Revista Portuguesa de Química

SOCIEDADE
PORTUGUESA
DE QUÍMICA

Fernando Pina
Dep. de Química
Faculdade de Ciências
e Tecnologia
Universidade Nova de Lisboa
2825 Monte da Caparica

COMISSÃO EDITORIAL
EDITORIAL BOARD

Ana Lobo
Dep. de Química
Faculdade de Ciências
e Tecnologia
Universidade Nova de Lisboa
2825 Monte da Caparica

Carlos Crispim Romão
Inst. de Tecnologia
Química e Biológica
Rua da Quinta Grande, 6
Apartado 127, 2780 Oeiras

Carlos F. G. C. Geraldes
Dep. de Bioquímica
Faculdade de Ciências
e Tecnologia
Universidade de Coimbra
3000 Coimbra

Fernanda Madalena A. Costa
Dep. de Química
Faculdade de Ciências
Universidade de Lisboa
Rua Ernesto de Vasconcelos,
Bloco 1
1700 Lisboa

Hugh Burrows
Dep. de Química
Faculdade de Ciências e
Tecnologia
Universidade de Coimbra
3000 Coimbra

Irene Montenegro
Centro de Química Pura e
Aplicada
Universidade do Minho
Largo do Paço
4700 Braga

José Costa Lima
Dep. de Química-Física
Faculdade de Farmácia
Universidade do Porto
Rua Aníbal Cabral, 164
4000 Porto

José Luís Figueiredo
Dep. de Engenharia Química
Faculdade de Engenharia
do Porto
Rua dos Bragas
4099 Porto Codex

José Ferreira Gomes
Dep. de Química
Faculdade de Ciências
Universidade do Porto
4000 Porto

José M. Gaspar Martinho
Dep. de Engenharia Química
Instituto Superior Técnico
1096 Lisboa Codex

Lélio Lobo
Dep. de Engenharia Química
Faculdade de Ciências e
Tecnologia
Universidade de Coimbra
3000 Coimbra

Revista Portuguesa de Química

Instruções para os Autores
Instructions for Authors

Tendo em vista um aumento significativo do alcance e impacto da *Rev. Port. Quím.*, os artigos são obrigatoriamente escritos e publicados em inglês, não excedendo as 20-30 páginas dactilografadas (formato A4 a dois espaços, margens de 2,5 cm), incluindo todas as tabelas, esquemas e figuras. As referências e notas *mencionadas no texto do manuscrito* serão ordenadas e numeradas entre parêntesis rectos. No final do manuscrito, antes das tabelas e figuras, essas referências e notas aparecerão numeradas sem parêntesis.

Exemplos:

1. P.R. Kemper, J. Bushnell, von G. Helden, M.T. Bowers, *J. Phys. Chem.* **97** (1993) 52.

2. J.P. Colloman, L.S. Hegedus, J.R. Norton, R.G. Finke, *Principles and Applications of Organotransition Metal Chemistry;* University Science Books: Mill Valey, 1987; pp. 279-354.

3. P.B. Armentrout, in *Gas Phase Inorganic Chemistry*; D.H. Russel, Ed.; Plenum Press: New Tork, 1989; pp 1-42.

As figuras e tabelas aparecerão numeradas em árabe e agrupadas no fim do manuscrito, após as referências e em folhas separadas. As tabelas só deverão ser utilizadas quando representarem uma vantagem para a exposição do texto ou quando não possam ser substituídas por gráficos ou figuras. As figuras devem ser enviadas com grande qualidade gráfica.

No caso de existir mais do que um Autor, deverá ser assinalado com um asterisco (*) o nome daquele a quem toda a correspondência ou comentários deverão ser enviados. Os manuscritos devem ser enviados em **triplicado** ao *Editor da Revista Portuguesa de Química, Sociedade Portuguesa de Química, Av. da República, 37, 4º, 1050 Lisboa, Portugal.*

Do Projecto de Estatuto Editorial da *Revista Portuguesa de Química*

Pretende a Revista Portuguesa de Química (Rev. Port. Quím.) publicar os resultados originais da investigação em Química na forma de revisões críticas concisas e que reflictam a actividade científica levada a cabo por investigadores ou pelas suas equipas.

Os artigos serão predominantemente solicitados através de um **convite** da responsabilidade do *Editor da Rev. Port. Quím.*, e poderão incidir sobre qualquer das áreas e disciplinas da Química, perspectivando a contribuição dos autores no quadro mais geral do seu desenvolvimento internacional e interdisciplinar e referenciando as opiniões e os autores mais relevantes, constantes na literatura.

Pretende-se que pelo seu conteúdo e formato se possa estabelecer um compromisso entre o interesse de uma audiência geral, mas atenta, e uma audiência especialmente ligada ao campo de investigação do(s) Autor(es). A concisão dos artigos submetidos, bem como o esforço de uma boa definição dos conceitos, referência e enquadramento crítico da investigação levada a cabo em torno dos temas propostos da Comissão Editorial ou de avaliadores por ela seleccionados. A inclusão de resultados não publicados deverá ser feita de uma forma moderada e quando significativamente necessária. Pelo contrário, as conclusões finais devem reforçar e perspectivar o significado dos resultados obtidos mais importantes. A submissão de artigos à *Rev. Port. Quím.* implica que o mesmo trabalho não seja ou tenha sido submetido outro Jornal ou Revista.

A Comissão Editorial é nomeada, por um período de três anos, pela Direcção da Sociedade Portuguesa de Química e tem a responsabilidade por todas as decisões editoriais. **A Sociedade Portuguesa de Química** e a **Comissão Editorial** da **Rev. Port. Quím.** não assume, no entanto, qualquer responsabilidade pelas afirmações e opiniões expressas pelos autores dos artigos publicados. Os comentários ou outros textos da responsabilidade dos membros da Comissão Editorial não envolvem a Sociedade ou a própria *Rev. Port. Quím.*

Some aspects of the photochemistry of fullerenes

Alguns aspectos da fotoquímica dos fulerenos

MÁRIO N. BERBERAN E SANTOS

CENTRO DE QUÍMICA-FÍSICA MOLECULAR, INSTITUTO SUPERIOR TÉCNICO, 1096 LISBOA CODEX, PORTUGAL

After a short overview of the fullerenes, the more physical aspects of their photochemistry are reviewed, with special emphasis on the polarization of the fluorescence of C_{60} and C_{70}, and on the delayed fluorescence of C_{70}.

Após uma breve panorâmica da origem e presente estado dos conhecimentos sobre os fulerenos, são apresentados alguns aspectos da sua fotoquímica, com particular relevo para a polarização de fluorescência do C_{60} e do C_{70}, e para a fluorescência retardada deste último.

1. Introduction

The discovery of the fullerenes in 1985 by Kroto *et al.* [1] immediately arose great interest. However, it was only after their bulk synthesis in 1990 by Krätschmer *et al.* [2, 3] and almost simultaneously by Taylor *et al.* [4], that the proposed molecular structures were conclusively shown to be correct. It was also only then that the study of the physical and chemical properties of fullerenes became possible. In this work, and after a short overview, the physical aspects of the photochemistry of the fullerenes will be reviewed, with special emphasis on the work carried out at Centro de Química-Física Molecular, IST.

Figure 1 – The structures of C_{60}, C_{70} and C_{76}. For comparison, typical carbon-carbon bond length values are: 1.33 Å in ethene (double bond), 1.40 Å in benzene (aromatic), and 1.54 Å in alkanes (single bond); In naphthalene (see Fig. 2) carbon-carbon bond lengths take values between 1.37 Å and 1.42 Å. Of the two possible IPR isomers of C_{76}, only the one shown has been isolated. It is optically active, with two enantiomeric forms.

Fullerenes are clusters composed by an even number of trivalent (three σ bonds and one π bond) carbon atoms. They have polyhedral shape, with pentagonal and hexagonal faces. The three smallest stable fullerenes are C_{60}, C_{70} and C_{76} (Fig.1). A large number of higher fullerenes was also isolated and characterised, namely C_{78}, C_{82}, C_{84} [5 and references therein] and, more recently, from C_{86} to C_{104}, and even C_{120} [6,7]. Still higher ones, up to C_{460}, have been observed in mass spectra. Much larger fullerene-like structures, either multi- or single-walled, e.g. nanotubes, have also been produced and are the subject of active research, see e.g. [8,9]. Since 1990, many fullerene derivatives, mainly of C_{60} and, to a minor extent, of C_{70}, have been synthesised [10]. They belong to several classes [10b]: (i) exohedral derivatives, like adducts and salts of fullerides, (ii) endohedral complexes, like $He@C_{60}$ and $Sc_4@C_{82}$ (iii) heterofullerenes, like $C_{69}N$ (iv) open cluster compounds, and (v) degradation products. It is interesting to note that the total synthesis of fullerenes remains a challenge for chemists [11].

Among the various clusters originally observed in the mass spectra of laser ablated graphite (C_n, with n = 24, 28, 32, 38, 40, 42, 44, 50, 60,...) only the heavier ones correspond to the stable species present in soot (either prepared by the Krätschmer-Huffman method [2, 3] or simply from hydrocarbon combustion [12]) that have been isolated and characterised (C_n, with n = 60, 70, 76, 78,....). The structure and stability of such clusters can be partially explained on the basis of two simple rules [5, 13a]: (i) in order to reduce angular strain, only pentagonal and hexagonal rings are allowed, and (ii) in order not to reduce the π-energy stabilisation, and simul-

taneously to reduce angular strain, pentagons must be surrounded by hexagons (the so-called isolated pentagon rule, or IPR). Fulfilment of the first rule, together with the celebrated Euler theorem, imply that clusters must have an even number n of atoms and exactly 12 pentagons and $(n\text{-}20)/2$ hexagons [5,13a]. C_{20}, composed exclusively by pentagons, is therefore the first possible fullerene cluster. However, the smallest n for which the IPR is obeyed is 60, the next value being 70 [13]. This justifies why C_{60} and C_{70} are especially abundant in the vapour and are the smallest fullerenes to have been isolated. Above 70, all even n are allowed by the same rules, and above 74, several IPR isomers exist. However, the number of observed isomers is in general much smaller than the maximum possible. For instance, C_{72} and C_{74} are not observed, and of the 35 IPR isomers of C_{88}, only 2 are known. It is suggested that this is due to finer aspects of relative stability and to the formation mechanism of the fullerenes [6]. For very large structures, the possibility of occurrence of heptagons and additional pentagons (usually associated, the so-called azulene or 5/7 defects) also exists [8].

In C_{60} (symmetry point group I_h), all carbon atoms are equivalent, but there are two different bond lengths (Fig. 1). In C_{70} (symmetry point group D_{5h}), there are five classes of carbon atoms, and eight different bond lengths (Fig. 1). In C_{76} (symmetry point group D_2), there are 19 classes of carbon atoms, and 30 different bonds (Fig. 1).

In fullerenes, π-electrons are fairly delocalized, and a simple quantum [14] (or even classical [15]) picture of full delocalization over a sphere is able to explain the gross features of the electronic absorption and dispersion spectra of C_{60}. Nevertheless, as show by the observed diversity of bond lengths, some single-double bond alternancy is retained (Fig. 1), and this has important consequences in the reactivity and regiochemistry of these molecules [10].

2. General aspects of the photochemistry of fullerenes

Our discussion of fullerenes will be mostly devoted to C_{60} and C_{70}. While some of the general conclusions probably apply to other members of the family, photophysical and photochemical informations on the higher fullerenes are scarce. In fact, little more is known than their electronic absorption spectra [4, 6, 7, 16]. This situation will undoubtedly change in the near future.

Absorption and emission

The photophysical properties of these all-carbon molecules result from: (i) Delocalization of π-electrons, (ii) large number of π-electrons and, (iii) high molecular symmetry. The delocalization of the π-electrons over a relatively large surface produces electronic absorption spectra covering most of the visible region, with onsets

in the red (C_{60}, C_{70}) or in the near infrared (C_{76}, C_{78}, ...). The fluorescence, with negligible Stokes shift, appears therefore in the red and infrared (C_{60}, C_{70}), while for the higher fullerenes (C_{76}, C_{78}, ...) it is expected to be located in the infrared. Also as a consequence of extended delocalization and large molecular size, the singlet-triplet splitting is small [17,18], and phosphorescence also appears in the extreme red and infrared for C_{60} and C_{70}. The large number of π-electrons (60, 70,...) implies a large density of electronically excited states (Fig. 2), leading to a continuous absorption in the UV and visible, and also to facilitated nonradiative transitions.
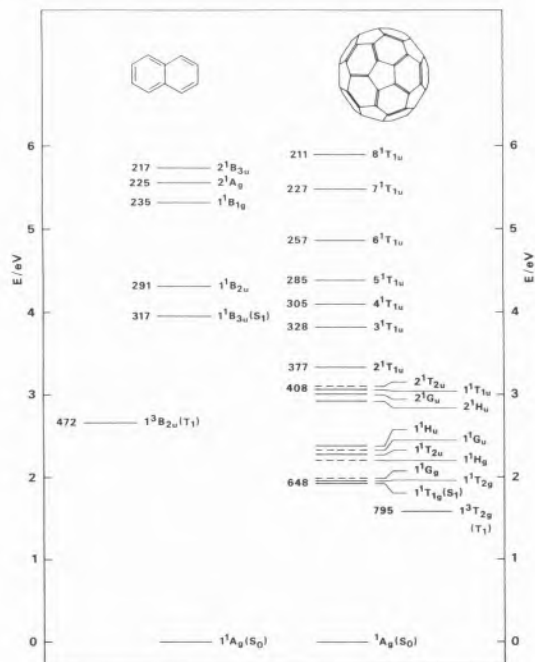
Figure 2. Comparison of the electronic state diagrams of naphthalene (10 π-electrons) and C_{60} (60 π-electrons). The approximate wavelengths (in nm) of the pure electronic transitions are shown on the left. For both molecules, only the first triplet (T_1) is shown. For C_{60}, only the T_{1u} states are shown for energies above 3.3 eV. Note the much higher density of states of C_{60}, as well as the much smaller singlet-triplet gap of this compound. The ionization energies of naphthalene and C_{60} are, respectively, 8.1 eV and 7.6 eV.

Finally, the high molecular symmetry restricts the number of allowed electronic transitions, rendering for example forbidden the S_1-S_0 radiative transition. In this way, the absorption spectra of both C_{60} and C_{70} show weak bands in the visible ($\lambda_{max} \simeq 540$ nm, $\varepsilon_{max} \simeq 710$ M^{-1} cm^{-1}, for C_{60}, and $\lambda_{max} \simeq 470$ nm, $\varepsilon_{max} \simeq 14500$ $M^{-1}cm^{-1}$ for C_{70}) but more intense ones in the violet and UV ($\varepsilon_{max} \simeq 10^5$ $M^{-1}cm^{-1}$) [2, 19-21]. Their solutions display a wide variety of beautiful colours, ranging from the "exquisitely delicate magenta" [22] of C_{60}, to the orange-red of C_{70}, and to the bright yellow-green of C_{76} [16]. A thorough study of the colours of C_{60} solutions is given in

[23]. The high molecular symmetry is also responsible for a Jahn-Teller distortion in the emissive (S_1 and T_1) states, for intrinsically low values of the polarization of the luminescence (C_{60}, C_{70}), and for a relatively large spin-orbit coupling [24].

Excited state dynamics

For a discussion of the excited state dynamics of the fullerenes, we refer to the so-called Jablonski diagram, Figure 3. Some important photophysical parameters are given in Table 1. Owing to the small singlet-triplet gap, and to the forbidden nature of the radiative $S_1 \rightarrow S_0$ process (fluorescence), the dominant S_1 decay process for C_{60} and C_{70} (and, in all likeliness, for at least the most symmetric higher fullerenes) is the $S_1 \rightarrow T_1$ intersystem crossing [17, 18]. Indeed, the quantum yield of triplet formation is almost unity in both cases. The fluorescence lifetime is quite short for both molecules, and is almost equal to the inverse of the $S_1 \rightarrow T_1$ intersystem crossing rate constant. This process is much faster than in typical aromatic hydrocarbons. Because it is not activated, the lifetimes and quantum yields are insensitive to temperature. Consistent with the forbidden nature of the radiative process, the fluorescence radiative lifetimes are of the order of 1 microsecond, that is, 3-4 orders of magnitude higher than the actual lifetimes. The quantum yields of fluorescence are therefore small. However, as will be discussed below, in certain favourable conditions, the effective fluorescence quantum yield of C_{70} may increase 10 to 100-fold as a consequence of the $S_1 \leftarrow T_1$ back-intersystem crossing [25]. The phosphorescence of C_{60} has been only studied at or below 77 K [26-28]. Given the variation with temperature observed in C_{70} [25], we regard as provisional the respective values given in Table 1.
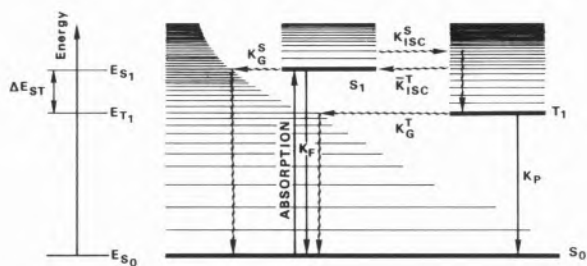
Figure 3. Simplified diagram of the electronic states and kinetic elementary steps after photon absorption (Jablonski diagram). As usual, the radiative processes ($S_1 \leftarrow S_0$ absorption, $S_1 \rightarrow S_0$ fluorescence and $T_1 \rightarrow S_0$ phosphorescence) are represented by straight lines, while the nonradiative processes ($S_1 \rightarrow S_0$ internal conversion, $S_1 \rightarrow T_1$ intersystem crossing, $S_1 \leftarrow T_1$ intersystem crossing, and $T_1 \leftarrow S_0$ intersystem crossing) are represented by wavy lines. It is possible that one or more higher triplets (T_2, etc.) also lie below S_1, thus participating, as intermediates, in the intersystem crossing process.

Table 1. Some photophysical parameters of C_{60} and C_{70}

	C_{60}	C_{70}
$\lambda(S_1\text{-}S_0)$ / nm	648	650
$\lambda(T_1\text{-}S_0)$ / nm	795	750
ΔE_{ST} / kJ mol^{-1}	34	25
τ_F / ns	1.1	0.65
τ_R / μs	2-6	1
Φ_F	2×10^{-4}	5×10^{-4}
Φ_T	$\simeq 1$	0.994
τ_p / ms	0.4	50
Φ_P	n.a.	10^{-3}
S_Δ	$\simeq 1.0$	$\simeq 0.9$

Singlet oxygen

One of the interesting aspects of both C_{60} and C_{70} is their ability to produce singlet oxygen O_2 ($^1\Delta_g$) with almost unit efficiency, $S_\Delta \simeq 1$ [17, 18, 29]. On the one hand, their quantum yield of triplet formation is close to unity, and the quenching of the fullerene triplet by oxygen through triplet-triplet annihilation, is close to

$$^3C_n^* + {}^3O_2 \rightarrow {}^1C_n + {}^1O_2^* \quad (n = 60, 70) \tag{1}$$
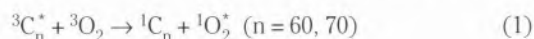
diffusion control. On the other hand, the reverse process (i.e., quenching of singlet oxygen by ground state fullerenes) proceeds at a rate much smaller than diffusion control [17, 30]. This fact, together with the low fluorescence quantum yield, makes the fullerenes very good photosensitizers [31].

Optical limiting behaviour

Within a certain wavelength range, fullerenes present the interesting property of an effective absorption coefficient that increases with the incident light intensity [32, 33]. In this way, solutions or films of these compounds respond nonlinearly to the incident light, being more opaque to the higher intensities. This appears to occur in those spectral regions where the triplet-triplet intrinsic absorption coefficients are considerably higher than the corresponding singlet-singlet ones, mainly on account of an increasing population of the triplet state with intensity (reverse saturable absorption, or RSA). Both the incident pulse duration and repetition rate play an important role, because the T_1 population evolution depends on the interplay of external excitation and internal photophysical kinetics. Simplified kinetic models for RSA exist [34, 35]. The physical picture is complicated by the possibility of alternative or at least co-existing mechanisms, namely thermal lensing and

nonlinear light scattering [33, 36]. Considerable effort towards applications is well underway [37].

3. Fluorescence polarization of C_{60} and C_{70}

The linear polarization of the fluorescence emitted at a right angle with the excitation direction is conveniently measured by the quantity anisotropy, r [38], where

$$r = \frac{I_{||} - I_{\perp}}{I_{||} + 2I_{\perp}} \quad (2)$$

$I_{||}$ is the intensity of the fluorescence with vertical polarization and I is the intensity of the fluorescence with horizontal polarization, the excitation being made with vertically polarized light (Fig. 4). For a ground state isotropic distribution of molecules, the fluorescence
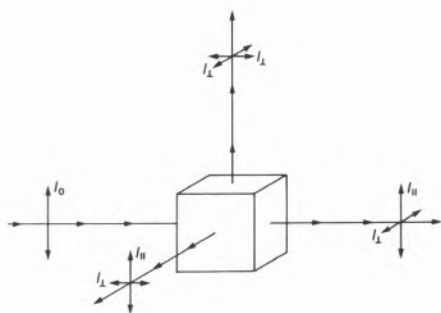
Figure 4. Isotropic sample excited with vertically polarized light. The fluorescence emitted in the plane perpendicular to the polarisation direction of the excitation may be decomposed in vertically polarized (parallel, $I_{||}$) and horizontally polarized (perpendicular, $I_{\perp}$) components.

anisotropy is a direct measure of the angular correlation between the (one-photon) absorption and the emission transition dipoles [39]

$$r(t) = 0.4 \frac{3 < \cos^2 \alpha > (t) - 1}{2} \quad (3)$$

where α is the angle between absorption and emission transition dipoles and $< \cdots >$ denotes the ensemble average which is in general a function of time.

If rotation and energy migration do not occur within the excited state lifetime, the anisotropy in response to excitation by a $\delta(t)$ pulse is constant in time and identical to that obtained for steady-state excitation.

In such a case, both reduce to the fundamental anisotropy r_o [39], where $<...>$ is now an average over the

$$r_o = 0.4 \frac{3 < \cos^2 \alpha > - 1}{2} \quad (4)$$

angular distribution within the molecular framework. Upper and lower bounds for the fundamental anisotropy are 0.4 (collinear absorption and emission) and -0.2 (orthogonal absorption and emission).

If three mutually perpendicular axes are defined with respect to the molecular framework (molecular frame), these three axes are frequently non-equivalent from the symmetry point of view. In that case, the angle α is unique for a given pair of excitation and emission wavelengths; In particular it is zero for excitation at the 0-0 band of S_1, provided the emitting S_1 retains the Franck-Condon geometry. Hence, the fundamental anisotropy takes its maximum value, 0.4, when exciting at the S_1 0-0 band.

However, if two of the axes of the molecular frame are equivalent, x and y say, and if the absorption and the (several equivalent) emission transition moments occur in the xy plane, then the fundamental anisotropy will have as a maximum value only 0.1 [40, 41]. This was conclusively shown to be the case for benzene (ground state symmetry point group D_{6h}) and triphenylene (ground state point group D_{3h}) [40-42].

For the even more symmetrical molecules belonging to the tetrahedral, octahedral and icosahedral point groups, where the x, y and z axes are equivalent, the possibility of intrinsically unpolarized fluorescence arises.
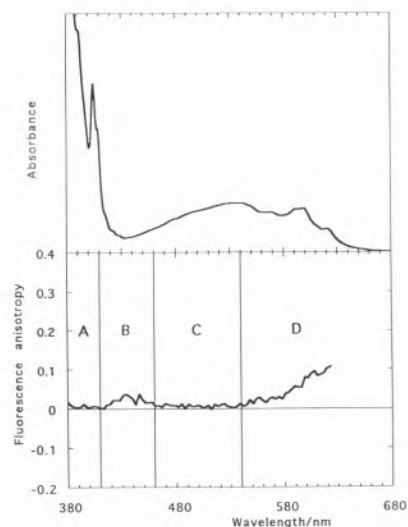
Figure 5. Electronic absorption spectrum (top) and excitation polarization (bottom) of 2×10^{-4} M C_{60} in toluene-ethanol (10:1) glass at 140 K. Owing to weakness of the fluorescence, the measured anisotropy departs from zero in regions B and D, where stray light (B, D) and polarized Raman scattering from toluene (D) have comparable intensity [50].

An interesting candidate would be the C_{60} molecule, that belongs to the icosahedral (I_h) point group, as convincingly shown by its ^{13}C-NMR [4, 43], IR absorption [3, 44], and vibrational Raman [44] spectra. The discovery of C_{60} weak fluorescence [45-48], prompted us to investigate its fundamental polarization, predicted some years before to be nil [49]. It was indeed found that the fluorescence of C_{60} had negligible polarization when measured in low temperature, optically transparent rigid organic glasses (Figures 5, 6 and 7) [50, 51]. It was thus concluded that the fluorescence is intrinsically unpolarized, as expected on theoretical grounds. C_{60} is probably the first molecule to display intrinsically unpolarized fluorescence.
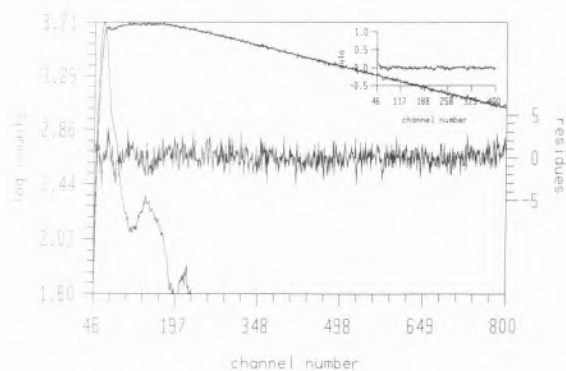
Figure 6. Fluorescence decay of C_{60} in a methylcyclohexane-toluene (7:2) glass at 110 K, obtained with the picosecond laser system of CQFM [51]. $[C_{60}] = 8 \times 10^{-5}$ M. Excitation and emission wavelengths were 595 nm and 690 nm. The time scale was 2.77 ps/channel. The Raman scattering can be seen as a first peak in the decay (the possibility that it was due to excitation scattered light is ruled out by its emission wavelength dependence and because a cut-off filter was used). The decay is well fitted (reduced chi-squared = 1.21, random residuals and negligible autocorrelation) by a sum of three exponentials, one of which, of zero lifetime, accounts for the Raman scattering, the other two having $\tau_1 = 1.09$ ns ($\alpha_1 = 1.25$) and $\tau_2 = 0.10$ ns ($\alpha_2 = -0.25$). The 100 ps component is only observed at low temperature.

From the point of view of symmetry, C_{70} is again an interesting molecule. The molecule is known to belong to the D_{5h} point group, thus having two equivalent axes (x and y). The electronic transition moment for S_1-S_0 may in principle occur either along the z-axis or in the xy-plane. In the first case, the fundamental anisotropy of C_{70} may take values between 0.4 and -0.2, depending on the excitation wavelength. In the second case, the fundamental anisotropy of C_{70} may take values only between 0.1 and -0.2, depending on the excitation wavelength. As mentioned above, cases where 0.1 is the maximum allowed value are known for planar molecules belonging to the D_{nh} point groups ($n \geq 3$). In these, however, anisotropy values cannot be different from 0.1, because all singlet-singlet one-photon transitions are in-
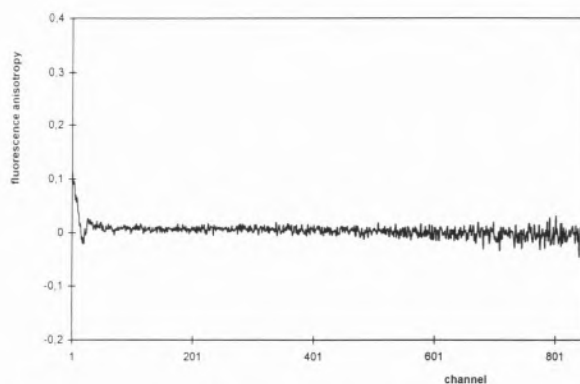
Figure 7. Experimental fluorescence anisotropy decay of C_{60} in a methylcyclohexane-toluene (7:2) glass at 110 K, obtained with the picosecond laser system of CQFM [51]. $[C_{60}] = 8 \times 10^{-5}$ M. Excitation and emission wavelengths were 595 nm and 690 nm. The time scale was 2.77 ps/channel. It is seen that, after the impulse duration (FWHM = 35 ps, or 13 channels), the anisotropy has a nearly constant value very close to zero (0.001 ± 0.005). Note that the Raman scattering, being much faster than fluorescence, does not affect the results, that fall into region D of the steady-state experiment (Fig. 5).

plane, whereas in C_{70} out-of-plane ones (i.e. along the z-axis) are also possible. The only available theoretical calculation on the polarization of the electronic transitions of C_{70} [52], predicts the electronic transition moment for $S_1 \leftarrow S_0$ to be in the xy-plane. Our experimental results [51] support such a conclusion (Fig. 8): The anisotropy is never above 0.1, even when close to the
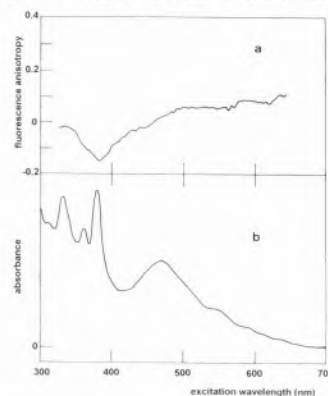
Figure 8. (a) Steady-state anisotropy of C_{70} in a methylcyclohexane-toluene (7:2) glass at 110 K, and, (b) Absorption spectrum of C_{70} a methylcyclohexane-toluene (7:2) glass at room temperature, both as a function of the excitation wavelength. $[C_{70}] = 7 \times 10^{-5}$ M. The small oscillations observed in (a) are due to noise.

absorption on-set. The first electronic transition of C_{70} is thus polarized in the xy plane, in agreement with the calculations by the tight-binding model [52]. It can also be seen in Fig. 8 that the anisotropy attains a minimum at ca. 380 nm. This minimum, close to -0.2, coincides with the peak wavelength (378 nm) of a strong absorption band that is therefore z-polarized.

4. Delayed fluorescence of C_{70}

Molecular fluorescence is almost always the result of a two-step process: a transition from the ground state to an electronically excited state (absorption) followed by a transition from the same excited state (or another one of lower energy, after fast relaxation) to the ground state (*prompt fluorescence*, PF), see Figure 3. For the common case of closed-shell molecules, the states involved in the last step are S_0 (ground singlet state) and usually S_1 (first excited singlet). However, fluorescence can also occur by a more complicated route, *via* the triplet manifold: after excitation, and once attained S_1, there is an intersystem crossing to the triplet manifold (triplet state T_1), and then, after vibrational thermalization, a second intersystem crossing back to S_1, followed by emission proper (Figure 3). This second type of fluorescence, called *thermally activated delayed fluorescence* (TDF), is significant only if the two following conditions are met: (i) reasonably high probability of $S_1 \rightarrow T_1$ intersystem crossing, i.e., high quantum yield of triplet formation Φ_T where

$$\Phi_T = \frac{k_{ISC}^s}{k_F + k_G^S + k_{ISC}^s} \qquad (5)$$

and, (ii) reasonably high probability of subsequent $S_1 \leftarrow T_1$ back intersystem crossing, i.e., high quantum yield of singlet formation, Φ_S, which by analogy with Eq. 5 is defined

$$\Phi_S = \frac{k_{ISC}^T}{k_p + k_G^T + k_{ISC}^T} \qquad (6)$$

In fact, it follows from the kinetic model depicted in Figure 3 that the steady-state intensities ratio of delayed fluorescence (DF) to prompt fluorescence (PF) is given by

$$\frac{I_{DF}}{I_{PF}} = \frac{\Phi_{DF}}{\Phi_{PF}} = \frac{1}{\dfrac{1}{\Phi_S \Phi_T} - 1} \qquad (7)$$

From the theory of nonradiative transitions, it is known that high values of k_{ISC}^S are favoured by a small ΔE_{ST} (S_1 - T_1 gap). The same holds *a fortiori* for k_{ISC}^T, because it is *approximately* given by [53, 54]

$$k_{ISC}^T = \overline{k}_{ISC}^T \exp\left(-\frac{\Delta E_{ST}}{RT}\right) \qquad (8)$$

where $\overline{k}_{ISC}^T$ is the average rate constant for the adiabatic $S_1 \rightarrow T_1$ intersystem crossing, and the exponential factor is the fraction of triplets whose total internal energy (electronic + vibrational) is equal or larger than the electronic energy of S_1. Therefore, TDF is only possible for molecules with small ΔE_{ST} and even then at not too low temperatures.

Although known for many years [53 and references therein], the phenomenon of TDF remains extremely rare. In most of the cases studied, including the classic one, eosin [53], it is exceedingly weak, in the sense that $\Phi_{DF} \ll \Phi_{PF}$.

The known photophysical properties of C_{70}, namely the quantum yield of triplet formation close to one [18, 29, 55, 56], the small S_1 - T_1 gap [18, 27, 57, 58] and the long intrinsic phosphorescence lifetime [57-60], all favour TDF for this molecule.

In fact, we have observed exceptionally *strong* TDF ($\Phi_{DF} \gg \Phi_{PF}$) for C_{70} dissolved in degassed liquid and solid paraffin [25]. The same study disclosed an intriguing variation of the phosphorescence spectrum with temperature, and enabled the revision of the published values of ΔE_{ST} and of Φ_T, the last one obtained with unprecedented precision from a new kinetic analysis.

The luminescence spectrum of C_{70} in paraffin is shown in Figure 9. It consists of a high energy system, fluorescence (630 nm - 750 nm), and a low energy system, phosphorescence (>750 nm). A Parker plot (i.e., $\ln(I_{DF} / I_P)$ vs. 1/T, where I_P is the phosphorescence intensity) of 10^{-5} M degassed solutions of C_{70}, from -59°C to 5°C, gives a straight line, from whose slope one obtains $\Delta E_{ST} = 26 \pm 1$ kJ/mol. On the other hand, for degassed solutions and temperatures above -20°C, DF is much stronger than PF (Figure 10; at the highest recorded temperature, 70°C, it is 50 times stronger). Using the new method of analysis described in [25], for temperatures from -20°C to 70°C, one obtains a singlet-triplet gap of
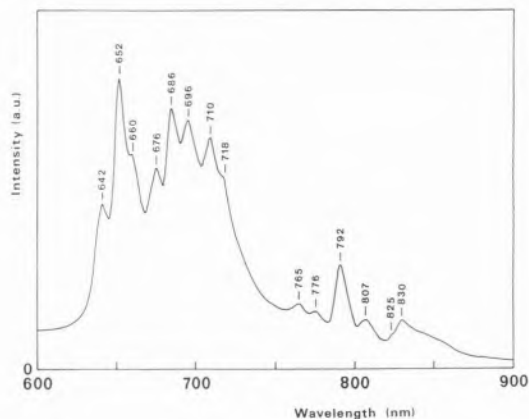
Figure 9. Luminescence spectrum of C_{70} dissolved in paraffin, at -30 °C. $[C_{70}] = 2.5 \times 10^{-5}$ M. Excitation and emission slits were 18 nm and 2 nm, respectively. The fluorescence spans the range 630 nm - 750 nm. The fluorescence band at 642 nm appears to be a hot band. The phosphorescence begins at ca. 750 nm, and extends further to the infrared (not shown).
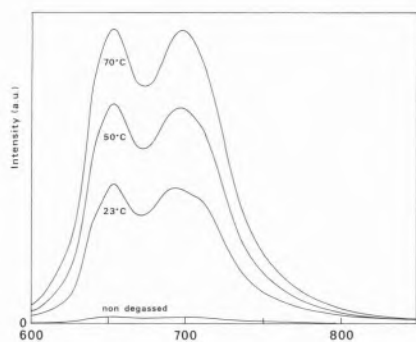
Figure 10. Low resolution fluorescence spectra of a 1.4×10^{6} M solution of C_{70} in liquid paraffin. Degassed solution at 23 °C, 50 °C, and 70 °C. The intensity of the non degassed solution is independent of temperature, and is entirely due to prompt fluorescence. The rise with temperature observed in the degassed solutions results from the increasing contribution of delayed fluorescence to the total intensity. Emission slits were 9 nm.

25 ±1 kJ/mol, in good agreement with the value recovered from the Parker plot. From the accepted spectroscopic assignment of 652 nm as the 0-0 band of the fluorescence [58, 61], the determined range of values of ΔE_{ST} (24 kJ/mol - 27 kJ/mol) places the 0-0 band of the phosphorescence in the range 750 nm - 765 nm. The phosphorescence spectrum recorded at -85 °C, where delayed fluorescence is negligible, has indeed its on-set at ca. 750 nm (Fig. 11). Careful examination of the
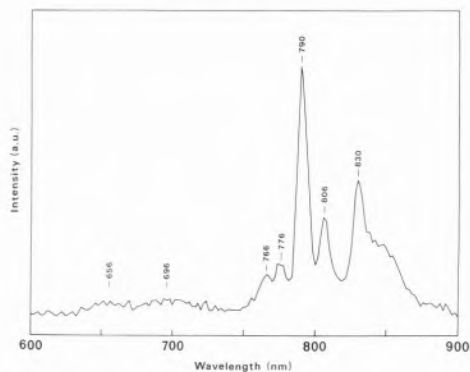
Figure 11. Phosphorescence spectrum of C_{70} in solid paraffin at -85°C. The residual delayed fluorescence is seen as two very weak bands on the left. Time delay: 10 ms.

room temperature luminescence spectrum of a degassed solution (dominated by delayed fluorescence, Fig. 12) shows again a weak shoulder at 776 nm and weak bands at 791 nm and 830 nm, making very likely that the phosphorescence spectrum does not change significantly for temperatures higher than at least -85 °C. Previous studies of the phosphorescence spectrum [26, 27, 46, 57, 58] have not explored the temperature region above 77 K and, as a consequence, the high energy bands were not observed. This occurs because on cooling down to ca. 77 K or less, and thus well below the temperature region where significant TDF is obser-
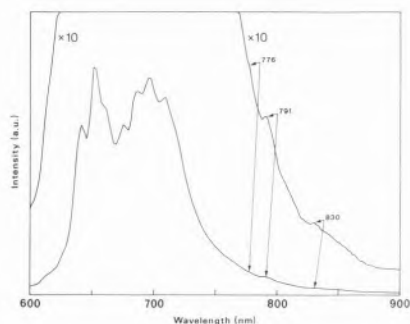
Figure 12. Luminescence of a 10^{-5} M degassed solution of C_{70} in liquid paraffin, at room temperature. The phosphorescence barely emerges from the fluorescence tail.

ved, the high energy system of bands looses intensity, and the first noticeable band of the phosphorescence spectrum appears at 788 nm (77 K), or even at 806 nm (methylcyclohexane at 10 K) [58]. This peculiar behaviour could be due to solid matrix effects [10].

The data analysis performed according to the new method also yields $k_{ISC}^{T} \simeq 10^{7}$ s^{-1}. This value is to be compared with that of the direct intersystem crossing, $k_{ISC}^{S} = 2 \times 10^{9}$ s^{-1}, which is simply computed as the inverse of the fluorescence lifetime (ca. 650 ps). The difference between the two rate constants does not appear unreasonable, in view of the much higher density of final states expected for the direct intersystem crossing case.

A quantum yield of triplet formation $\Phi_{T} = 0.994 \pm 0.001$, is also obtained. This value is to be compared with the published ones, obtained by more sophisticated techniques [18, 29, 55, 56], 0.76 ± 0.15, 0.97 ± 0.03, 1 ± 0.15, and 0.90 ± 0.15, and is believed to be substantially more accurate, especially as a lower bound. Using the determined value of Φ_{T} and Eq. 7, one obtains for the high temperature limit ($\Phi_{S} = 1$), that $\left(\dfrac{I_{DF}}{I_{PF}} \right)_{max}$

= 166. In this way, the global fluorescence quantum yield ($\Phi_{F} = \Phi_{PF} + \Phi_{DF}$) of C_{70} can in principle be 167 times higher than that of prompt fluorescence, and thus attain the very respectable value of $167 \times 5 \times 10^{-4} = 0.08$.

5. Concluding remarks

The chemistry and photochemistry of fullerenes and derivatives is an area in great expansion, and with almost unlimited possibilities, given the diversity of structures covered. As regards applications, it also offers great promise.

(CNAM, Paris, and ENS Cachan), Ing. Jean-Pierre Lefèvre (CNAM, Paris, and ENS Cachan), Dr. Aleksandre Fedorov (CQFM, IST) and Eng. João M.M. Garcia (CQFM, IST).

References

1. H.W. Kroto, J.R. Heath, S.C. O'Brien, R.F. Curl, R.E. Smalley, *Nature* **318** (1985) 162.

2. W. Krätschmer, K. Fostiropoulos, D.R. Huffman, *Chem. Phys. Letters* **170** (1990) 167.

3. W. Krätschmer, L.D. Lamb, K. Fostiropoulos, D.R. Huffman, *Nature* **347** (1990) 354.

4. R. Taylor, J.P. Hare, A.K. Abdul-Sada, H.W. Kroto, *J. Chem. Soc. Chem. Commun.* (1990) 1423.

5. J. Cioslowski, *Electronic Structure Calculations on Fullerenes and Their Derivatives*, Oxford University Press, New York and Oxford, 1995.

6. Y. Achiba, Proceedings of Fullerenes '96, to be published in *J. Phys. Chem. of Solids*.

7. H. Richter, K. Taghizadeh, W.J. Grieco, A.L. Lafleur, J.B. Howard, Proceedings of Fullerenes '96, to be published in *J. Phys. Chem. of Solids*.

8. T.W. Ebbesen, *Phys. Today*, June 1996, 26.

9. A. Thess, R. Lee, P. Nikolaev, H. Dai, P. Petit, J. Robert, C. Xu, Y.H. Lee, S.G. Kim, A.G. Rinzler, D.T. Colbert, G.E. Scuseria, D. Tománek, J.E. Fischer, R.E. Smalley, *Science* **273** (1996) 483.

10. (a) R. Taylor, D.R.M. Walton, *Nature* **363** (1993) 685. (b) A. Hirsch, Proceedings of Fullerenes '96, to be published in *J. Phys. Chem. of Solids*.

11. P.W. Rabideau, A. Sygula, *Acc. Chem. Res.* **29** (1996) 235.

12. J.B. Howard, J.T. McKinnon, Y. Makarovsky, A.L. Lafleur, M.E. Johnson, *Nature* **352** (1991) 139.

13. (a) H. W. Kroto, *Nature* **329** (1987) 529. (b) T.G. Schmalz, W.A. Seitz, D.J. Klein, G.E. Hite, *J. Am. Chem. Soc.* **110** (1988) 1113.

14. (a) M. R. Savina, L.L. Lohr, A.H. Francis, *Chem. Phys Letters* **205** (1993) 200. (b) M. N. Berberan-Santos, *Quím. Nova* **17** (1994) 293.

15. D. Östling, A. Rosén, P. Apell, G. Mukhopadhyay, *Proc. SPIE* **2284** (1994) 48.

16. (a) F. Diederich, R.L. Whetten, *Acc. Chem. Res.* **25** (1992) 119. (b) K. Kikuchi, N. Nakahara, T. Wakabayashi, M. Honda, H. Matsumiya, T. Moriwaki, S. Suzuki, H. Shiromaru, K. Saito, K. Yamauchi, I. Ikemoto, Y. Achiba, *Chem. Phys. Letters* **188** (1992) 177.

17. J. W. Arbogast, A. O. Darmanyan, C. S. Foote, Y. Rubin, F. N. Diederich, M. M. Alvarez, S. J. Anz and R. L. Whetten, *J. Phys. Chem.* **95** (1991) 11.

18. J. W. Arbogast and C. S. Foote, *J. Am. Chem. Soc.* **113** (1991) 8886.

19. H. Ajie, M.M. Alvarez, S.J. Anz, R.D. Beck, F. Diederich, K. Fostiropoulos, D.R. Huffman, W. Krätschmer, Y. Rubin, K.E. Schriver, D. Sensharma, R.L. Whetten, *J. Phys. Chem.* **94** (1990) 8630.

20. J.P. Hare, H.W. Kroto, R. Taylor, *Chem. Phys. Letters* **177** (1991) 394.

21. R.M. Williams, J.W. Verhoeven, *Chem. Phys. Letters* **194** (1992) 446.

22. H.W. Kroto in *The Fullerenes*, H.W. Kroto, J.E. Fischer and D.E. Cox eds., Pergamon, Oxford, 1993.

23. J. Catalán, J.L.Saiz, J.L. Laynez, N. Jagerovic, J. Elguero, *Angew. Chem. Int. Ed. Engl.* **34** (1995) 105.

24. (a) P.M. Allemand, G. Srdanov, A. Koch, K. Khemani, F. Wudl, *J. Am. Chem. Soc.* **113** (1991) 2780. (b) F. J. Adrian, *Chem. Phys.* **211** (1996) 73.

25. M.N. Berberan-Santos, J.M.M. Garcia, *J. Am. Chem. Soc.* **118** (1996) 9391.

26. Y. Zeng, L. Biczok, H. Linschitz, *J. Phys. Chem.* **96** (1992) 5237.

27. K. Palewska, J. Sworakowski, H. Chojnacki, E. C. Meister, U. P. Wild, *J. Phys. Chem.* **97** (1993) 12167.

28. D.J. Heuvel, I.Y. Chan, E.J.J. Groenen, J. Schmidt, G. Meijer, *Chem. Phys. Letters* **231** (1994) 111.

29. R.R. Hung, J.J. Grabowski, *Chem. Phys. Letters* **192** (1992) 249.

30. A.A. Krasnovsky Jr, C.S. Foote, *J. Am. Chem. Soc.* **115** (1993) 6013.

31. M. Selke, C.S. Foote, *J. Am. Chem. Soc.* **115** (1993) 1166.

32. L.W. Tutt, A. Kost, *Nature* **356** (1992) 225.

33. A. Kost, J.E. Jensen, M.B. Klein, J.C. Withers, R.O. Loufty, M.B. Haeri, M.E. Ehritz, *Proc. SPIE* **2284** (1994) 208.

34. F. Henari, J. Callaghan, H. Stiel, W. Blau, D.J. Cardin, *Chem. Phys. Letters* **199** (1992) 144.

35. J.R. Heflin, S. Wang, D. Marciu, C. Figura, R. Yordanov, *Proc. SPIE* **2530** (1995) 176.

36. S.R. Misra, H.S. Rawat, M.P. Joshi, S.C. Mehendale, K.C. Rustagi, *Proc. SPIE* **2284** (1994) 220.

37. R. Signorini, M. Zerbetto, M. Meneghetti, R. Bozio, M. Maggini, C. Favei, M. Prato, G. Scorrano, *J. Chem. Soc. Chem. Commun.* (1996) 1891.

38. A. Jablonski, *Bull. Acad. Polon. Sci., Ser. Math. Astr. Phys.* **8** (1960) 259.

39. (a) F. Perrin, *Ann. Phys. (Paris)*, **12** (1929) 169. (b) A. Jablonski, *Z. Naturforsch.* **16a** (1961) 1.

40. P.P Feofilov, *The Physical Basis of Polarized Emission*, Consultants Bureau, N.Y., 1961.

41. F. Dörr, *Angew. Chem. Int. Ed. Engl.* **5** (1966) 478.

42. R.D. Hall, B. Valeur and G. Weber, *Chem. Phys. Letters* **116** (1985) 202.

43. R.D. Johnson, G. Meijer, D.S. Bethune, *J. Am. Chem. Soc.* **112** (1990) 8983.

44. D.S. Bethune, G. Meijer, W.C. Tang, H.J. Rosen, W.G. Golden, H. Seki, C.A. Brown and M.S. de Vries, *Chem. Phys. Letters* **179** (1991) 181.

45. C. Reber, L. Yee, J. McKiernan, J.I. Zink, R.S. Williams, W.M. Tong, D.A.A. Ohlberg, R.L. Whetten and F. Diederich, *J. Phys. Chem.* **95** (1991) 2127.

46. S.P. Sibley, S.M. Argentine and A.H. Francis, *Chem. Phys. Letters* **188** (1992) 187.

47. Y. Wang, *J. Phys. Chem.* **96** (1992) 764.

48. D. Kim, M. Lee, Y.D. Suh and S.K. Kim, *J. Am. Chem. Soc.* **114** (1992) 4429.

49. M.N. Berberan e Santos, *Polarização da luminescência molecular*, IST, 1987.

50. M.N. Berberan-Santos, B. Valeur, *J. Chem. Soc. Faraday Trans.* **90** (1994) 2623.

51. A. Fedorov, M.N. Berberan-Santos, J.P. Lefèvre, B. Valeur, submitted to *Chem. Phys. Letters*.

52. J. Shumway and S. Satpathy, *Chem. Phys. Letters* **211** (1993) 545.

53. C.A. Parker, *Photoluminescence of Solutions*, Elsevier, Amsterdam, 1968.

54. F. Tanaka, M. Okamoto, S. Hirayama, *J. Phys. Chem.* **99** (1995) 525.

55. D.K. Palit, A.V. Sapre, J.P. Mittal, C.N.R. Rao, *Chem. Phys. Letters* **195** (1992) 1.

56. R.V. Bensasson, T. Hill, C. Lambert, E.J. Sand, S. Leach, T.G. Truscott, *Chem. Phys. Letters* **206** (1993) 197.

57. S.M. Argentine, A.H. Francis, C.-C. Chen, C.M. Lieber, J.S. Siegel, *J. Phys. Chem.* **98** (1994) 7350.

58. S. M. Argentine, K. T. Kotz, A. H. Francis, *J. Am. Chem. Soc.* **117** (1995) 11762.

59. M. R. Wasielewski, M. P. O'Neil, K. R. Lykke, M. J. Pellin, D. M. Gruen, *J. Am. Chem. Soc.* **113** (1991) 2774.

60. H.T. Etheridge, R.B. Weisman, *J. Phys. Chem.* **99** (1995) 2782.

61. Y.-P. Sun, C.E. Bunker, *J. Phys. Chem.* **97** (1993) 6770.

Molecular Basis for the Structure and Function of the Xanthine Family of Molybdenum Enzymes

Estrutura e Função das Enzimas de Molibdénio Pertencentes à Família da Oxidase da Xantina

MARIA JOÃO ROMÃO

INSTITUTO DE TECNOLOGIA QUÍMICA E BIOLÓGICA, APT. 127, 2780 OEIRAS and INSTITUTO SUPERIOR TÉCNICO, DEP. QUÍMICA, 1096 LISBOA CODEX, PORTUGAL

This work is based on the X-ray crystallographic analysis of the aldehyde oxido-reductase from *Desulfovibrio(D.) gigas*, a member of the xanthine oxidase family. Its crystal structure is described and comparisons are made with spectroscopic and kinetic studies from the literature. A main emphasis is put on the recent achievements which have contributed towards the understanding of the structure and function of the xanthine oxidase family of molybde, num enzymes - the hydroxylases. Specific mechanistic implications of the crystal structure of the *D. gigas* enzyme are discussed in relation to the xanthine oxidase family of enzymes.

Este trabalho baseia-se na análise cristalográfica da oxido-reductase do aldeído de *Desulfovibrio(D.) gigas*, uma enzima pertencente à família das oxidases da xantina. Após uma descrição da respectiva estrutura cristalina, são feitas comparações com estudos espectroscópicos e cinéticos da literatura, colocando-se uma ênfase particular nas contribuições mais recentes para a compreensão da estrutura e função das hidroxilases de molibdénio. As implicações mecanísticas específicas da estrutura cristalina são discutidas no contexto das enzimas do tipo da oxidase da xantina.

Abbreviations

D. - Desulfovibrio
FAD - flavin adenin dinucleotide
Mop - aldehyde oxido-reductase from *Desulfovibrio gigas*
MPT - mononucleotide form of molybdopterin
MCD - molybdopterin cytosine dinucleotide
MGD - molybdopterin guanine dinucleotide
MAD - molybdopterin adenine dinucleotide
MHD - molybdopterin hypoxanthine dinucleotide
XO - xanthine oxidase

Structural Biology and Chemistry are fields which have greatly benefited and expanded in the years which followed the discovery of X-ray diffraction in 1912 [1]. The application of X-ray Crystallography to the structural analysis of Biological Macromolecules started in the late fifties [2, 3] and ever since is the technique which has more deeply influenced the knowledge of the three-dimensional structure of proteins, nucleic acids, viruses and other macromolecules: the catalytic centers of enzymes have been unraveled and structure-function relationships established, with important consequences in many domains such as the structure-based *drug design*.

The present article is focused on the crystal structure of a molybdenum enzyme which belongs to the xanthine oxidase family and is the first representative of this group of enzymes for which a 3D structure was determined [7, 8]. Recently, the 3D structures of members of other classes of molybdenum hydroxylases were determined: DMSO reductases [16, 17] and formate dehydrogenase from *E. coli* [69], which however show no homology to the the XO group of enzymes. A description of the basic principles and methodologies used in Protein Crystallography is beyond the scope of this article, but has been outlined elsewhere [4].

1. Introduction

Molybdenum containing enzymes can be classified in two classes: 1-nitrogenase, which catalyzes the reduction of dinitrogen to ammonia, and where molybdenum is part of an heterometal FeMo-cofactor [9]; and 2- hydroxylases or oxotransferases, which promote a variety of two-electron oxidation-reduction reactions, whereby oxygen (oxo) atom transfer occurs[1]. Molybdenum plays an essential role in the catalysis of the oxo-transfer reaction, coupled to an electron-transfer between substrate and other cofactors, such as Fe/S centers, hemes or flavins. Coupling of both functions leads to a formal direct transfer of an oxygen atom from the metal center to the substrate. Among the molybdenum hydroxylases which are currently known, xanthine oxidases, sulfite oxidases, nitrate reductases, aldehyde oxidases and DMSO reductases have been characterized in great detail (see [5] for a review). Molybdenum oxotransferase enzymes catalyze the following general reactions, where water has been shown to be the source of the incorporated oxygen atom [10], and reducing equivalents are generated [11, 12].

$$RH + H_2O \rightarrow ROH + 2e^- + 2H^+ \quad \text{(1.1) RH = aldehyde or aromatic heterocycle}$$

$$RR'E + H_2O \overset{a}{\underset{b}{\rightleftarrows}} RR'E = O + e^- + 2H^+ \quad \text{(1.2) E = N, S}$$
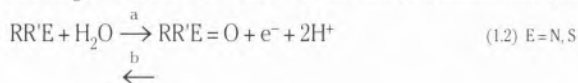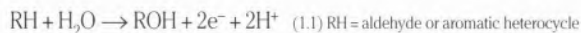
Xanthine oxidase from bovine milk, due to its ready availability, is the prototype for molybdenum hydroxylases and has been intensively studied for the past forty years, but many other oxomolybdenum enzymes have also been investigated within the last decade. In a recent review on molybdenum oxotransferases [5], these enzymes have been classified into three families on the basis of the reactions they catalyze, as well as on the basis of the characteristics of their molybdenum centers: (1) The xanthine oxidase family, (2) the sulfite oxidase and assimilatory nitrate reductases family and (3) the DMSO reductase family. This classification is supported by amino acid homologies within these protein families, which are found in a wide range of organisms. The large xanthine oxidase family of enzymes may be considered as the one of the true hydroxylases, with the dithiolene moiety of the molybdopterin cofactor (*fac*) (Figure 1) coordinated to an MoOS (H₂O) unit. The MoOS coordination was suggested by EXAFS experiments [12-14], but the presence of an additional water ligand was established by crystallography [7, 8]. Members of this family have been found broadly distributed within eukaryotes, prokaryotes and archaea. They catalyze the oxidative hydroxylation of aldehydes and aromatic heterocycles in reactions involving a C-H bond cleavage (reaction 1.1). Sulfite oxidase and assimilatory nitrate reductases possess a *fac*MoO2 unit, with uncertainty about additional coordination positions of the molybdenum. They have been found in eukaryotes and catalyze a simple oxo transfer to the lone pair of sulfur in sulfite oxidase (E=S, reaction 1.2-a) or the reverse reaction in nitrate reductase (E=N, reaction 1.2-b). In the DMSO reductase family, other enzymes such as the biotin-S-oxide reductase and bacterial dissimilatory nitrate reductases have been included, which also follow the overall stoichiometry of reaction 1.2-b. This family of enzymes possesses the Mo-cofactor with a bisdithiolene coordination of the molybdenum, as recently established by X-ray crystallography [16, 17]. These studies showed that the Mo atom is also coordinated by the side chain oxygen of a serine (Ser 147). This class of enzymes seems to be structurally more diverse when compared to the other two, and its members have only been found in bacteria and archaea.

The molybdenum containing hydroxylases, in particular xanthine oxidases, have been extensively
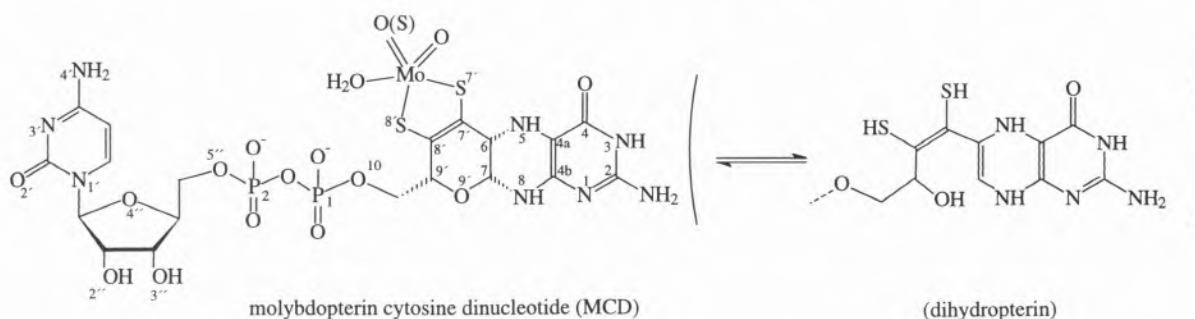
Figure 1 - The molybdenum coordination, with metal ligand distances obtained by EXAFS for Mop [18] and for xanthine oxidase XO [13, 15], in oxidized and reduced forms.

---

1 There is complementary as well similarity in the chemistries of molybdenum and tungsten, and pterin-containing tungsten enzymes have also been isolated and characterized, primarily from hyperthermophilic Archaea [27]

studied by a wealth of experimental techniques [5, 6] but a detailed knowledge of these enzymes has suffered from the lack of crystal structures for members of this class. The aldehyde oxido-reductase from *Desulfovibrio (D.) gigas* -Mop- is the first representative of this important group of metalloproteins for which a high-resolution crystal structure is available [7, 8]. In this work we will concentrate on the xanthine oxidase family of molybdenum enzymes with emphasis on the crystal structure of Mop. The functional and mechanistic implications of the Mop structure on a general catalytic mechanism for the xanthine oxidase family of enzymes are an important consequence of this study.

2. Brief survey of the xanthine oxidase family of molybdenum enzymes

Molybdenum oxotransferases, in general, possess a common Mo=O group in the metal coordination sphere, reason why they have been called oxomolybdenum enzymes [6]. The molybdenum hydroxylases, which constitute the xanthine oxidase family (containing an MoOS unit) have been assigned on the basis of their irreversible inhibition by cyanide which reacts with Mo=S, releasing thiocyanate. Until X-ray structural data were available for this class of enzymes, the main techniques used to study the molybdenum coordination sphere have been EXAFS [13, 14] (and [18] for Mop) and EPR from the Mo^V species [19] (and [20, 21] for Mop). EXAFS data have shown that the metal center in its oxidized form has at least one oxo group with a distance Mo=O of about 1.7 Å, as well as two thiolate ligands at distances of about 2.4 Å (see Figure 2). This latter feature is common to all oxomolybdenum enzymes, and is due to the coordination of molybdenum to an organic cofactor commonly designated by "molybdopterin" (Figure 1, left). In spite of the lability of this cofactor when isolated from the protein matrix, its basic pterin ring structure and dithiolene side chain were proposed on the basis of chemical and spectroscopic analysis of the cofactor isolated from the enzymes in different modified or inactivated forms [22-26]. However, the presence of a pyran ring in the structure was established only by crystallography for the tungsten-containing aldehyde oxido-reductase from *Pyrococcus furiosus* [27], for the aldehyde oxido-reductase from *Desulfovibrio gigas* (Mop) [7] and more recently, for the DMSO Reductases from two *Rhodobacter* species [16, 17].

The molybdopterin cofactor is coordinated to the metal via its dithiolene function and may be present either in dinucleotide forms or in the simpler monophosphate form. In Mop, the cofactor is the dinucleotide of cytosine -molybdopterin cytosine dinucleotide (MCD) -, but in other enzymes from prokaryotic sources is found as guanine (MGD) [28], adenine (MAD) [29] or hypoxanthine (MHD) [29] dinucleotide. The simpler monophosphate form (MPT), also found in some bacterial enzymes, is the only form present in all known enzymes from eukaryotic sources and the diversity of the pterin cofactor within known molybdenum-containing enzymes seems to be related to the species of origin rather than the enzymatic function, as shown within the xanthine oxidase family, where MPT has been found in eukaryotic enzymes and MCD in bacterial enzymes reported so far [5].

Members of the xanthine oxidase family show about ~25% sequence identity and 60-70% sequence similarity, with higher conservation in segments involved in the binding of the metal centers and redox-active sites [30]. Enzymes included in this class are either homodimers, α_2, or dimers of heterotrimers, $\alpha_2\beta_2\gamma_2$. Mop, aldehyde oxidases and eukaryotic xanthine oxidases and xanthine dehydrogenases are organized as α_2 homodimers, with all redox-active cofactors confined within a single polypeptide chain. The common folding pattern for this group of enzymes, starts with the two [2Fe-2S] domains, followed by a flavin domain (which is absent in Mop and replaced by an extended segment which connects two domains- Figure 6) and finishes with two large domains responsible for binding the molybdopterin cofactor [30]. Other groups of hydroxylases have been included in the xanthine oxidase family of enzymes, due to analogies in their molybdenum centers and the reactions they catalyze: the CO dehydrogenases, the isoquinoline oxidoreductases and nicotine dehydrogenases, all from bacterial and archaeal sources (see [5] for references). They are organized as $\alpha_2\beta_2\gamma_2$ structures, where the α subunit binds the two [2Fe-2S] centers, the β subunit the flavin and the γ subunit the molybdenum cofactor.
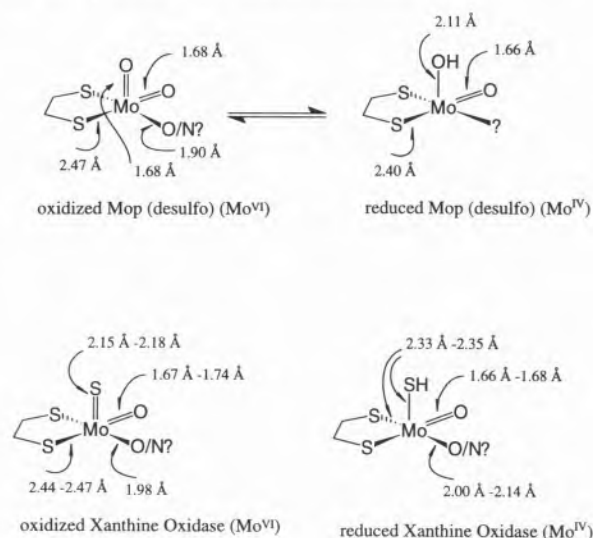
Figure 2 - The molybdopterin cytosine dinucleotide (MCD) cofactor as established by crystallography in Mop [7]. The open chain form is shown as an equilibrium between the two forms (as suggested in solution).

Xanthine oxidase, the prototype of the molybdenum hydroxylases, has been intensively studied by spectroscopic and kinetic techniques, which have contributed to characterize it from a structural and functional point of view. Several inorganic model systems have also been proposed and are described in a number of recent reviews [31-34]. Some attention will now be given to the general features of xanthine oxidase, highlighting relevant points which can be illustrated with details from the crystal structure of Mop.

Xanthine oxidase catalyses the oxidation of xanthine to uric acid, using dioxygen as the physiological electron acceptor (or NAD^+ in the case of xanthine dehydrogenases). In addition to xanthine, it can also oxidize other aromatic heterocycles and aldehydes, but with little specificity. Xanthine is oxidized at the molybdenum center, whereby MoVI is reduced to MoIV and reducing equivalents are transferred to O_2 at the flavin site. Electron transfer between the molybdenum center and the FAD is mediated by the Fe/S centers. Intramolecular electron transfer within the xanthine oxidase family of molybdenum enzymes is an essential aspect of catalysis and has been studied by different techniques such as flash photolysis, pulse radiolysis and pH-jump perturbation (see 5 for references).

EPR was one of the first tools employed for the study of the molybdenum center of xanthine oxidase, and a variety of Mo^V species were detected, either in the course of equilibrium reductive titrations, or transiently within reaction with substrate. Other characteristic EPR signals have been observed from complexes of the enzyme with inhibitors such as arsenite [35], methanol [36], ethylene glycol [37] and alloxanthine [38], and analogies are encountered between the EPR spectra of XO and those of Mop [20, 21, 39]. For example, the Mo^V EPR signals ("type 2"), exhibited by xanthine oxidase upon reaction with xanthine [40] ($g_{1,2,3}$= 1.9951, 1.9712, 1.9616) are quantitatively very similar to the corresponding signals reported for Mop upon reaction with salicylaldehyde [20] ($g_{1,2,3}$= 1.9882(3), 1.9702(3), 1.9643(3)), which suggests similarities of their active sites.

The two [2Fe,2S] centers - Fe/S I and Fe/S II -, are also clearly distinguished on the basis of their characteristic EPR signals, which display similar features in Mop [21] and xanthine oxidases: the so-called Fe/S type I shows characteristic g-values similar within eukaryotic xanthine oxidases (milk XO [36] $g_{1,2,3}$= 2.022, 1.935; 1.899) and Mop [21] ($g_{1,2,3}$= 2.021, 1.938; 1.919) typical of spinach ferredoxin ($g_{1,2,3}$= 2.02(1), 1.93(1), 1.90(1)). On the other hand, center Fe/S II, , exhibits broader lines than center Fe/S I, with g-values comparable in Mop [21] (2.057, 1.970, 1.900) and milk xanthine oxidase [68] (2.12, 2.01, 1.91), but displaying larger variations within members of the xanthine oxidase family than the center Fe/S I.

Mössbauer spectroscopy also allows the distinction between both Fe/S centers in the reduced enzymes: one of the centers (probably Fe/S I) exhibits a rather normal

quadrupole splitting ΔE_Q of 2.4 mm/s and 2.69(2) mm/s for the ferrous site in xanthine oxidase (at 175K) [41] and Mop (at 180K) [42] respectively, while the other center exhibits an unusually large quadrupole splitting of 3.2 mm/s and 3.14(2) mm/s for xanthine oxidase and Mop respectively.

3. The crystal structure of the aldehyde oxido-reductase from *Desulfovibrio gigas*

The crystal structure of Mop, the first representative of a molybdenum oxotransferase, is a valid model for the interpretation of a large number of experimental data of xanthine oxidase and related enzymes. It was solved at high resolution in its native desulfo form [7], as well as in sulfo, oxidized, reduced and alcohol-bound forms [8], allowing a detailed look at the several structural aspects of the molybdenum hydroxylases relevant for catalysis: a) domain architecture; b) structure of the cofactors and binding mode within the polypeptide chain; c) molybdenum center environment; d) metal coordination and its role in catalysis.

In analogy to eukaryotic xanthine oxidases, xanthine dehydrogenases and aldehyde oxidases, Mop is an α_2 homodimer of two 100 kDa subunits (2x907 amino acids) [67]. The redox-active cofactors are two different kinds of [2Fe-2S] centers [21], and a molybdopterin cofactor (molybdopterin cytosine dinucleotide-MCD) (Figure 1), inserted in discrete domains (Figure 3) within a single subunit.
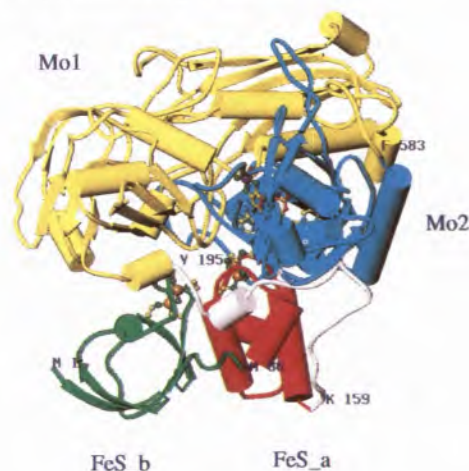
Figure 3 - The molecular structure of Mop with the four independent domains represented in different colors and cofactors shown as colored spheres. *Fe/S_b*- green, residues 1-76; *Fe/S_a*- red, residues 84-156; *connecting peptide*-white, residues 158-195; *Mo1*- yellow, residues 196-581; *Mo2*- blue, residues 582-907.

Structural and domain arrangement of the protein

From the electron density map interpretation the two [2Fe-2S] centers were recognized at the earlier

Figure 4 - Stabilization of the molybdopterin cytosine dinucleotide of Mop by hydrogen bonding interactions with surrounding residues (with indication of the domains to which they belong).

stages of the analysis, while the molybdopterin cofactor was identified, only at a later stage of the structure solution, as a molybdopterin cytosine dinucleotide, confirmed by chemical analysis [43]. For some of the higher resolution data sets [8], isopropanol molecules as well as magnesium ions, both from the crystallization solution, were clearly identified. The presence of alcohol molecules, particularly the one close to the molybdenum site (Figure 8), was important for mechanistic deductions, to model the Michaelis complex of an aldehyde substrate molecule (Figure 9).

The protein molecule is roughly globular with an approximate diameter of 75 Å (Figure 3) and its secondary structure shows 28% of α-helical and 21% of β-sheet conformations. The protein is organized into four domain: two small 2Fe-2S domains (Fe/S_a and Fe/S_b) and two much larger domains (Mo1 and Mo2), which constitute the molybdopterin binding portion of the enzyme. The MCD cofactor is bound by a network of hydrogen bonding interactions whereby domain Mo1 contributes with two single molybdopterin binding segments and domain Mo2 binds the other side of the pterin system and provides all of the dinucleotide binding segments (Figure 4). These two large domains also surround the molybdenum catalytic site and define, at their interface, a 15 Å deep tunnel, wide open at the surface and constricted in the middle, which leads substrate molecules into the buried molybdenum catalytic site (Figure 5).

The first Fe/S_b (residues 1 to 76) domain possesses the consensus sequence CXXGXCXXC shared by the plant type ferredoxin class of iron-sulfur proteins [30]. Also the chain fold is similar to that of plant (*Spirulina*

platensis) [2Fe-2S] ferredoxins [44]. It shows the topology of a five-stranded β-half barrel with an α-helix running almost perpendicular to the strands direction. The overall fold can be superimposed to *Spirulina platensis* ferredoxin 44] with a deviation of less than 0.5Å in the Cα atom positions of the iron-sulfur cluster binding turns. The second iron-sulfur domain Fe/S_a (residues 84 to 156) reveals a unique and new fold for

Figure 5 - Simplified Cα representation of the Mop molecule with cofactors highlighted as colored spheres. Two isopropanol molecules are also represented as well as the three buried waters close to the molybdenum site (purple sphere). The arrow points towards the entrance of the tunnel, marked also by one of the isopropanol molecules (IPP1) and a few waters.

ferredoxins: a four-helix bundle with two longer central helices flanked by two shorter α-helices. The metal cluster lies at the N-termini of the two central helices. Domain Fe/S_a is connected to the molybdenum binding domain Mo1 via a long extended meander with irregular secondary structure and which spans about 50 Å across a rather concave region of the surface of the molecule. This concave region extends from one side of the protein to the other and appears to be the most likely site for the insertion of the flavin domain present in xanthine oxidases. This region of the molecule also appears to be the most probable site of interaction with flavodoxin, which has been shown to be able to accept electrons from Mop/aldehydes *in vitro* [45].

The two larger Moco binding domains, Mo1 (residues 196 to 581) and Mo2 (residues 582 to 907) are in close contact to each other and the molybdenum catalytic site is right at their interface. Domain Mo1 is rather elongated (ca 75 Å long and 28 Å wide) and organized in two subdomains: a larger N-terminal part which consists of a seven-stranded incomplete β-barrel with one α-helix filling its central cavity with two additional helices flanking the barrel and exposed to solvent. The smaller C-terminal subdomain consists of a five-stranded mixed parallel-antiparallel β-sheet

flanked by two helices which run approximately parallel to the strands direction. Domain Mo2 is also organized in two subdomains, each with a similar basic fold (a four-stranded β–sheet, which bends around a pair of helices), and in part dyad related. Both subdomains resemble two large wings spanning over 80 Å and the co-factor MCD lies at the intersection of those two wings.

The [2Fe-2S] centers

Both [2Fe-2S] clusters are approximately planar with the two iron atoms and four cysteine sulfur atoms defining a plane orthogonal to the plane of the [2Fe-2S] group. All iron atoms are tetrahedrally coordinated by the sulfur atoms of the cysteines, with Fe-S bond lengths of 2.2 Å and 2.3 Å for the iron-sulfide and for the iron-cysteine S^γ respectively. The N-terminal plant-type ferredoxin iron cluster (Fe/S_b) has one of the iron atoms linked to C40 and C45, while the other iron atom is coordinated by C48 and C60. The second iron cluster (Fe/S_a) has one of the iron atoms bound to C100 and C139 and the other bound to C103 and C137. While center Fe/S_b is close to the protein surface with Cys $S^\gamma60$ exposed to the solvent, center FeS_a is 14 Å buried and in contact with the molybdopterin.

Xanthine Oxidases
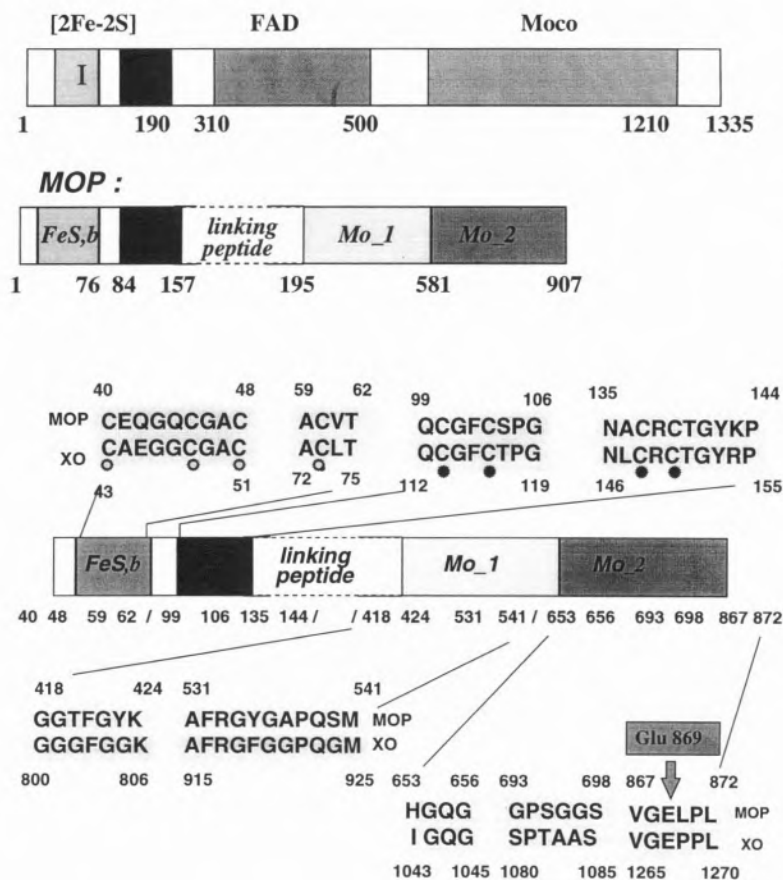
Figure 6 - Primary sequence alignment of Mop and xanthine oxidase. Top-Domain arrangement of xanthine oxidases. in comparison to Mop. Bottom Selection from the amino acid sequence alignment of Mop with xanthine oxidase from *Drosophila Melanogaster* [30], highlighting the conservation of the primary sequence in both proteins, particularly high in the regions involved in co-factor binding.

The molybdopterin cofactor

The structure of the molybdopterin cofactor was established for Mop by crystallography as a cytosine dinucleotide, MCD (Figure 1). The general bicyclic pterin structure and dithiolene side chain had been proposed by chemical and spectroscopic analysis [22-26], but the fused pyran ring resulting in a tricyclic structure had not been detected and was only established by crystallography. It has now been found in three different enzymes: in the aldehyde ferredoxin oxido-reductase (AOR) from *Pyrococcus furiosus* [27], in Mop [7] and in the DMSO reductase (DMSOR) from *Rhodobacter sphaeroides* [16 and *capsulatus* 17]. In both AOR and DMSOR, the metal atom (W and Mo respectively) coordinates two molybdopterins through their dithiolene groups but in distinct ways. The AOR from *Pyrococcus furiosus* has two molybdopterins coordinating the tungsten atom and additionally linked by a magnesium ion bound to their phosphate groups. In DMSOR two molybdopterin guanine dinucleotides (MGD) are bound to the molybdenum atom resulting in a very elongated structure (~35 Å) [16, 17]. Neither the tungstoprotein nor the DMSO reductases share homology to Mop or to the xanthine oxidase family and belong to three different protein families, of which, the DMSO reductase family of oxomolybdenum enzymes is likely to be structurally more diverse than the xanthine oxidase family [5].

When isolated, the cofactor is bicyclic, suggesting that the pyran ring is closed by a reversible intramolecular nucleophilic addition of the hydroxyl 9´-OH to the C7 carbon atom of the double bond of a dihydropterin system (Figure 1). The pyran ring closure may occur *in situ* subsequent to binding of the open chain cofactor to the enzyme favored by the numerous interactions between the cofactor and the surrounding polypeptide chain (cf. Figure 4). In all structures the pyran is tilted approximately 40° relative to the two ring pterin system (<30° in one of the pterins of DMSOR). The fused pyran ring has three chiral centers C6, C7 and C9´, with absolute configurations *R, R, R* in Mop, as well as in the other structures. Contrary to suggestions [27, 46] based on functional and structural inorganic models for DMSOR [46], neither the pterin nucleus, nor the dinucleotide coordinate directly to the metal. In DMSOR the protein contributes to the metal coordination with the side chain oxygen of a serine residue, which may be a cysteine or selenocysteine in other members of the DMSOR diverse family.

In Mop the pterin cofactor is in the dinucleotide MCD form and it is well documented [5] that the variants molybdopterin (MPT) and molybdopterin dinucleotides (MGD, MCD, MAD, MHD) are widely distributed among eukaryotes and prokaryotes. In enzymes from eukaryotes the pterin has always been found in the MPT form. The role of the ribonucleotide portion of the molybdopterin dinucleotides in some bacterial enzymes remains obscure.

The MCD present in Mop is extended, with a widest distance of 17 Å between the cytidine (N4´ atom) and the pterin (O4 atom). The functional groups of the cytidine are hydrogen bonded to main chain atoms of domain Mo2 (Figure 4). The structure of this cofactor is likely to represent the general form of dinucleotidic cofactors of other molybdenum hydroxylases, but differences in stabilization of the base are expected, namely in those segments (of domain Mo2) which bind the dinucleotide part, absent in the eukaryotic hydroxylases. This is reflected by the lower degree of homology in this part of the primary sequence, when Mop is compared with eukaryotic xanthine dehydrogenases [30].

Structure and environment of the metal centers

The redox-active cofactors of Mop are inserted in the protein matrix in close proximity to each other, and define a plausible electron transfer pathway (Figure 7). While the first Fe/S center b is rather exposed to solvent via its cysteine 60, Fe/S center a is approximately 14 Å below the molecular surface and has no direct contact with the solvent. The closest distance between the iron atoms of the two Fe/S centers is ca. 12 Å while the molybdenum atom lies 15 Å away from the nearest iron atom of center a. The molybdenum site is also buried but accessible to the protein surface through a 15 Å deep tunnel as described above. The pterin system of Mo-co is in direct contact with the nearest iron-sulfur center through a hydrogen bond between the amino group at C2 and the γ sulfur atom of Cys139, which coordinates one of the iron atoms. The two iron-sulfur centers are in contact via a chain of seven covalent bonds and a single hydrogen bond between amide of residue Ala136 and the carbonyl of Cys45. The 2Fe-2S iron centers are bound by covalent bonds between the irons and cysteine residues and further stabilized by a number of NH- - -S hydrogen bonds between their sulfur
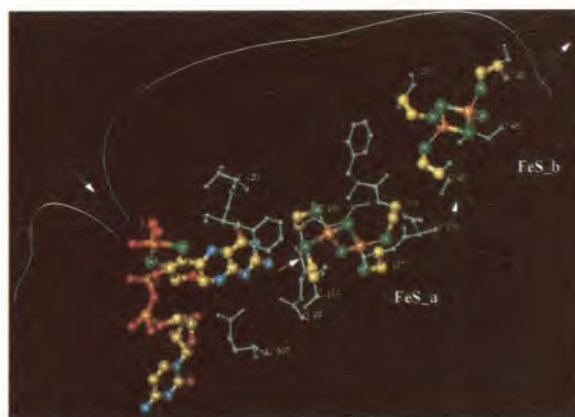
Figure 7 - Molecular representation of the three co-factors of Mop: molybdopterin cytosine dinucleotide and both close contacting centers, FeS_a and FeS_b, exposed to solvent through Cys 60. For the sake of clarity, residues contacting with the dinucleotide part are omitted. The arrow shows the direction of the tunnel which leads into the molybdenum site.

atoms and the amide groups of the surrounding protein main chain. The pterin tricycle is bound by two hydrogen bonds of the carbonyl oxygen atom O4 to amides of the segment Thr420-Phe421 from domain Mo1, while the phenyl ring of Phe421 is coplanar with the pterin, favoring a π–π interaction with the pterin ring. The side chain of Gln807 from domain Mo2, anchors the other edge of the pterin establishing hydrogen bonds to nitrogens N1 and N8 (Figures 4 and 7). The channel connecting the surface with the molybdenum site is coated with hydrophobic residues exclusively from domains Mo1 and Mo2. It exhibits a constriction at half-way by a cluster of hydrophobic residues Phe425, Phe494, Leu497 and Leu626. These side chains must move away in order to let bulkier aromatic substrate molecules pass and reach the catalytic site.

After passing the hydrophobic channel, reducing substrates, aldehydes in the case of Mop, react and are oxidized at the molybdenum center: Mo^{VI} is reduced to Mo^{IV} and reducing equivalents are transferred through the partially conjugated system of the pterin and the hydrogen bond, pterin-NH2—Sγ-C139, to the Fe/S center a (Figure 7). Electron transfer proceeds via seven covalent bonds and one hydrogen bond (NH Ala136- - - O=C C45) towards the exposed Fe/S center b. From here, electrons will flow to an unknown physiological electron acceptor in the case of Mop or, in the case of xanthine oxidase, will be intramolecularly transferred to the flavin center and from there to molecular oxygen, generating superoxide. Intramolecular electron transfer within the xanthine oxidase family of enzymes has been recognized as an essential aspect of catalysis and has been extensively studied by a number of techniques [37-43]. This proposed pathway assigns an important role to the pterin ring for the electron transfer from molybdenum to the Fe/S centers. Since the molybdenum atom is not coordinated to any protein side chain (Figure 8), the pterin cofactor is also essential in anchoring the molybdenum within the protein. A third important role may be attributed to the pterin co-factor by modulating the redox properties of the molybdenum. Crystallographic data of Mop [8] obtained under reducing conditions show conformational changes in the cofactor: In the reduced crystals the dithiolene sulfurs are wider apart (larger S-Mo-S angle) with a sulfur-sulfur distance of 3.5 Å instead of 3.0 Å as found in the oxidized crystals [7]. Additionally, in the reduced derivatives, the dithiolene molybdenum cycle is less planar with the molybdenum atom deviating ca 0.4-0.7 Å from the mean plane of the ring, towards the apical ligand. This distortion also suggests that the dithiolene double bond participates in the redox reaction. In the oxidized state of the enzyme, the short distance between the dithiolene sulfur atoms (3.0 Å) is closer than their van der Waals contacts (2x1.85 Å), implying a partial disulfide bond formation, which is lost upon reduction of the molybdenum. As a result, the dithiolene ligand donates electron density to the metal and consequently the reduction potential of the molybdenum center would be expected to decrease. Additionally, electron donating capacity of the ligand to the metal may favor a five-fold coordinated Mo^{VI} center.

Such a role for the pterin cofactor in modulating the redox state of the metal had been proposed [47] on the basis of model compound studies for a Mo^{VI} complex L_2MoO_2 ($L=SC(CH_3)_2CH_2NH(CH_3)$), which also exhibits an S – – S bond of 2.76 Å, indicative of a disulfide bond character. The authors suggest that the dithiolene group may participate in the $Mo^{VI} \rightarrow Mo^{IV}$ redox process by involving a disulfide-thiolate reduction, associated with formal changes of the oxidation state of the metal. Other recent model compound studies [48] have proven that tetrahydropterin is able to reduce MoVI with disulfur coordination (MoO_2(diethyldithiocarbamate)$_2$) to MoIV in (MoO (diethyldithiocarbamate)$_2$). These results suggested that oxidation/reduction states of the pterin were involved in the Mo oxidation state during substrate turnover, but extrapolations from these model systems to molybdenum-containing enzymes were not satisfactory. Although the synthesis of such complexes of molybdenum coordinated to pterin species has deserved much attention (reviewed in [32]) and has often been successful [46, 49, 50], the relationship to the reaction mechanism of molybdenum hydroxylases is not clear.
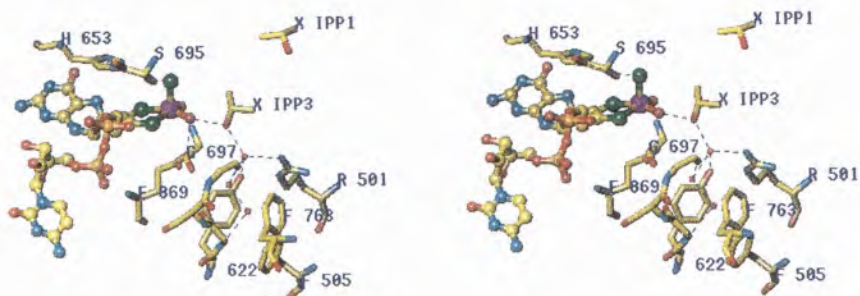
Figure 8 - Stereo representation of the molybdenum catalytic site (sulfo form) and surrounding residues within hydrogen bonding distance. IPP1 points in the direction of the channel and IPP3 is the isopropanol molecule which binds directly to the metal.

There have been proposals in the literature concerning the role of the pterin co-factor in the enzymatic mechanism of the molybdenum oxotransferases. Studies of the state of reduction of MPT in sulfite oxidase [51, 52] and in xanthine oxidase [51] have led to the suggestion of the direct involvement of the pterin in catalysis, either via electron transfer or by modulation of the oxidation/reduction properties of the metal. The Mop crystal structure analyzed in oxidized and reduced states 8 supports these suggestions.

The molybdenum site and its environment

The molybdenum coordination sphere was defined on the basis of the 2.25 Å crystallographic data [7] as square pyramidal geometry, with no protein ligand binding to the metal, but a glutamate residue (Glu 869, conserved within the XO family of enzymes [30] (Figure 6)) is only 3.5 Å away from the metal. With higher resolution data to 1.8 Å 8, the molybdenum site was defined in greater detail and the metal ligands unambiguously identified. In the approximate square pyramidal arrangement, the dithiolene ring system defines the equatorial plane and contributes with two sulfur ligands. The three remaining positions, assigned as three oxygen ligands, were identified as one water ligand (MoOH2) and two oxo (Mo=O) groups, where the former occupies the position *trans* to sulfur S7´ of the dithiolene (Figure 8). The two oxo groups were identified on the basis of shorter distances to the metal (range of 1.6-1.9 Å for the different crystals analyzed [8]), as well as lack of hydrogen bonds to surrounding residues. The water ligand shows a longer bond to the metal (range of 2.1-2.5 Å) and is within hydrogen bonding contact to the hydroxyl group of isopropanol IPP3, to amide of Gly 697 and to carboxylate of Glu 869 (Figure 8). The apical oxo ligand is found to be replaced by a sulfur atom in Mop crystals which have been resulfurated by incubation with sulfide under turnover conditions [8]. This important result allowed to identify the catalytically essential Mo=S group.

The structure of the molybdenum site agrees with EXAFS data for xanthine oxidases and for Mop, which show an oxo group present in both oxidized and reduced forms of xanthine oxidases and of Mop (Figure 2), while three sulfur ligands are assigned for XO with one longer Mo-S bond for the reduced state of the enzyme. However, EXAFS data did not show the second oxygen ligand, which has now been identified as a coordinated water.

Relevant residues and well ordered water molecules within the molybdenum catalytic site are represented in Figure 8 for the sulfo form of the enzyme. In close vicinity to the molybdenum is the conserved Glu 869 which is approximately trans to the apical position and may bind directly to the metal by a small rotation of the carboxylate. The apical Mo=S group has the imidazole of His 653 as nearest neighbor, within hydrogen bonding distance (~3.2 Å). The Mo=O ligand is in a quite constrained environment, close to amide of Arg 533 (3.3 Å), to carbonyl oxygen of Phe 421 (3.8 Å) and to Cα of Gly 422. The metal bound water is facing the mouth of the extended channel and is the most accessible ligand and the neighboring isopropanol molecule (IPP3), from the crystallization solution, contacts with this water ligand. Alcohols are known to inhibit Mop 45 (as well as xanthine oxidase [37]) and this IPP3 site is a good model for the Michaelis complex of the reaction of Mop with aldehydes. The isopropanol molecule is part of a network of hydrogen bonds namely to a chain of three buried water molecules (137W, 138W, 105W). Two of these waters (137W, 138W) are stabilized by hydrogen bonds to the surrounding polypeptide, but the innermost water, 105W, is located in a particularly apolar environment (Phe 505, Phe 763 and Tyr 622) (Figure 8). Apart from IPP3, other isopropanol molecules were located in the crystal structure of Mop, one of which (IPP1) was identified close to the mouth of the channel (Figure 5), which may justify the known inhibitory effect of alcohols in Mop as well as in xanthine oxidase.

To summarize, one can distinguish as most relevant features of this catalytic site: (1) Its accessibility through an extended hydrophobic channel, which has a constriction separating a wider outer compartment from a more restricted inner binding site at the molybdenum; (2) The presence of a water ligand which is the most accessible one, and probably the source of the transferred hydroxyl group and binding site of reaction intermediates; (3) The chain of well ordered buried water molecules, able to replenish the vacant coordination site after product dissociation; (4) The conserved residue Glu 869 close to the molybdenum, which may transiently bind to the metal and act as a proton acceptor of the water molecule (see below).

4. Homology of the aldehyde oxido-reductase from *Desulfovibrio gigas* with the xanthine oxidase family of enzymes

Comparison of the amino acid sequence of Mop with that of different xanthine oxidases was the first proof of their relationship 7, 30. The multiple alignment with xanthine oxidases from mammalian, insect and fungal sources, showed that the Mop amino acid sequence is highly conserved with ca. 52% homology and 25% identity, suggesting a close structural relationship [30] (Figure 6). Homology also extends to other molybdopterin and iron-sulfur containing enzymes.

The homology is particularly high in those segments associated with binding of the redox-cofactors (but not of the cytosine dinucleotide) as well as within residues of the substrate binding pocket, and for residues of the tunnel. As detailed in Figure 6-b, the binding segments of the cofactors are well conserved. Interruptions by deletions and insertions occur only in
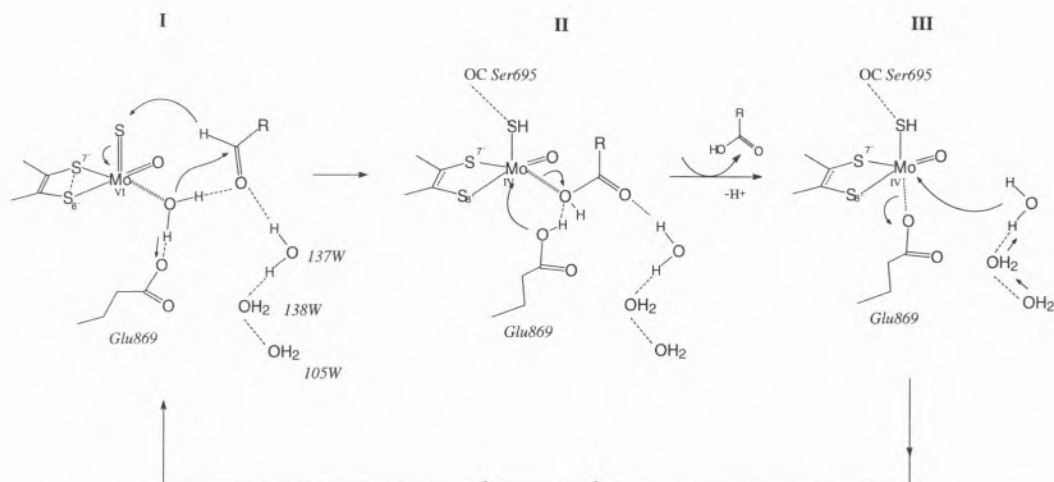
Figure 9 - Hypothetical structures for the reductive half-cycle of the hydroxylation reaction of Mop and xanthine oxidase: I, the Michaelis complex with aldehyde substrate close to MoVI; II, the enzyme/carboxylic acid product complex (MoIV); and III, after product dissociation, intermediate with Glu869

loop regions and at the N- and C- termini. The long deletion of about 400 residues in the Mop structure, between residues 157 and 195, corresponds to the FAD domain in the xanthine oxidases, absent in Mop (Figure 6-a). This additional domain must be placed, in the XO family of enzymes, somewhere along the extended connecting segment (white segment in Figure 3). The FAD binding domain has been tentatively assigned on the basis of mutant studies. A mutation which has received considerable attention is the Tyr395Phe Xanthine dehydrogenase from *Drosophila melanogaster* [53] which was shown to be enzymatically inactive. This residue had been previously shown to be important in the NAD+ binding by the enzyme, by performing chemical modification of this tyrosine in chicken liver XDH [54]. In all cases, these chemical modifications identified the NAD binding site within the insertion found in the Mop sequence [30].

The close relationship between Mop and the xanthine oxidase family of proteins implies a common mechanism of action of these enzymes and essential structural aspects of Mop agree in fact with a large number of experimental data of the XO class of enzymes.

5. Structure based catalytic mechanism

Molybdenum hydroxylases and in particular xanthine oxidases have been investigated by a variety of spectroscopic techniques to gain insight into the mechanism of this class of enzymes. These several aspects have been recently reviewed [5, 6]. In parallel,

much effort has been dedicated to the search for synthetic models of Moco and to the analysis of their structures as well as spectroscopic and functional properties. These model systems and their contribution to the understanding of enzymatic mechanisms have been reviewed [31, 32].

In previous sections we have described relevant features of the Mop structure with important mechanistic implications: (1) The domain organization of the protein and co-factors environment which define a buried catalytic site with unique features; (2) The intramolecular electron transfer among the redox centers, mediated by the pterin cofactor, to which several functions are now clearly associated; (3) The clear definition of the metal coordination sphere, consistent with EXAFS data, as well as the unambiguous location of the catalytically important sulfido molybdenum ligand. The water ligand is revealed for the first time and proposed as the catalytically labile oxygen. The possibility of the water ligand being the source of the labile oxygen is corroborated by recent ^{17}O -EPR studies [55] of model compounds, on which basis a metal bound hydroxide was proposed as the labile site; (4) The isopropanol site, present in the second coordination sphere of molybdenum is used as a valid model for the Michaelis complex of an aldehyde substrate (Figure 9), whereas the carbonyl oxygen replaces the hydroxyl group and the aldehyde hydrogen occupies the methyl group closer to the metal. In this orientation, the carbonyl oxygen establishes two hydrogen bonds with water 137W and with the water ligand, which polarize it. The nucleophilicity of the water ligand is promoted by Glu 869.

The assumption of the isopropanol site as a model for the substrate binding site is supported by several arguments from the literature: Alcohols are substrate-analog inhibitors of Mop [45] as well as of xanthine oxidase [37], while ethylene glycol is a slow substrate of xanthine oxidase [56]. A number of aldehydes are found to inactivate bovine milk xanthine oxidase [57], while reactivation occurs immediately after removing excess of aldehyde. EPR data of xanthine oxidase inhibited with methanol and formaldehyde produced identical "inhibited" signals [58], suggesting similar binding modes for alcohols and aldehydes. The binding of substrate molecules in the second coordination sphere of molybdenum in the Michaelis complex is also supported by spectroscopic data: In the reaction of xanthine oxidase with 2-hydroxy-6-methylpurine (a slowly reacting substrate), no proton coupling due to the C8-H proton is detected in the "rapid type 1" EPR signal [59], although coupling is detected after substrate oxidation and hydride transfer [59, 60]. Also the strong inhibitor 8-bromoxanthine [61] has been shown to interact with xanthine oxidase in a way typical of purine substrates and the Mo-Br distance was found to be larger than 4 Å.

The structure of the Michaelis complex as represented in Figure 9 shows a simple pathway for the enzymatic reaction: In step I, the carbonyl carbon atom suffers nucleophilic attack by the activated water ligand (transferred as OH-), concertedly with hydride transfer to the sulfido group, whereby the carboxylic acid product is generated but remains bound to the molybdenum via the transferred oxygen atom (step II). Bond formation requires a further approach of the atoms involved, possibly via anchoring of the carbonyl oxygen to water 137W, and the aldehyde hydrogen must come closer to the sulfido group. The direct transfer of a hydrogen from substrate (step I) to xanthine oxidase has been detected as a proton from the enzyme strongly coupled to Mo^V in the rapid EPR signal [62]. The close proximity of the carbonyl carbon atom to the metal as in (II), was proposed in the "inhibited" species of xanthine oxidase, by ENDOR studies [63, 64], while EXAFS has indicated product analogs bound to MoIV [14, 15]. In the last step III, the carboxylic acid product is released, which is probably facilitated by a transient binding of Glu 869 to the metal to maintain a 5-fold coordination. The Mo water site may then be regenerated from the chain of internal buried water molecules.

This reaction scheme agrees with proposals for the reaction of xanthine oxidase [6, 65] and provides details on the exact stereochemical environment. However, it differs by suggesting the water ligand, instead of the oxo group (probably present just as the so-called "spectator oxygen", known from molybdenum coordination chemistry [66], as the labile oxygen to be transferred to the substrate, as supported by recent ^{17}O-EPR studies 55 and ^{17}O- and 13C-ENDOR experiments [63, 64] on xanthine oxidase.

References

1. W. Friedrich, P. Knipping, M. Laue, *Sitzungsber. Kgl. Bayerische Akad Wiss.* (1912) 303.
2. J. C. Kendrew, G. Bodo, H. M. Dintzis, R. G. Parrish, H. Wyckoff, *Nature* **181** (1958) 662.
3. R. Huber, P. Reinemer, *Química* **61** (1996) 38.
4. M. J. Romão, *Boletim de Biotecnologia* **53** (1996) 18, and references therein.
5. R. Hille, *Chem Rev* **96** (1996) (in press).
6. R. Hille, *Biochim. Biophys. Acta* **1184** (1994) 143.
7. M. J. Romão, M. Archer, I. Moura, J. J. G. Moura, J. LeGall, R. Engh, M. Schneider, P. Hof, R. Huber, *Science* **167** (1995) 1167.
8. R. Huber, R. Duarte, I. Moura, J. J. G. Moura, J. LeGall, M. Liu, R. Hille, M. J. Romão, *Proc. Natl. Acad. Sci. USA* **93** (1996) 8846.
9. D. C. Rees, J. Kim, M. M. Georgiadis, H. Komiya, A. J. Chirino, D. Woo, J. Schlessman, M. K. Chan, L. Joshua-Tor, G. Santillan, Chakrabarti, Hsu BT, *ACS Symposia* **535** (1993) 170.
10. K. N. Murray, J. G. Watson, S. Chaykin, *J. Biol. Chem.* **241** (1966) 4798.
11. E. I. Stiefel, *ACS Symposia* **535** (1993) 1.
12. R. Hille, *ACS Symposia* **535** (1993) 22.
13. S. P. Cramer, R. Hille, *J. Am. Chem. Soc.* **107** (1985) 8164.
14. R. Hille, G. N. George, M. K. Eidsness, S. P. Cramer *Inorg. Chem.* **28** (1989) 4018.
15. N. A. Turner, R. C. Bray, G. P. Diakun, *Biochem. J.* **260** (1989) 563.
16. H. Schindelin, C. Kisker, J. Hilton, K.V. Rajagopalan, D. C. Rees, *Science* **272** (1996) 1615.
17. F. Schneider, J. Löwe, R. Huber, H. Schindelin, C. Kisker, J. Knäblein, *J. Mol. Biol.* (1996) (in press).
18. S. P. Cramer, J. J. G. Moura, A. V. Xavier, J. LeGall, *J. Inorg. Biochem.* **20** (1984) 275.
19. R. C. Bray, *Quaterly. Rev. Biophysics* **21** (1988) 299.
20. N. Turner, B. A. S. Barata, R. C. Bray, J. Deistung, J. LeGall, J. J. G. Moura, *Biochem. J.* **243** (1987) 755.
21. R. C. Bray, N. A. Turner, J. LeGall, B. A. S. Barata, J. J. G. Moura, *Biochem. J.* **280** (1991) 817.
22. J. L. Johnson, K. V. Rajagopalan, *Proc. Natl. Acad. Sci. USA* **79** (1982) 6856.
23. J. L. Johnson, B. E. Hainline, K. V. Rajagopalan, B. H. Arison, *J Biol. Chem* **259** (1984) 5414.
24. S. P. Cramer, J. L. Johnson, A. A. Ribeiro, D. S. Millington, K. V. Rajagopalan, *J. Biol. Chem.* **262** (1987) 16357 .
25. J. L. Johnson, M. M. Wuebbens, K. V. Rajagopalan, *J. Biol. Chem.* **264** (1989) 13440.
26. K. V. Rajagopalan, J. L. Johnson, *J. Biol. Chem.* **267** (1992) 10199.
27. M. K. Chan, S. Mukund, A. Kletzin, M. W. W. Adams, D. C. Rees, *Science* **267** (1995) 1463.

28. J. L. Johnson, N. R. Bastian, K. V. Rajagopalan, *Proc. Natl. Acad. Aci. USA* **87** (1990) 3190.

29. G. Börner, K. Karrasch, R. K. Thauer, *FEBS Lett.* **290** (1991) 31.

30. U. Thoenes, O. L. Flores, A. Neves, B. Devreese, J. J. V. Beeumen, R. Huber, M. J. Romão, J. LeGall, J. J. G. Moura, C. Rodrigues-Pousada, *Eur. J. Biochem.* **220** (1994) 901.

31. R. H. Holm, *Coord. Chem. Rev.* **100** (1990) 183.

32. J. H. Enemark, C. G. Young, *Adv. Inorg. Chem.* **40** (1993) 1.

33. D. Collison, C. D. Garner, J. A. Joule, *Chem. Soc. Rev.* (1996) 25.

34. R. H. Holm, *Chemistry Rev.* **87** (1987) 1401.

35. M. J. Barber, L. M. Siegel, *Biochemistry* **22** (1983) 618.

36. M. J. Barber, M. P. Coughlan, K. V. Rajagopalan, L. M. Siegel, *Biochemistry* **21** (1982) 3561.

37. D. J. Lowe, M. J. Barber, R. T. Pawlik, R. C. Bray, *Biochem. J.* **155** (1976) 81.

38. T. R. Hawkes, G. N. George, R. C. Bray, *Biochem. J.* **218** (1984) 961.

39. J. J. G. Moura, B. A. S. Barata, *Methods in Enzymology* **243** (1994) 24 .

40. S. Gutteridge, S. J. Tanner, R. C. Bray, *Biochem. J.* **175** (1978) 869.

41. F. F. Morpeth, G. N. George, R. C. Bray, *Biochem. J.* **220** (1984) 235.

42. B. A. S. Barata, J. Liang, I. Moura, J. LeGall, J. J. G. Moura, B. Hanh Huynh, *Eur. J. Biochem.* **204** (1992) 773.

43. J. Caldeira, I. Moura, M. J. Romão, R. Huber, J. LeGall, J. J. G. Moura, *J. Inorg. Biochem.* **59** (1995) 739.

44. T. Tsukihara, K. Fukuyama, M. Nakamura, Y. Katsube, N. Tanaka, M. Kakudo, K. Wada, T. Hase, H. Matsubara, *J. Biochem.* **90** (1981) 1763.

45. B. A. S. Barata, J. LeGall, J. J. G. Moura, *Biochemistry* **32** (1993) 11559.

46. B. Fischer, H. Schmalle, E. Dubler, A. Schäfer, M. Viscontini, *Inorg Chem* **34** (1995) 5726.

47. E. I. Stiefel, K. F. Miller, A. E. Bruce, J. L. Corbin, J. M. Berg, K. O. Hodgson, *J. Am. Chem. Soc.* **102** (1980) 3624.

48. S. J. N. Burgmayer, A. Baruch, K. Kerr, K. Yoon, *J. Am. Chem. Soc.* **111** (1989) 4982.

49. S. J. N. Burgmayer, M. R. Arkin, L. Bostick, S. Dempster, K. M. Everett, H. L. Layton, K. E. Paul, C. Rogge, A. L. Rheingold, *J. Am. Chem. Soc.* **117** (1995) 5812.

50. S. J. N. Burgmayer, K. Everett, L. Bostick, *ACS Symposia* **535** (1993) 114.

51. S. Gardlik, K. V. Rajagopalan, *J. Biol. Chem.* **265** (1990) 13047.

52. S. Gardlik, K. V. Rajagopalan, *J. Biol. Chem.* **266** (1991) 4889.

53. W. A. Doyle, J. F. Burke, A. Chovnick, F. L. Dutton, C. Russell, J. R. S. Whittle, R. C. Bray, *Biochem. Soc. Trans.* **24** (1996) 31S .

54. T. Nishino, T. Nishino, *J. Biol. Chem.* **264** (1989) 5468 .

55. R. J. Greenwood, G. L. Wilson, J. R. Pilbrow, A. G. Wedd, *J. Am. Chem. Soc.* **115** (1993) 5385.

56. S. J. Tanner, R. C. Bray, *Biochem. Soc. Trans.* **6** (1978) 1331.

57. F. F. Morpeth, R. C. Bray, *Biochemistry* **23** (1984) 1332.

58. F. M. Pick, M. A. McGartoll, R. C. Bray, *Eur. J. Biochem.* **18** (1971) 65.

59. R. Hille, J. H. Kim, C. Hemann, *Biochemistry* **32** (1993) 3973.

60. S. Gutteridge, S. J. Tanner, R. C. Bray, *Biochem. J.* **175** (1978) 887.

61. R. Hille, R. C. Stewart, *J. Biol. Chem.* **259** (1984) 1570.

62. R. C. Bray, G. N. George, *Biochem. Soc. Trans.* **13** (1985) 560.

63. B. D. Howes, R. C. Bray, R. L. Richards, N. A. Turner, B. Bennett, D. J. Lowe, *Biochemistry* **35** (1996) 1432.

64. D. Howes, B. Bennett, R. C. Bray, R. L. Richards, D. J. Lowe, *J. Am. Chem. Soc.* **116** (1994) 11624.

65. H. Kim, M. G. Ryan, H. Knaut, R. Hille, *J. Biol. Chem.* **271** (1996) 6771.

66. K. Rappé, W. A. III Goddard, *J. Am. Chem. Soc.* **104** (1982) 3287.

67. M. J. Romão, B. A. S. Barata, K. Lobeck, I. Moura, M. A. Carrondo, J. LeGall, F. Lottspeich, R. Huber, J. J. G. Moura, *Eur. J. Biochem.* **215** (1993) 729.

68. D. J. Lowe, R. M. Lynden-Bell, R. C. Bray, *Biochem. J.* **130** (1972) 239.

69. (a) V. N: Gladyshev, J. C. Boyington, S. V. Khangulov, D. A. Grahame, T. C. Stadtman, P. D. Sun *J Biol Chem* **271**(1996) 8095. (b) J. C. Boyington, V. N. Gladyshev, T. C. Stadtman, P. D. Sun IUCr XVII Congress of the International Union of Crystallography (1996).

Catalysis in fine chemicals production

A catálise nas indústrias de química fina

A.E. VAN DIEPEN*, A.C.J.M. VAN DE RIET AND J. A. MOULIJN

'DEPARTMENT OF CHEMICAL ENGINEERING, CPT-STM, DELFT UNIVERSITIY OF TECHNOLOGY, JULIANALAAN 136, 2628 BL DELFT, THE NETHERLANDS

Catalysis in fine chemicals production is still slightly in the development stage. Traditionally, production of fine chemicals takes place in batch reactors, and consists of many stoichiometric reactions, which yield a lot of by-products. The use of catalysts can markedly improve selectivities. Two examples are discussed in this article, both using reactor types which are unconventional in fine chemicals production. The first example is the selective hydrogenolysis of CFC-12 (CCl_2F_2) to HFC-32 (CH_2F_2) with carbon supported palladium as the catalyst. It has been shown that a continuous process for this reaction is technically and economically feasible. The reactor used is a cooled multitube fixed bed reactor because of the high exothermicity of the reaction. The second example demonstrates the use of a novel reactor type, viz. a monolithic reactor, in fine chemistry. The monolithic catalyst has been tested for the selective hydrogenation of benzaldehyde to benzyl alcohol. High selectivities are obtained, and the activity is in the normal range for industrial chemical processes.

A utilização de catalisadores em Química está ainda em fase de desenvolvimento. Tradicionalmente, os produtos da Química Fina são obtidos em reactores fechados, por meio de muitas reacções estequiométricas que originam uma grande quantidade de subprodutos. O uso de catalisadores pode melhorar substancialmente as selectividades. Neste artigo discutem-se dois exemplos, em que se utilizam reactores de tipo não convencional em Química Fina. O primeiro exemplo trata da hifrogenólise selectiva de CFC-12 (CFC-12 (CCl_2F_2) a HFC-32 (CH2F2) usando um catalisador de paládio suportado em carbono. Demonstrou-se que um processo contínuo para esta reacção é técnica e economicamente viável. O reactor usado é um leito fixo multitubular com arrefecimento, devido à elevada exotermicidade da reacção. O segundo exemplo demonstra o uso de um novo tipo de reactor, o reactor monolítico, em Química Fina. O catalisador monolítico foi testado na hidrogenação selectiva de benzaldeído a álcool benzílico. Obtiveram-se selectividades elevadas, com uma actividade na gama normal para os processos químicos industriais.

1. General Introduction

Traditionally, chemical engineers have been mainly involved in bulk processes. Novel processes have been put in practice, and it is clear that chemical engineers have been successful. Also in environmental catalysis the chemical engineering community has contributed visibly, a noticeable example being the catalytic converter used in car exhaust gas cleaning. Less attention has been paid to fields where the production volumes are smaller, and the chemical complexity is higher, e.g., in the production of pharmaceuticals and agrochemicals. However, also in these areas the chemical reaction engineering approach is useful. This area is called 'Fine chemistry'.

1.1. Comparison of fine and bulk chemicals

Fine chemicals differ from bulk chemicals in many respects, as shown in Table 1 (the limits are chosen slightly arbitrarily). Specific for fine chemistry is also that relatively large amounts of by-products are formed (Table 2 [1]). It is clear that in realizing improved processes, large steps can be made. For instance, improved selectivities not only reduce the amount of by-products formed (less waste disposal), but also facilitate product separation.

1.2. Developments in Fine Chemicals Production

A trend in fine chemistry is the increasing interest in the production of compounds with high purity, especially optically pure compounds. In pharmaceuticals it often cannot be considered safe to apply mixtures of the optical isomers. It is possible that only one isomer is active for the desired purpose, while the other isomers are inactive or even have a damaging effect. In fine chemistry, catalysis does not play the important role it does in the production of bulk chemicals. Multi-step synthesis reactions usually consist of a number of

Table 1. Fine versus bulk chemicals.

	Fine chemicals	Bulk chemicals
Price	> 5$/kg	< 5$/kg
Volume	< 10 kt/y	> 10 kt/y
Product variety	hight	low
Chemical complexity	hight	low
Added value	hight	low
Synthesis	multi stop	few steps
Catalysis	exception	often
Raw materials and energy consumption	hight	low
By-products	hight	low
Toxic compounds	often (e.g. phosgene, HCN)	exception
Plants	often MPP*	dedicated
	usually batch	often continuous
Investment	low ($)	hight ($)
	hight ($/kg)	low ($/kg)
Labor	hight	low
Market fluctuations	hight	low

* MPP = multi product/purpose plant

stoichiometric reactions rather than catalytic reactions. Examples are:

– Hydrogenation by a mixture of a metal and an acid;
– Oxidation by permanganate;
– Friedel-Crafts alkylation.

Such reactions always will lead to high amounts of by-products. Figure 1 shows the Friedel- Crafts alkylation of benzene with 2-propylchloride to yield cumene. The reaction scheme shows that equimolar quantities of HCl and $Al(OH)_3$ are formed. Furthermore, the cumene formed is more reactive towards alkylation than benzene itself. As a result, as soon as cumene starts to accumulate in the reaction mixture, it undergoes further alkylation to give di- and even trisubstituted products. So, large amounts of by-products are formed. Catalytic processes are much more selective, and do not produce this many by-products. Therefore, it is not surprising that catalysis is more and more applied in fine chemistry.
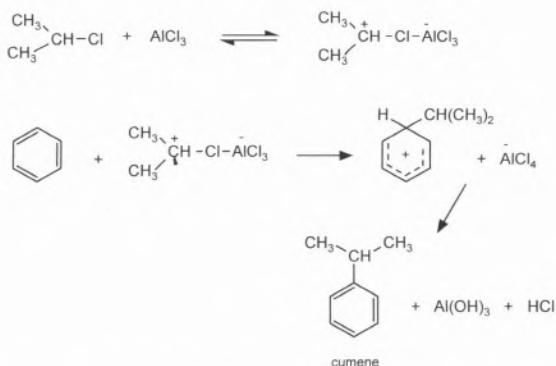
Figure 1 – Friedel-Crafts alkylation of benzene with 2-propylchloride

Another trend in fine chemistry is the use of reactants which do not produce by-products with unfavourable properties. For instance, oxidation with permanganate is unattractive in this respect. Examples of attractive reactions are oxidations carried out with O_2, H_2O_2 and organic peroxides, e.g., tert-butyl-hydroperoxide: $(CH_3)_3$-C-O-O-H. These oxidation reactions often have to be catalyzed.

Table 2. Production and by-product formation in various sectors of industry [1].

Industry segment	Product tonnage	kg by-product/ /kg product
Oil refining	$10^6 - 10^8$	ca. 0.1
Bulk Chemicals	$10^4 - 10^6$	< 1 - 5
Fine Chemicals	$10^2 - 10^4$	5 - 50
Pharmaceuticals	$10 - 10^3$	25 - > 100

1.3. Process Development and Reactor Design

Catalysis can markedly improve selectivities in fine chemistry. Use of catalysts also can significantly reduce the use of chemicals which produce unattractive by-products (e.g. salts). Process-integrated catalysis can play an important role in the design and development of processes for the production of fine chemicals. Figure 2 shows the levels involved in process development. In conventional process development, one starts with research on the micro level, and then with time, proceeds via meso- and macro level to the ultimate industrial plant. Traditionally, the micro level is the area of chemists, whereas the meso and macro levels are reserved for chemical engineers. However, integration of all three levels, meaning close cooperation between

MACRO
process design

MESO
particles, reactors
reactor selection, design

MICRO
sites, molecules, intermediates
kinetics
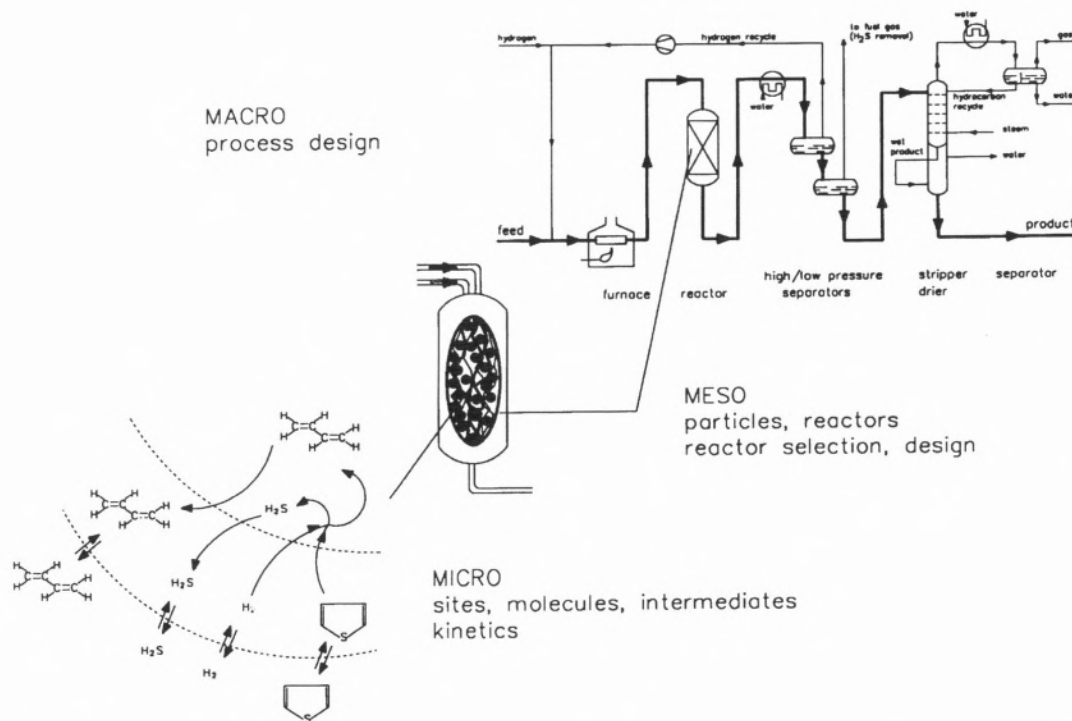
Figure 2 – Levels in process development

chemists and chemical engineers, could speed up process development to a great extent. For instance, adequate kinetic studies can reveal important process information (selection of recycle streams, reactor type, etc.) at an early stage.

For every production process the choice and design of the reactor is the key to a succesful process. Reactor design requires information on:

– Chemical kinetics;
– Heat and mass transfer, reactor hydrodynamics.

The workhorse in fine chemistry generally is the (semi) batch reactor, which essentially is a well stirred tank. In general, the temperature, and concentrations of reactants and products will change significantly in going from laboratory to full scale reactor. Therefore, it is not surprising that selectivities often change upon scale up, especially in complex reactions. Another risk is the occurrence of a run-away, i.e. due to the smaller area/volume ratio, heat is not dissipated at a high enough rate in the large reactor, leading to excessive temperature rise. Both phenomena are illustrated in Figures 3 and 4.

Batch and semibatch reactors are not suitable for fast and highly exothermic reactions. Furthermore, they are usually not appropriate for gas phase reactions. In this paper two non-conventional examples will be given, illlustrating the use of other reactor types. The first is an example of selective hydrogenolysis, the conversion of
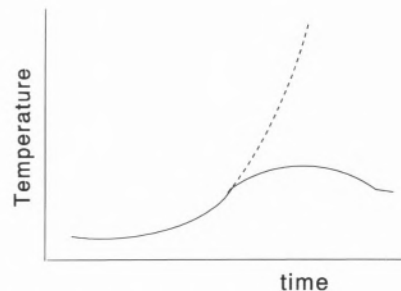
Figure 3 – Temperatures profiles; — = normal (smal scale); - - - = runaway (large scale).
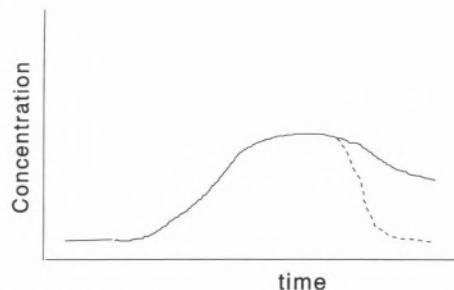
Figure 4 – Selectivity loss (concentration of P, the desired product, is shown); – = normal condition (small scale); - - - = runaway condition (large scale)

CCl_2F_2 into CF_2H_2. This process has been developed based on a multitube fixed bed reactor configuration. The second example illustrates the use of a novel reactor type, viz. a monolithic reactor, for application in fine chemistry. The selective hydrogenation of benzaldehyde into benzyl alcohol has been chosen as a model reaction.

The presence of recycle streams complicates process design. Impurities may build up in recycle streams, and moreover, cause catalyst deactivation. It is important that all impurities (either introduced with feed streams or formed as by-products) are identified and their influence on process performance determined. For instance, it has been determined that methane, which is formed as a by-product in the CCl_2F_2 conversion process (see below), and is present in the hydrogen recycle stream, deactivates the catalyst. Therefore, the concentration of methane must be limited by purging it.

2. The selective hydrogenolysis of CCl_2F_2 into CF_2H_2

2.1. Introduction

Chlorofluorocarbons (CFCs) until recently were produced for use in amongst others refrigeration applications. Technically, they possess very favorable properties, and, moreover, they are low-priced chemicals. So, it is not surprising that CFCs found an ever increasing market. However, it is now generally accepted [2] that fully halogenated CFCs are responsible for the depletion of the ozone layer, and that they contribute to the greenhouse effect. World-wide, production and consumption of CFCs is being terminated, but considerable amounts are still present (estimated [3] 2.25 Mton, with CCl_2F_2 and CCl_3F accounting for about 45% each). Recovery and subsequent destruction of these substances is a logical step. Many destruction techniques have been proposed [3-8], but only combustion has been applied on a commercial scale. Obviously, the conversion of CFCs into valuable chemicals is much more desirable. At Delft University of Technology, a catalytic process is under development in which CCl_2F_2 (CFC-12) is converted into CH_2F_2 (HFC-32), which is an ozone-friendly refrigerant [9].

2.2. Reactions

The reaction to be carried out is the hydrogenolysis of CCl_2F_2.

$$CCl_2F_2 + 2 H_2 \rightarrow CH_2F_2 + 2 HCl \qquad \Delta H_r^{298} = -156 \text{ kJ/mol}$$

The reaction enthalpy shows that the reaction is very exothermic. An important side reaction is the formation of methane, which is even more exothermic:

$$CCl_2F_2 + 4 H_2 \rightarrow CH_4 + 2 HCl + 2 HF \qquad \Delta H_r^{298} = -319 \text{ kJ/mol}$$
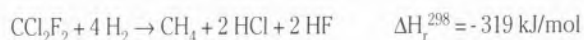
CCl_2F_2 belongs to the family of halogenated methanes. Figure 5 [10] shows all the possible C_1 derivates containing Cl, F, and H. The arrows indicate the thermodynamic stability (e.g. CCl_4 least stable, CH_4 most stable), and not necessarily a reaction sequence. Initially, it was anticipated that the conversion of CCl_2F_2 would proceed through a serial kinetic scheme, with $CHClF_2$ as intermediate. Other hydrogenolysis reactions, such as the hydrogenolysis of aldehydes [11], and acid chlorides [12], and also benzene hydrogenation [13,14] indeed proceed through a consecutive mechanism. All hydrogenolysis reactions starting from CCl_2F_2 are exothermic irreversible reactions. Although thermodynamically the reaction of CCl_2F_2 proceeds via $CHClF_2$, CH_2ClF, CH_3F, and finally methane, a reaction towards CH_2F_2 might be hoped for (provided that a selective catalyst is available), because the carbon-fluorine bond is much stronger than the carbon-chlorine bond [15].
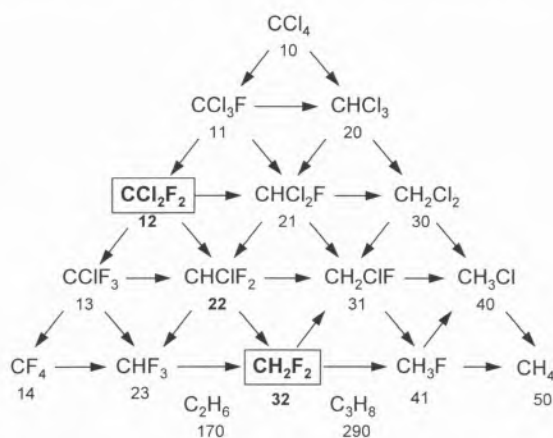
Figure 5 – Thermodynamic relation between chlorinated and fluorinated methanes. The direction of the arrows indicates the thermodynamic stability at 298 K and atmospheric pressure [10]

2.3. Experimental Results

Several noble metals on activated carbon supports have been tested for their catalytic activity. Palladium was found to be the most suitable noble metal for the CCl_2F_2 hydrogenolysis reaction [16]. Pretreatment of the activated carbon support material is important. Washing with aqueous sodium hydroxide, aqueous hydrochloric acid, and water serves to remove impurities [17,18]. The main product formed in the catalytic hydrogenolysis of CCl_2F_2 is CH_2F_2, although significant amounts of $CHClF_2$ and methane are also formed. The results reported here are steady-state values.

The effect of washing of the activated carbon support is evident from Figure 6 [17]. Both conversion and selectivity towards CH_2F_2 increase. The formation of CHF_3 and the lower alkanes C_2H_6 and C_3H_8 are
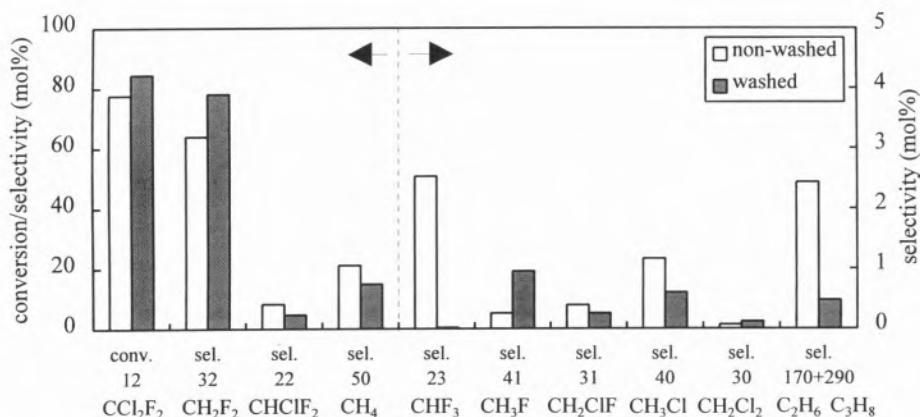
Figure 6 – Performance at 510 K of Pd (2 wt%) catalyst on a non-washed and a washed activated carbon in the hydrogenolysis of CCl_2F_2 [17]

strongly suppressed. Washing of the activated carbon removes impurities such as iron and aluminium, which can act as Friedel-Crafts catalysts. These metals catalyze the undesired chlorine/fluorine exchange reactions, such as $CHClF_2 \rightarrow CHF_3$, and $CH_2F_2 \rightarrow CH_2ClF$. Iron also catalyzes the formation of CH_4, and the lower alkanes [17].

The results reported below have all been obtained with palladium on a washed activated carbon support. Figure 7 [10] shows the catalytic behaviour of the palladium catalyst for the hydrogenolysis of CCl_2F_2 as a function of temperature. The results are striking: The selectivity only changes slightly with temperature, while the conversion increases exponentially from 0 to 100% over the temperature range.

The hydrogenolysis reactivity of $CHClF_2$ and CH_2F_2 has also been evaluated. Figure 8 [10] shows the results, which indicate that the reactivity of $CHClF_2$ and CH_2F_2 is much smaller than the reactivity of CCl_2F_2. This result is important because it indicates that CH_2F_2, the most important product in hydrogenolysis of CCl_2F_2, is not formed via a reaction network of the type:

$$CCl_2F_2 \quad \overset{H_2}{\leftrightarrow} \quad CHClF_2 \quad \overset{H_2}{\leftrightarrow} \quad CH_2F_2 \quad \overset{H_2}{\leftrightarrow} \quad etc.$$
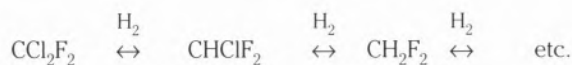
If this would have been the case, the conversion of $CHClF_2$ would have been of the same order as that of CCl_2F_2. The consequence for process development is evident: it is not useful to recycle the $CHClF_2$ formed.

HCl is an important product of the reaction. A large amount of HCl was added to determine the influence of chlorine on the reaction. Figure 9 [10] shows the effect on conversion and selectivity. HCl not only inhibits the CCl_2F_2 conversion, it also significantly affects the selectivities. The selectivity towards $CHClF_2$ increases at the expense of CH_2F_2. The selectivity towards CH_4 remains approximately constant.

2.4. Reaction Mechanism

Figure 10 shows a simplified reaction mechanism accounting for the most significant products [10]. The reaction involves the competitive adsorption of CCl_2F_2, HCl, and hydrogen. The first step is dissociative adsorption into $CClF_2$ or CCl_2F. Because of the greater strength of the carbon-fluorine bond [15], mainly $CClF_2$ will be formed.

The selectivity for CH_2F_2 and $CHClF_2$ depends on the amounts of chlorine and hydrogen present on the surface. More chlorine means an increased formation of $CHClF_2$ (see also Figure 9), whereas a higher hydrogen concentration results in the formation of more CH_2F_2 [15]. The high selectivity towards CH_2F_2 can be explained by the stability of the adsorbed difluorocarbene
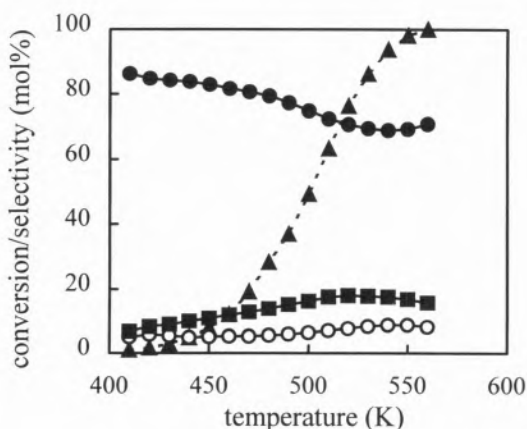
Figure 7 – Conversion (triangles) and selectivity in the hydrogenolysis of CCl_2F_2 over 1 w% Pd/C as a function of temperature to CH_2F_2 (filled circles), $CHClF_2$ (squares), and CH_4 (open circles). Conditions: WHSV = 1 g/(g·h), $H_2/CCl_2F_2 = 3$, p = 0.3 Mpa [10].
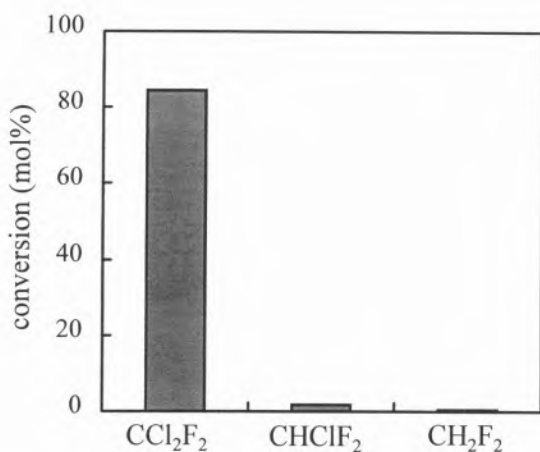
Figure 8 – Comparision of the reactivity of CCl_2F_2, $CHClF_2$, and CH_2F_2 in the catalytic hydrogenolysis over 2 g of 2 wt% Pd/C. Conditions: T= 510 K, H_2/CFC = 3, p = 0.3 MPa, feed = 16.5 mmol/h [10]

(CF_2) [15]. Readsorption of both products on the catalyst does not occur (or only to a very small extent), as can be concluded from the small reactivity of $CHClF_2$ and CH_2F_2 towards hydrogenolysis (Figure 8). It has been suggested that CH_4 is formed via a parallel pathway, namely via CCl_2F and CH_3 on the catalyst surface[10]. Evidence of this reaction pathway stems from the observation of small amounts of other products such as CH_2Cl_2, CH_3Cl, and $CHClF_2$ [10]. Also, the selectivity towards CH_4 is unaffected by HCl addition, which does influence the primary reaction pathway.
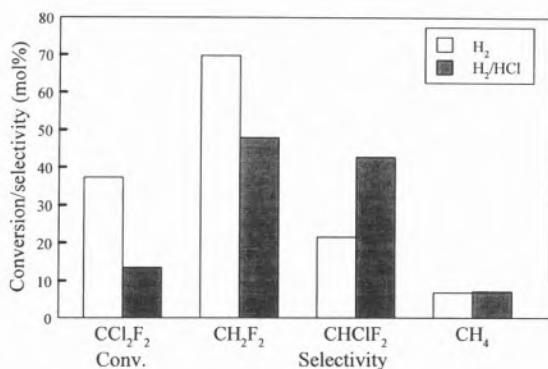
Figure 9 – Influence of HCl on hydrogenolysis reaction. Conditions: T= 510 K, H_2/CCl_2F_2= 3 mol/mol, WHSV=1 g/g.h, p=0.2 Mpa, HCl/H_2=1 mol/mol [10]

2.5. Process design

A preliminary process design has shown that a continuous CFC-destruction process based on the Pd catalyst is technically, and economically feasible [19]. Figure 11 [19] shows a possible configuration. Oil,

water, and $CClF_2$-CF_3 (R-115), which may have been introduced in the CCl_2F_2 feed during its recovery, have to be removed. Oil and water might cause problems with the catalyst and corrosion of process equipment, while CHF_2-CF_3 (R-125), the hydrogenolysis product of $CClF_2$-CF_3, complicates separation because it forms an azeotrope with CH_2F_2 [19]. $CHClF_2$ is also removed. Approximately 80% of the CCl_2F_2 fed to the reactor is converted. Acids, mainly HCl, but also some HF which is formed simultaneously with methane, are removed prior to light ends separation. It has been shown [10] that a high hydrogen/CCl_2F_2 ratio increases the conversion and selectivity towards CH_2F_2. The presence of methane in principle deactivates the catalyst, mainly due to coke formation [19]. However, if the excess hydrogen is high enough ($\approx$ 6 - 10 mol/mol CCl_2F_2), some methane is allowed [19]. The excess hydrogen is recycled, together with light products such as methane and ethane which inevitably end up in this recycle stream. In order to control their concentrations, a purge stream is required. From the experimental results it is apparent that $CHClF_2$ should not be recycled to the reactor. The product CH_2F_2 is separated from CCl_2F_2 and $CHClF_2$, which are recycled to the pretreatment section.

When the process is to be applied in an industrial plant, the reactor will be a multi-tubular fixed bed reactor (6600 tubes of $\approx$20-30 mm) because of the exothermicity of the reaction (standard heat of reaction -156 kJ/mol, standard heat of reaction for the formation of methane - 319 kJ/mol). Cooling is performed by means of boiling water. Temperature control is very important to prevent runaways and to protect the catalyst. For this reason a fixed bed reactor with intermediate quench cooling, as used in for instance ammonia synthesis, is not suitable; Due to the high conversion (80 %) which is obtained, a lot of heat is evolved, and hot spots might easily occur.
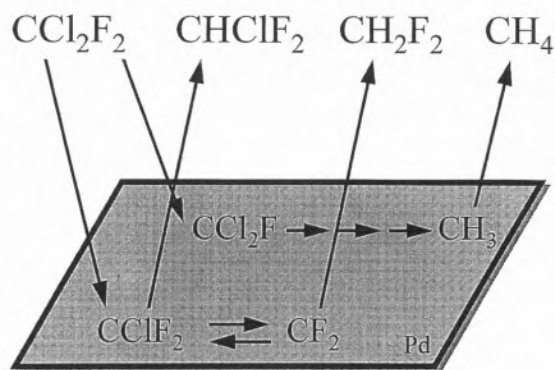
Figure 10 – Simplified reaction mechanism for the selective hydrogenolysis of CCl_2F_2 [10].
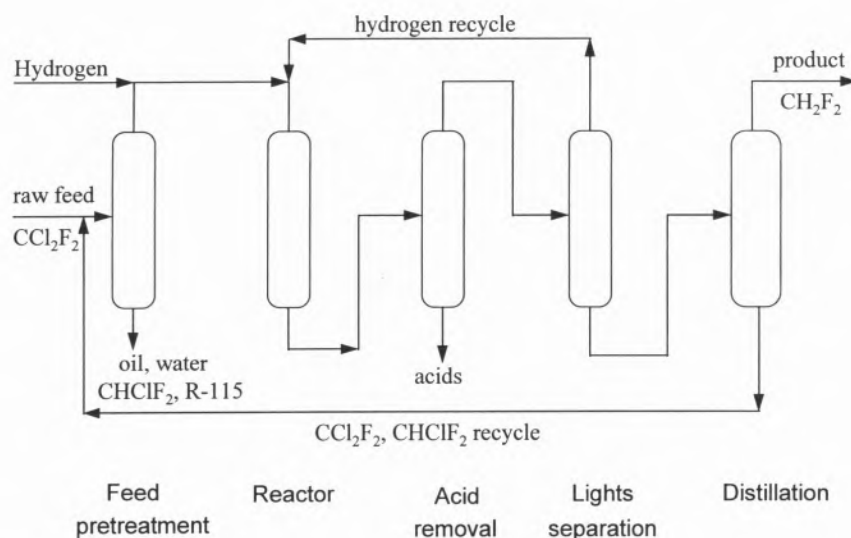
Figure 11 –Process lay out for the conversion of CCl_2F_2 to CH_2F_2 [19].

2.6. Conclusions regarding CCl_2F_2 hydrogenolysis

The main product of hydrogenolysis of CCl_2F_2 is CH_2F_2. The most important by-products are $CHClF_2$ and CH_4. Pd on purified activated carbon is an excellent catalyst for this reaction. With this catalyst high conversions and selectivities are obtained. Parallel rather than consecutive reactions lead to the formation of CH_2F_2, $CHClF_2$, and CH_4. Therefore, in an industrial process, recycling of $CHClF_2$ is not useful to increase the CH_2F_2 yield. Similarly, recycling of HCl decreases conversion and selectivity towards CH_2F_2. A high hydrogen to CCl_2F_2 ratio is required. Therefore, a hydrogen recycle is introduced, which inevitably contains some methane. Based on catalyst performance studies, it can be concluded that a small amount of methane is acceptable.

It is clear that mechanistic/kinetic studies yield important process data. Integration of catalyst research and process design can significantly speed up process development, e.g. the selection of recycle streams to be used in process development follows from the reaction mechanism. Furthermore, catalyst performance studies show that total methane removal is not necessary.

3. Selective hydrogenation of benzaldehyde to benzyl alcohol using nickel/alumina monolithic catalysts

3.1. Introduction

A monolithic catalyst is an example of a structured catalyst. The support is made of either ceramics or metal and consists of a large number of narrow parallel channels (Figure 12). The channel walls are typically covered by a thin layer of a porous oxide. This layer, the washcoat, serves as the catalyst carrier.

Monoliths have found wide application in the treatment of automotive exhaust gases and industrial off-gases. The monolithic structure provides low pressure drops, large external surface areas, and short diffusion distances. These features make monoliths suitable for solid-catalyzed gas-liquid reactions as well. The interest in three-phase monolith reactors is focused on three main fields of applications: hydrogenations, oxidations and biotechnology applications. The use of monoliths in heterogeneous catalysis has been reviewed by Cybulski and Moulijn [20].

Liquid-phase hydrogenations are common industrial processes. Conventional hydrogenation reactors are slurry and trickle-bed reactors. Monolith reactors have some attractive features compared to these conventional reactors. Currently, a commercial three-phase hydrogenation process using monolithic catalysts is operative. Eka Nobel AB, AKZO-Nobel uses a monolith reactor for the hydrogenation of 2-ethylanthraquinone [21, 22], which is part of the anthraquinone process for hydrogen peroxide manufacture.

The objective of this study is to demonstrate the potential of monolithic catalysts in the production of fine chemicals. The hydrogenation of benzaldehyde to benzyl alcohol was chosen as a test reaction.
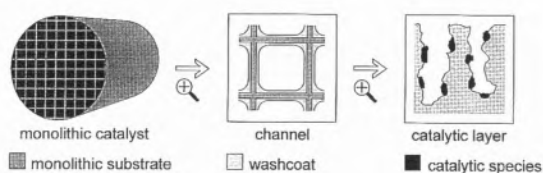
Figure 12 – Monolithic catalyst

3.1.1. Monoliths versus Conventional Reactor Types

In three-phase catalytic reactors hydrodynamics play an important role in bringing about the contact between the phases. The performance of a monolith reactor is therefore highly dependent upon the flow pattern in the monolithic channels. The most important flow regime is Taylor (or segmented) flow. This flow pattern consists of liquid slugs separated from each other by gas slugs (Figure 13 [23]). The gas slug is separated from the channel wall by a very thin liquid film. This thin liquid film provides low axial dispersion and low mass transfer resistance from the gas/liquid interface to the channel wall. Mass transfer is further enhanced by the forced recirculation within the liquid slugs.
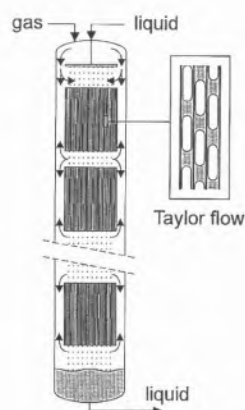
Figure 13 – Monolith reactor with internal gas recirculation

In a slurry reactor (Figure 14a) the catalyst is present in the form of small particles (1-200 μm). The particles are kept in suspension by mechanical stirring or by the gas flow. A main advantage is the short diffusion distance in the catalyst, resulting in high effectiveness factors. Major disadvantages of a slurry reactor are problems connected with agitation (e.g. catalyst attrition), catalyst separation, and scale-up. By using a monolith reactor these problems are avoided.

In a trickle-bed reactor (Figure 14b) the catalyst particles with sizes in the range of 1-3 mm constitute a stationary bed. Both gas and liquid flow downwards through the bed. The gas-phase forms the continuous phase. The liquid flows over the catalyst particles in the form of a film. Main advantages are the high catalyst loading and the trivial catalyst separation. Major disadvantages are the high pressure drop over the bed and the problems connected with flow maldistribution (e.g. cooling and thermal runaways). In a monolith reactor the pressure drop is much lower. Main characteristics of monolith, slurry and trickle-bed reactors are given in Table 3 [24].

An additional advantage of a monolith reactor is the relative ease of scale-up. Each channel can be seen as a reactor on its own, which means that scale-up essentially comes down on multiplying the number of channels. However, crucial for the performance of the reactor is a proper distribution of the fluid over the cross-section of the monolith. Since there is no radial connection between the channels a non-uniform inlet distribution will be propagated throughout the channels. Grolman et al. [25] showed that the distribution is significantly enhanced by the presence of a foam layer on top of the monolith.

It is even possible to operate the reactor with a pump free internal gas recirculation (Figure 13 [23]). The liquid plugs formed in the Taylor flow regime automatically entrain gas. The fluids are driven through the channels by gravity, resulting in a very low pressure drop over the monolith. This enables internal gas recirculation.

Monolith reactors also have some drawbacks. Main disadvantages are the necessity of a uniform inlet distribution, the higher cost of monoliths and the short residence time of the reactants in the monolith channels. The latter however, can be an advantage for very fast reactions.
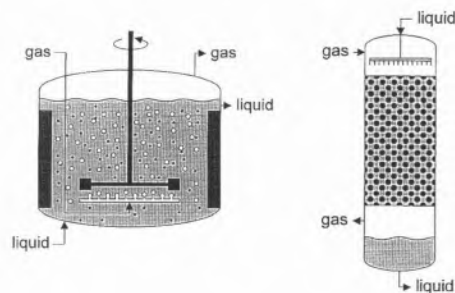
Figure 14 – Conventional reactors; a: stirred slurry reactor, b) Trickle-bed reactor.

3.1.2. Benzyl alcohol production

Benzyl alcohol is mainly used in the photographic and textiles industry, but also finds many applications as an intermediate for the production of fine chemicals. Benzyl alcohol itself can also be regarded a fine chemical; plant capacities are in the order of 2 kton/year [26]. It can be produced in many ways but at present only two processes are of industrial importance, namely hydrolysis of benzyl chloride, and hydrogenation of benzaldehyde [27]. The latter process is currently performed in a slurry reactor in batch-mode. A continuous process is also known [27].

Depending on the reaction conditions benzaldehyde can be hydrogenated to form benzyl alcohol, toluene, hydroxymethylcyclohexane, benzene and methane. However, with suitable reaction conditions and a catalyst a high benzyl alcohol yield can be obtained.

Table 3. Comparison between typical monolith, slurry and trickle-bed reactors.

Property	Monolith	Agitated slurry	Trickle-bed
Particle/channel diameter [mm]	1.1-2.3	0.01-0.1	1.5-6.0
Volume fraction of catalyst	0.07-0.15	0.005-0.01	0.55-0.6
External surface area [m2/m3]	1500-2500	300-6000	600-2400
Diffusion distance [μm]	20-150	5-50	100*-3000
Superficial liquid velocity [m.s^{-1}]	0.1-0.45	-	0.001-0.02
Superficial gas velocity [m.s^{-1}]	0.01-0.35	0.03-0.5	0.15-3.0
Pressure drop [kPa.m^{-1}]	3.0	6.0	50.0
Mass transfer			
gas-liquid, $k_L a$ [s^{-1}]	0.05-0.30	0.01-0.6	0.06
liquid-solid, $k_s a_s$ [s$_{-1}$]	0.03-0.09	1-4	0.06

* Egg shell catalyst

3.2. Experimental

A series of nickel monolithic catalysts with varying nickel load was prepared. Nickel was applied on the alumina washcoated monoliths by deposition-precipitation. The activity and selectivity of the catalysts was tested in the liquid-phase hydrogenation of benzaldehyde to benzyl alcohol in an internal recycle reactor of the Berty type.

3.2.1. Nickel loading

Nickel was applied on alumina washcoated monoliths. A deposition-precipitation method [28] was used to obtain a uniform distribution of the catalyst precursor over the support. Redistribution of the precursor during the drying phase is prevented by fixating it to the support prior to drying.

The monolith (dried at 363 K) was placed in a solution of nickel nitrate and urea, the latter in slight excess. The solution was heated to about 353 K and kept at this temperature during the reaction time. Urea then hydrolyses under the formation of hydroxyl-ions, according to:

$$NH_2CONH_2 + 3 H_2O \rightarrow 2 NH_4^+ + CO_2 + 2 OH^-$$
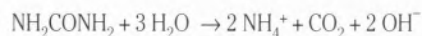
Nickel is deposited as nickel hydroxide, which is anchored by reaction to the surface OH-groups of the alumina washcoat:

$$Ni(OH)^+ + AlOH + OH^- \rightarrow AlONi(OH) + H_2O$$

After drying at 363 K, the monolith was calcined in air at 723 K for 2 hours.

3.2.2. Catalyst characterization

The specific surface area of the alumina washcoat was determined according to the BET method by nitrogen physisorption at 77 K.

The amount of nickel applied was determined from the weight increase of the monolith upon deposition-precipitation and calcination. It is assumed that this increase corresponds to NiO. The reducibility of the nickel species was investigated with temperature-programmed reduction (TPR). The nickel surface area was determined by hydrogen chemisorption.

3.2.3. Catalyst testing

The activity and selectivity of the monolithic catalysts were tested in the hydrogenation of benzaldehyde to benzyl alcohol (Figure 15). The most important side reaction is the hydrogenolysis of benzyl alcohol to toluene and water.
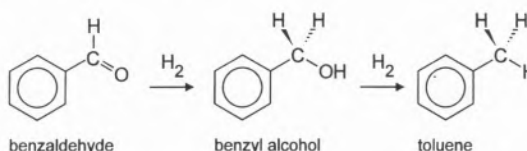
Figure 15 – Hydrogenation of benzaldehyde to benzyl alcohol.

An internal recycle reactor of the Berty type was used. A schematic representation of the reactor is given in Figure 16. The monolith was placed in the draft tube centered above the bottom-entering vane-type blower. The gas/liquid mixture flowed upwards in the baffled annulus between the draft tube and the vessel wall and returned downwards through the monolith. The reactor-vessel is surrounded by an oven which allowed the temperature in the reactor to be controlled within ± 1 K. The reactor was operated batchwise with respect to the liquid phase. Hydrogen was supplied at the rate it was consumed.
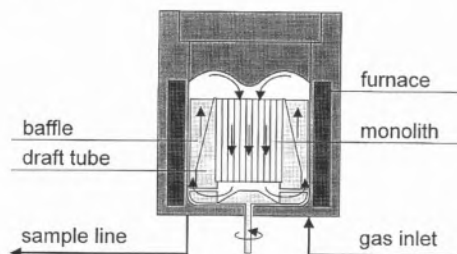
Figure 16 – Berty reactor.

3.3. Results and discussion

3.3.1 Loading and characterization of nickel catalyst

Nickel was applied on commercial alumina washcoated monolithic supports. The characteristics of the support are given in Table 4. Three nickel monolithic catalysts with increasing nickel load were prepared: M1 (1.1 wt% Ni), M4 (4.2 wt% Ni) and M7 (7.2 wt% Ni). Table 5 shows the characteristics of the deposition-precipitation experiments.

Table 4. Characteristics of monolithic support.

Substrate		
Material	cordierite	
Length	3.9	[cm]
Diameter	3.7	[cm]
Volume	42	[cm^3]
Cell density	62	[cells/cm^2]
Washcoat		
Material	Al$_2$O$_3$	
Amount	0.1	[g/cm^3]
S$_{BET}$	17.1	[m^2/g support]

Table 5. Characteristics of the deposition-precipitation experiments.

Monolith	Concentration [mol/l]		t [h]	Ni load [wt%]	
	Ni(NO$_3$)$_2$	Urea		total	(in washcoat)
M1	0.27	0.29	6.15	1.1	(8.1)
M4	1.06	1.15	5.25	4.2	(26.0)
M7	2.12	2.30	4.55	7.2	(46.0)

Table 6. Hydrogen chemisorption results.

Monolith	S$_{Ni}$	D	d$_{vs}$
	[m^2/g total]	[%]	[nm]
M1	0.38	5.2	≈ 20
M4	1.0	3.6	≈ 30
M7	0.39	(≈ 0.8)	(≈ 150)

Table 6 shows the hydrogen chemisorption results. The dispersion is lowest for the monolith with the highest nickel loading, i.e. 7 wt% corresponding to almost 50 wt% on a washcoat basis. The dispersion increases with decreasing nickel load. For all three catalysts the nickel particles are relatively large, which indicates that they are mainly deposited at the external surface of the washcoat.

The catalysts were reduced ex-situ in a TPR set-up. After reduction the monolith was cooled to 313 K under a nitrogen flow. Then it was passivated by contacting it with air. The TPR-profiles of the fresh and passivated catalysts are shown in Figure 17. The reduction temperature of the passivated catalysts is much lower. This means that ex-situ reduction and passivation of the fresh catalyst enables in-situ activation at relatively low temperature (≈ 500 K).
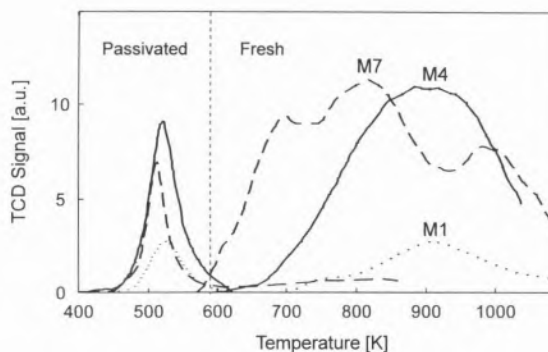
Figure 17 – TPR profiles of fresh and passivated catalysts.

3.3.2. Catalyst testing

The monolithic catalysts were tested in the hydrogenation of benzaldehyde to benzyl alcohol. Prior to the hydrogenation experiments the catalyst was reduced in-situ at a temperature of 473 K and a hydrogen pressure of 1.5 MPa.

For each catalyst a series of experiments was performed. About 145 g pure benzaldehyde was used as feed. The total pressure was 2.0 MPa and the temperature was 390, 415 or 440 K. The stirring rate was 1250 rpm.

Figure 18 gives typical results of an experiment. In the first part benzaldehyde is hydrogenated with very high selectivity, typically exceeding 99%. When almost all benzaldehyde has been converted, the rate of hydrogenolysis of benzyl alcohol to toluene and water becomes substantial. No evidence of other products such as hydroxymethylcyclohexane, benzene, and methane was found.

The straight line for the rate of benzaldehyde disappearance indicates a zero order reaction with respect to benzaldehyde under the reaction conditions applied. Both the reaction rate and the selectivity were determined from this zero-order part of the experiments. Table 7 gives the results for the experiments performed at 415 K. Besides a high selectivity the catalysts also show sufficient activity: ≈ 0.1 mmol/g$_{Ni}$s which amounts to 2 mol/m^{3}s. This value is situated within the useful conversion rate window for processes in the chemical industry, which ranges from about 1 to 10 mol/m^{3}s, according to Weisz [29]. The lower limit is determined by economic requirements, i.e. the desired conversion must be achieved within an acceptable reactor volume and residence time. The upper limit is imposed by the achievable rate of mass and heat transfer.

Preliminary calculations show that transport of hydrogen to the catalyst surface is most probably the rate-limiting step, which is in agreement with the general observations for liquid-phase hydrogenation reactions [30].

Figure 18 – Composition change with time (415 K, 20 bar, M4)

Table 7. Results of the hydrogenation experiments at 415 K.

Monolith	r [mmol/g$_{Ni}$·s]	TOF [s^{-1}]	Selectivity [%]
M1	0.10	0.16	100
M4	0.08	0.13	99.1
M7	0.17	0.65	98.1

3.4. Conclusions regarding benzaldehyde hydrogenation

The deposition-precipitation method used to apply nickel on alumina washcoated monoliths, resulted in high nickel loadings, though with low dispersion. Ex-situ reduction and passivation of the fresh catalyst enables in-situ activation at a lower temperature. The catalysts displayed a high selectivity and sufficient activity for the hydrogenation of benzaldehyde to benzyl alcohol, showing that nickel monolithic catalysts have potential for this reaction.

4. Conclusions

Process-integrated catalysis is a fascinating area, also in fine chemicals production. It enables the rational selection and design of the active catalyst phase, catalyst shape, reactor, and process. Batch and semi-batch reactors are not always the optimum choice in fine chemistry, especially for highly exothermic reactions. Furthermore, catalysis is increasingly used in fine chemistry, which often calls for dedicated plants.

Process-integrated catalysis has been succesfully used in the development of a process for the selective hydrogenation of CCl_2F_2 to the ozone-friendly CH_2F_2, a very exothermic reaction. Mechanistic/kinetic studies on a small scale provided important process data, which could directly be incorporated in the process design. This example shows that such an approach can markedly speed up process development. For instance,

it is conceived at an early stage which reactants and products have to be recycled, and these recycle streams can then be incorporated in process simulations.

The use of a monolithic catalyst in the selective hydrogenation of benzaldehyde to benzyl alcohol has potential; a high selectivity and reaction rates within the industrially acceptable range are obtained.

Acknowledgement

References

1. R. Sheldon, "Precision Process Technology", M.P.C. Weijnen and A.A.H. Drinkenburg, eds., Kluwer, Dordrecht, 1993.

2. W. Brune, Nature **379** (1996) 486.

3. United Nations Environmental Programme, "Report of the Ad-Hoc Technical Advisory Committee on ODS Destruction Technologies", (May 1992).

4. J. Burdeniuc and R.H. Crabtree, *Science* **271** (1996) 340.

5. S. Karmaker and H.L. Greene, *J. Catal.* **151** (1995) 394.

6. S. Imamura, T. Shiomi, S. Ishida, K. Utani, and H. Jindai, *Ind. Eng. Chem. Res.* **29** (1990) 1758.

7. D. Miyatani, K. Shinoda, T. Nakamura, M. Ohta, and K. Yasuda, *Chem. Lett.* (1992) 795.

8. S. Okazaki and A. Kurosaki, *Chem. Lett.* (1989) 1901.

9. Programme for Alternative Fluorocarbon Toxicity Testing, "Report of PAFT-V: HFC-32", (september 1992).

10. E.J.A.X. van de Sandt, A. Wiersma, M. Makkee, H. van Bekkum, and J.A., Moulijn, accepted for publication in *Recl. Trav. Chim. Pays-Bas* (1996).

11. P.N. Rylander, "Catalytic Hydrogenation over Platinum Metals", Academic Press, New York, 1967, p. 238 and references cited therein.

12. R.L. Augustine, "Catalytic Hydrogenation", Marcel Dekker Inc., New York, 1965, p. 130 and references cited therein.

13. M. Soede, E.J.A.X. van de Sandt, J. Struijk, M. Makkee, and J.J.F. Scholten, " Precision Process Technology", M.P.C. Weijnen and A.A.H. Drinkenburg, eds., Kluwer, Dordrecht, 1993, p 219.

14. M. Soede, E.J.A.X. van de Sandt, M. Makkee, and J.J.F. Scholten, *Stud. Surf. Sci. Catal.*,**78** (1993) 345.

15. J.R. Lacher, A. Kianpour, F. Oeting, and J.D. Park, *Trans. Faraday. Soc.* **52** (1956) 1500.

16. A. Wiersma, E.J.A.X. van de Sandt, M.A. den Hollander, M. Makkee, H. van Bekkum, and J.A. Moulijn, to be published.

17. E.J.A.X. van de Sandt, A. Wiersma, M. Makkee, H. van Bekkum, and J.A. Moulijn, accepted for publication in *Catalysis Today*.

18. A. Wiersma, E.J.A.X. van de Sandt, M. Makkee, H. van Bekkum, and J.A. Moulijn, Dutch Patent Application, NL 94.01574 (1994).

19. E.J.A.X. van de Sandt, A. Wiersma, M. Makkee, H. van Bekkum, and J.A. Moulijn, *Stud. Surf. Sci. Catal.* **101** (1996) 369.

20. A. Cybulski and J.A. Moulijn, Catal. Rev.-Sci. Eng., **36(2)**, (1994) 179.

21. T. Berglin, W. Herrmann, EP 83850234.2 (1986).

22. E. Bengtsson, EP 90850044.0 (1990).

23. S. Irandoust, A. Cybulski, and J.A. Moulijn, in *The use of monolithic catalysts for three-phase reactions, Structured Catalysts and Reactors*; A. Cybulski and J.A. Moulijn, Eds.; M. Dekker; New York, to appear in 1996.

24. R.K. Edvinsson and A. Cybulski, *Catalysis Today*, **24** (1995) 173.

25. E. Grolman, R.K. Edvinsson, A. Stankiewicz and J.A. Moulijn, *Hydrodynamic Instabilities in Gas-Liquid Monolithic reactors*, to be presented at the 1996 International Mechanical Engineering Congress & Exposition, Atlanta, (1996).

26. *Kirk-Othmer Encyclopedia of Chemical Technology* **4**; J.I. Kroschwitz, M. Howe-Grant, Treacy, C.A. Eds.; Wiley; New York , 4th edition (1992) pp. 116-125.

27. F. Brühne, in *Ullman's Encyclopedia of Industrial Chemistry* **A4**; W. Gerhartz, Y.S. Yamamoto, F.T. Campell, Eds.; Verlag Chemie, Weinheim, 5th edition (1985); pp 1-8.

28. L.M. Knijff, R.H. Bolt, R. van Yperen, A.J. van Dillen and J.W. Geus, *Stud. in Surf. Sci. and Catal.*, **63**, 165 (1991).

29. P.B. Weisz., *Chem. Technol.* (1982) 424.

30. P.N. Rylander , in *Ullman's Encyclopedia of Industrial Chemistry*, **A13**; B. Elvers, S. Hawkins, M.Ravenscroft, G. Schulz, Eds.; Verlag Chemie, Weinheim, 5th edition, (1989); pp. 486-494.

Microporous titanosilicates and other novel zeolite-type solids

Titanossilicatos microporosos e outros sólidos zeolíticos novos

JOÃO ROCHA[1]*, VÍTOR FÉLIX[1] and MICHAEL W. ANDERSON[2]

[1] DEPARTAMENTO DE QUÍMICA, UNIVERSIDADE DE AVEIRO, 3800 AVEIRO, PORTUGAL.
[2] DEPARTMENT OF CHEMISTRY, UMIST, P.O. BOX 88, MANCHESTER M60 1QD, U.K.

Recent progress towards the synthesis and structural characterization of microporous titanosilicates and related materials is reviewed. Traditional zeolites and zeolitic materials such as porous aluminophosphates, silicoaluminophosphates and derivatives, contain four-coordinated (Si, Al, P) framework atoms. Presently, much research is aimed at preparing microporous materials, containing five and six-coordinated atoms, which may possess novel structures and display important physical and chemical properties. In this context, transition metal atoms are particularly interesting since the resultant solids may find applications as heterogeneous redox catalysts. Microporous titanosilicates contain six-coordinated Ti(IV) atoms and four-coordinated Si(IV) atoms and display novel three-dimensional structures. Ti and Si may be substituted in the framework of certain members of this family (*e.g.* ETS-10 and nenadkevichite) by Nb or V, and Al or Ga, respectively. Very recently, a microporous vanadosilicate containing stoichiometric amounts of six-coordinated vanadium and possessing the structure of titanosilicate ETS-10 was synthesized and characterized. This suggests that, in the near future, it may be possible to prepare microporous silicates containing other transition metal centres.

Neste artigo revê-se o progresso recentemente feito na síntese e caracterização estrutural de titanossilicatos microporosos e materiais relacionados. Os zeólitos e os materiais zeolíticos tradicionais, tais como os aluminofosfatos, silicoaluminofosfatos e materiais derivados, porosos, contêm átomos tetracoordenados (Si, Al, P) no esqueleto. Desenvolve-se, presentemente, muita investigação com o objectivo de preparar materiais microporosos que contenham átomos penta e hexacoordenados, e que possam ter novas estruturas e exibir novas propriedades físico-químicas. Neste contexto, os átomos de metais de transição assumem um interesse particular, uma vez que os sólidos resultantes poderão encontrar aplicações como catalisadores heterogéneos redox. Os titanossilicatos microporosos contêm Ti(IV) hexacoordenado e Si(IV) tetracoordenado, exibindo estruturas tridimensionais novas. O Ti e o Si podem ser substituídos no esqueleto de certos membros desta família (por exemplo, ETS-10 ou nenadkevichite) por, respectivamente, Nb ou V e Al ou Ga. Muito recentemente, foi possível sintetizar e caracterizar um vanadossilicato microporoso que contém quantidades estequiométricas de vanádio hexacoordenado e que possui a estrutura do titanossilicato ETS-10. Este facto sugere que talvez seja possível, num futuro próximo, preparar silicatos microporosos contendo outros metais de transição.

1. Zeolites

Zeolites are crystalline, hydrated aluminosilicates with open three-dimensional structures built of $[SiO_4]^{4-}$ and $[AlO_4]^{5-}$ tetrahedra linked to each other by sharing all the oxygens to form regular intracrystalline cavities and channels of molecular dimensions (Figure 1) [1-3]. Silicon-oxygen tetrahedra are electrically neutral when connected together in a three-dimensional network as in quartz, SiO_2. The substitution of Si(IV) by Al(III) in such a structure creates an electrical imbalance and, to preserve overall electrical neutrality, each $\{AlO_4\}$ tetrahedron needs a balancing positive charge. This is provided by exchangeable cations held electrostatically within the zeolite. The structural formula of a zeolite is best expressed for the crystallographic unit cell as

$$M_{x/n} \left[(AlO_2)_x (SiO_2)_y \right] \cdot wH_2O$$
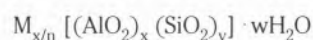
where, "M" is a non-framework exchangeable cation of valence n; the bracketed term represents the framework composition; and "w" is the number of (non-framework) water molecules.
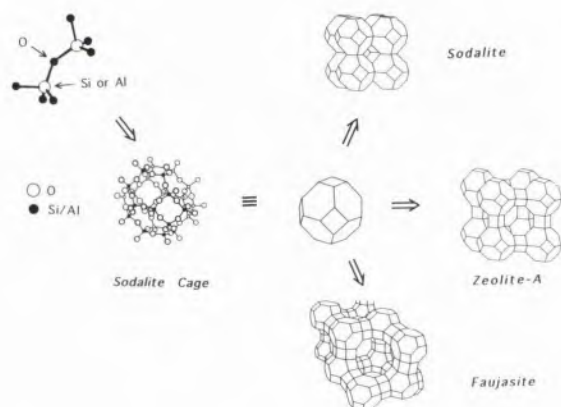
Figure 1. The structures of many zeolites, such as sodalite, zeolite-A and faujasite (zeolites-X and -Y), are based on the sodalite unit (or β-cage) which consists of 24 silica or alumina tetrahedra linked together: rings containing 4 and 6 Si/Al atoms are linked together to form a truncated octahedron.

Zeolites possess remarkable physical and chemical properties. The most important chemical properties are selective sorption, ion exchange and catalytical activity. The sorption and diffusion properties are related with the presence of channels of different sizes and cavities. The sorptive properties of zeolites are modified by the charge-balancing cations which are coordinated to the framework oxygen atoms. These cations can be ion-exchanged when the zeolite is treated with solutions of salts and typically they are mono or divalent ions such as Li^+, Na^+, K^+, Ca^{2+} and Mg^{2+}. The most important use of zeolites is as heterogenous catalysts. Zeolites are different from many other heterogenous catalysts in that catalytically active sites are distributed uniformly throughout their bulk. There are two kinds of acidic sites. Brønsted acid sites are the protons attached to bridging oxygens bonded to aluminium and silicon atoms. Lewis acid sites are produced upon calcination at elevated temperatures or steaming and their origin and nature is still poorly understood.

2. Microporous Aluminophosphates and Related Materials

Through the 1980s a variety of novel microporous framework structures were synthesized based on an aluminophosphate system [4]. In their pure form the aluminophosphates are termed $AlPO_4$s and consist of alternating corner-sharing framework $[AlO_4]^{5-}$ and $[PO_4]^{3-}$ tetrahedral groups. Overall the frameworks have no net charge and consequently no cation-exchange properties and little catalytic potential. Framework substitutions are, however, possible to produce silicoaluminophosphates [5] ($SAPO_4$s) and metal-substituted

aluminophosphates [6] ($MeAPO_4$s). The metals most commonly used are magnesium, manganese, iron, cobalt, zinc and vanadium. Some of these new materials have the framework topologies of known zeolites while others may have novel structures. Of great potential interest is a galophosphate known as cloverite (Figure 2), which consists of large supercages accessed through cloverleaf-shaped twenty-membered ring windows (larger than any known zeolite or $AlPO_4$) [7]. In all these materials the framework metal atoms are ostensibly in tetrahedral coordination although under certain circumstances (for example, various hydration conditions) the coordination might change to five- or six-fold.
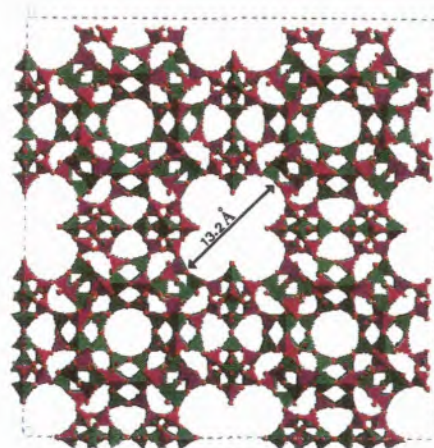
Figure 2. Projection of the structure of galophosphate cloverite along the [100] direction showing the cloverleaf-shaped 20-tetrahedral-atom pore opening. Green and purple tetrahedra contain Ga and P, respectively.

3. Novel Microporous Materials with Zeolite-Type Structures

There has been much recent effort, and some success, synthesizing microporous materials where framework atoms adopt different coordinations. Most notably microporous titanosilicates [8-10] (for example, ETS materials), molybdenum phosphates [11] (MoPOs) and manganese oxides such as OMS-1 [12]. Both titanosilicates and MoPOs contain octahedral and tetrahedral framework atoms with all atoms incorporated in stoichiometric quantities - not as a dopant. The OMS materials contain only octahedral framework atoms. As with zeolites, nature provides the clue that such variety in coordination is indeed compatible with open framework structures. Cacoxenite is a naturally occurring octahedral/tetrahedral phosphate structure with one of the largest pores ever observed [13]. OMS-1 is based on the mineral todorokite with only octahedral framework metal atoms. Many layered materials, including the expandable smectite clays, contain both octahedral and

tetrahedral framework atoms. By extending this variety of framework coordination to framework materials offers the opportunity to synthesize a whole variety of materials with novel pore structures. Also the new chemistry of the framework metal atoms provides new opportunities for the catalytic chemist.

4. Microporous Titanosilicates and ETS Materials

Titanosilicates form an important class of framework materials, both naturally occurring minerals and synthetic structures. In most minerals titanium adopts octahedral coordination and silicon adopts tetrahedral coordination with dense phase structures being most prevalent. However, a few open framework microporous minerals are known, although deposits are very rare. One such mineral is zorite which is found in small quantities in Russia [14]. Zorite has a highly disordered framework with ostensibly a two-dimensional channel system (Figure 3). Two orthogonal sets of channels are defined by twelve-T/O atom and eight-T atom rings (T =
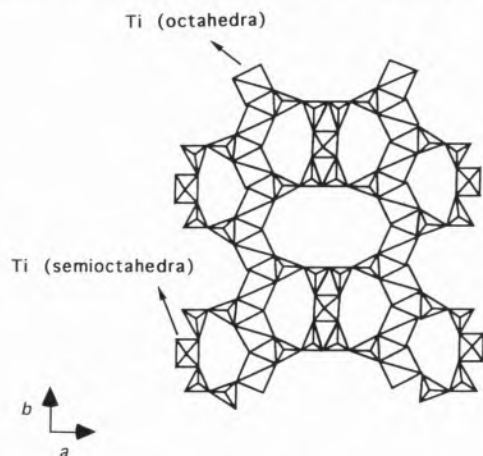
Figure 3. Zorite [001] projection. The disorder in the structure blocks the large twelve-ring pores and, since zorite possesses only eight-rings in ortoghonal directions, consequently zorite behaves as a small-pore material.

tetrahedral silicon; O = octahedral titanium). In reality the disorder in zorite results in the larger twelve-ring channels becoming partitioned into sections. A molecule diffusing into this twelve-T/O ring channel must make detours through the eight-T ring channel system in order to pass freely. Consequently, the adsorption characteristics of zorite are far inferior to that expected for an unfaulted material. Furthermore, zorite lacks thermal stability as internal water acts as part of the structure forming chains through the channel system. When the water is removed the framework structure collapses.

In 1989 and 1990 two independent reports by Kuznicki [8] and Chapman and Roe [10] discussed a synthetic structure which appeared to mimic zorite. Comparisons with the mineral were largely based upon similarities between the powder X-ray diffraction pattern of the synthetic material and that expected for zorite. However, no full structural analysis was performed. In the work of Kuznicki this synthetic material, which was referred to as ETS-4, was not very stable thermally and had poor adsorption characteristics. Another material (named ETS-10, see scanning electron microscopy, SEM, image in Figure 4) was also reported which displayed properties characteristic of a wide-pore and was thermally stable up to *ca.* 550ºC. In the case of ETS-10 there was no attempt at structural solution and no known natural counterpart was identified.

4.1. Synthesis of Microporous Titanosilicates and Related Materials

The synthesis of microporous titanosilicates is usually carried out in Teflon-lined autoclaves under hydrothermal conditions with temperatures ranging from 180 to 230 °C and times varying between a few hours and *ca.* 30 days. The syntheses are driven by kinetics with different metastable phases being formed with time. Several titanium and silicon sources can be used. $TiCl_3$ is often used but $TiCl_4$ and TiO_2 (both anatase and rutile) and a few organotitanium compounds are also important titanium sources. Sodium silicate solutions and colloidal silica are adequate silicon sources. The
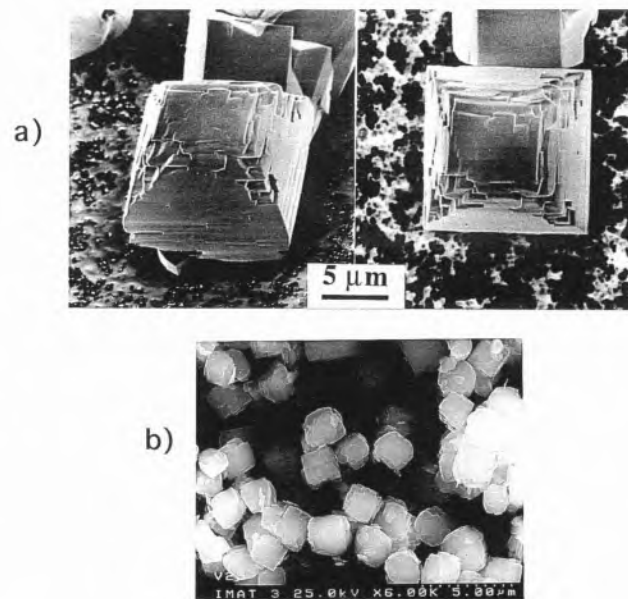
Figure 4. Scanning electron micrographs of (a) microporous titanosilicate ETS-10 and (b) vanadosilicate AM-6.

synthesis of ETS-10 usually requires the presence in the parent gel of both Na+ and K+ ions. Other phases (such as the AM materials) are produced pure only when one type of cation is present. Potassium fluoride is often used in the synthesis of ETS-10 but its presence is not crucial. So far, most porous titanosilicates can be prepared without the addition of any organic template molecules. However, several groups have prepared ETS-10 with a range of templates such as tetramethylammonium chloride, choline chloride and the bromide salt of hexaethyl diquat-5. The pH of the synthesis gel is usually high about 10-12 (after a 1:100 dilution with water). Seeding the gel with a little amount of the desired phase is also common practice. When trying to introduce aluminium and gallium in the framework of ETS-10, niobium in the framework of synthetic nenadkevichite or when preparing the vanadosilicate AM-6 other metals have to be introduced in the synthesis gel. A careful choice of the metal source is crucial for the success of the synthesis.

4.2. The Unusual Structure of ETS-10 [15-17]

It is difficult to determine the structure of ETS-10 (and indeed of most microporous titanosilicates) because (1) it can only be synthesized as a powder with particle size 0.6 - 20 μm, and (2) it exhibits a high degree of disorder - exemplified by broad powder X-ray diffraction (XRD) reflections (Figure 5). A similar situation exists for zeolite β, a wide-pore zeolite which was first synthesized in 1967 [18] but the structure of which was only determined in 1988 [19]. The strategy adopted for structural elucidation was (1) examine the framework ring connectivity and local disorder with high-resolution electron microscopy (HREM, see Figure 6), (2) determine the atomic make-up of the material by chemical analysis, (3) determine the local environment of silicon species by using ^{29}Si solid-state NMR (Figure 7), (4)

refine a trial structure using distance least squares analysis (DLS), (5) use this refined structure to simulate the HREM images (6) combine the minimised structure and the known disorder to simulate both the powder X-ray diffraction and electron diffraction data.

The solution of the structure of ETS-10 requires understanding in detail the nature of the disorder present. The ETS-10 framework can be decomposed into
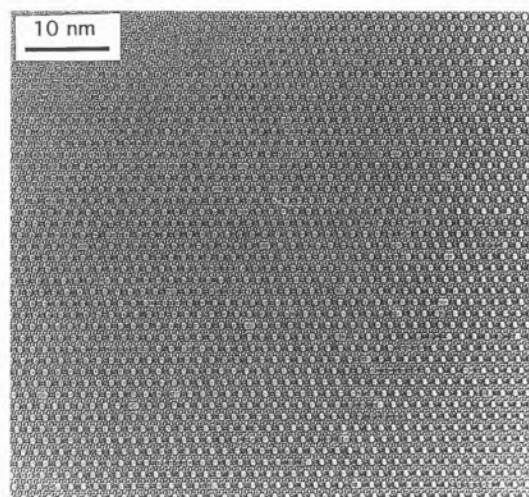
Figure 6. High-resolution electron micrograph of ETS-10 viewed along a direction perpendicular to the z-axis.

Figure 5. Powder X-ray diffraction patterns of microporous titanosilicate ETS-10 and vanadosilicate AM-6.
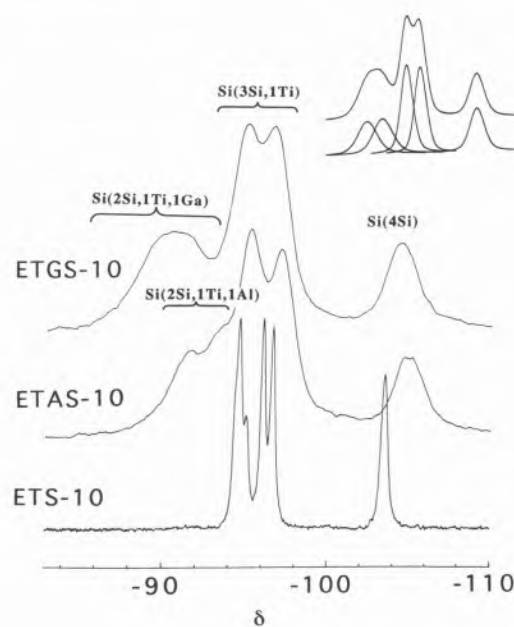
Figure 7. ^{29}Si magic-angle spinning NMR spectra of ETS-10, ETAS-10 and ETGS-10. The inset shows a deconvolution of the ETGS-10 spectrum.

38

sheets running parallel to the *a, b*-plane which contain two orthogonal sets of Ti-O-Ti chains with associated silicate units. The disorder is then manifested as a displacement of adjacent sheets in the *a, b*-plane. This displacement is always 1/4 unit cell in the *a*-direction and 1/4 unit cell in the *b*-direction (Figure 8 *B*). Knowing these rules for the disorder and assuming a random stacking of sheets the electron or X-ray diffraction patterns can be calculated using the DIFFaX routine.

All possible ordered and disordered polytypes of ETS-10 and the nature of the line defects can be explained in terms of different stacking sequences of the 8 possible sheets. Two specific interesting examples of ordered polytypes are as follows: *(1)* where the stacking sequence is 1, 3, 6, 8 repeat. This will give a diagonal arrangement of the twelve-ring pores - termed polymorph B; *(2)* where the stacking sequence is 1, 3, 1, 3 ... and so on. This will result in the twelve-ring pores having a zig-zag arrangement - termed polymorph A. Polymorph B belongs to space group *C*2/c with unit cell parameters *a* = 21.00 Å, *b* = 21.00 Å, *c* = 14.51 Å, α = 90.0°, β = 111.12° and γ = 90.0°. Polymorph A has either $P4_1$ or $P4_3$ symmetry with *a* = 14.58 Å, *b* = 14.85 Å and *c* = 27.08 Å, α = 90°; β = 90°; γ = 90°. Consequently, polymorph A has a screw axis and therefore will display chiral symmetry. In fact there is a spiral channel along the *c*-direction with a pitch of 27.08Å. This is one of the most interesting features of the structure of ETS-10. Only one other zeolite-type material has a chiral polymorph, zeolite β. However, ETS-10 contains four (Si) and six-fold atoms (Ti) while zeolite β has only atoms (Si, Al) in four-fold coordination. The chiral nature of ETS-10 polymorph A opens the exciting possibility of preparing a chiral heterogeneous catalyst. Our experience has, however, shown that this is not a trivial task.
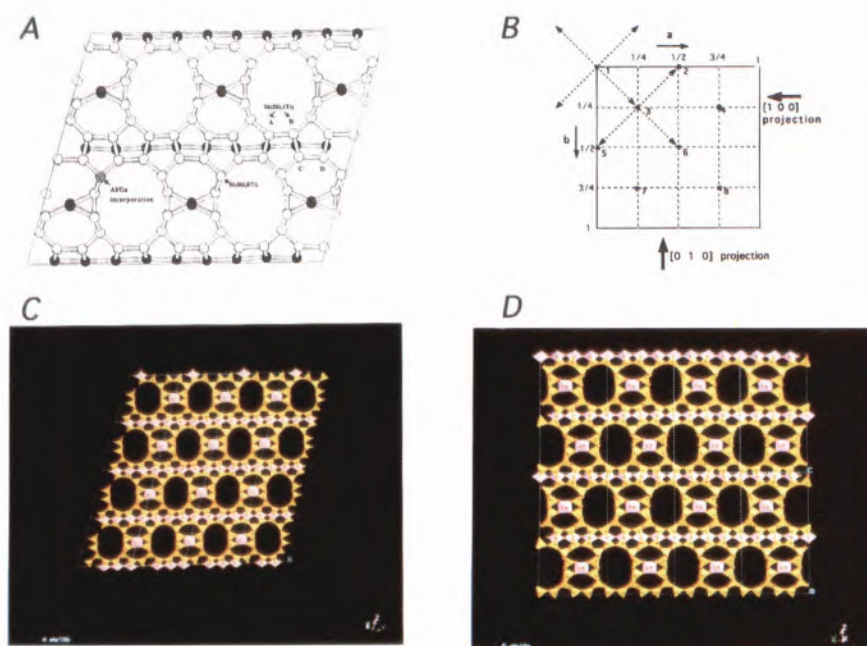
Figure 8. The stoichiometry of the framework of ETS-10 (*A*) is $Si_5TiO_{13}^{2-}$ which agrees with the chemical analysis, and the connectivity is exactly that suggested by ^{29}Si MAS NMR. The structure of ETS-10 is buit up from sheets displaced according to the diagram (*B*). The dots represent the eight possible sheet displacements as a fraction of the unit cell. Two sheets, however can only be connected if they are adjacent in this diagram; for example, 1 → 3 is allowed but 1 → 2 is not allowed. The basic building block for the disordered structure is most conveniently taken as a $Si_{40}Ti_8O_{104}^{16-}$ unit. The framework charge will be balanced by either sodium or potassium cations. The titanium atoms are octahedrally coordinated and are linked to one another in a straight chain. These chains are aligned parallel to the main orthogonal channels alternating in direction as they are stacked along the *c*-axis. The titanium octahedra are surrounded by 4 Si tetrahedra [each Si(3Si, 1Ti)] connected in such a way as to produce two three-rings. Four distinct types of Si(3Si, 1Ti) are labelled A, B, C and D in the *A* diagram, of which three can be resolved by NMR. These Si atoms are themselves connected together in purely siliceous five-rings where the apical Si of each five-ring is the remaining Si(4Si, 0Ti). Rods consisting of a chain of titanium octahedra surrounded on both sides by silicon 5-rings are joined together in a perpendicular arrangement to generate seven-rings and the complete stacking of these rods encompasses the large twelve-rings. The projection down the [110] zone axes is shown (*C*) for polymorph B (space group *C*2/c), and the projection down the [100] zone axis is shown (*D*) for polymorph A (space group $P4_1$). Down the c zone axis, owing to the stacking disorder of the plane parallel to the *c*-axis, there are no simple pores but a tortuous access may be gained by way of twelve-rings. Purple octahedra and brown tetrahedra contain Ti and Si, respectively.

4.3. Isomorphous Substitution in ETS-10 [20-22]

The anhydrous formula of ETS-10 is $M^{m+}_{2/m} TiSi_5O_{13}$, where M is a cation with charge m (Na$^+$ and K$^+$ in the as-prepared material). The cation density in ETS-10 is, therefore, approximately equivalent to that in a zeolite with Si/Al = 2.5 such as zeolite Y. This makes ETS-10 potentially a very interesting material for both cation exchange and catalysis. With regards to the latter the high framework charge and cation exchange ability should impart basic properties. On the other hand, acidic properties could be introduced by forming bridging hydroxyl groups such as Ti-(OH)-Si. To improve the acid characteristics further, we have incorporated aluminium and gallium into tetrahedral silicon sites, thus generating sites for zeolite-type acidity. These materials are known as ETAS-10 and ETGS-10, respectively. Consider again Figure 7. For the following arguments the choice of ETS-10 polymorph is irrelevant as the local T-site environment remains unaffected. In ETS-10 there are two types of silicon chemical environments, Si(3Si, 1Ti) and Si(4Si, 0Ti), which give the two groups of NMR resonances at -94 to -97 and ca. -103.7 ppm, respectively. The ratio of these environments is 4:1. The spectrum reveals a further crystallographic splitting of the Si(3Si, 1Ti) site. The spectrum of ETAS-10 contains all the ETS-10 resonances plus two other peaks ca. 4 ppm downfield from the Si(3Si, 1Ti) signals which become stronger when the framework aluminium concentration increases (Figure 9). These are ascribed to the framework incorporation of aluminium to produce Si(2Si, 1Al, 1Ti) environments (see Figure 8 A). It is important to note that there is no signal ca. 4 ppm downfield from the Si(4Si, 0Ti) resonance, showing no aluminium substitution neighbouring this silicon site and, hence, providing a direct proof of Al, Ti avoidance:
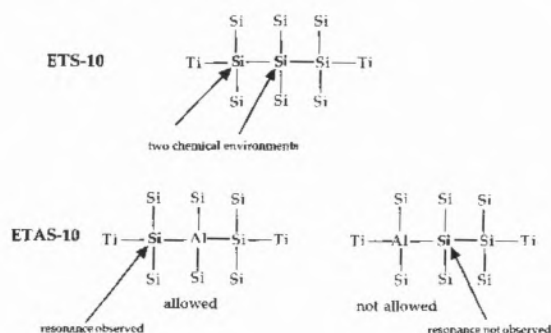
The ^{27}Al MAS NMR (Figure 10) spectrum is also indicative of this effect since it contains a single resonance at ca. 60 ppm assigned to Al(4Si). A small contribution from six-coordinated aluminium (ca. 2%) is evidenced by resonances between 0 and -10 ppm. The ^{29}Si MAS NMR spectrum of gallium-substituted ETS-10 resembles the spectrum of ETAS-10: a broad peak is seen downfield from the Si(3Si, 1Ti) signals. This peak
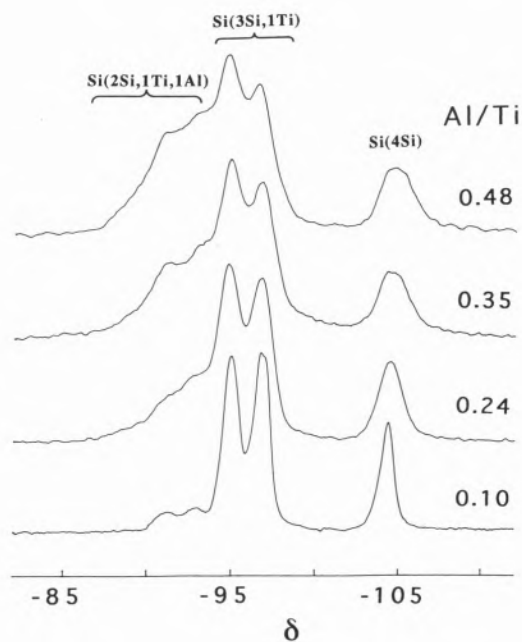
Figure 9. ^{29}Si magic-angle spinning NMR spectra of ETAS-10 with varying Al/Ti ratios as indicated. The linewidth of the peak at ca. -104 ppm varies linearly with the Al/Ti ratio.
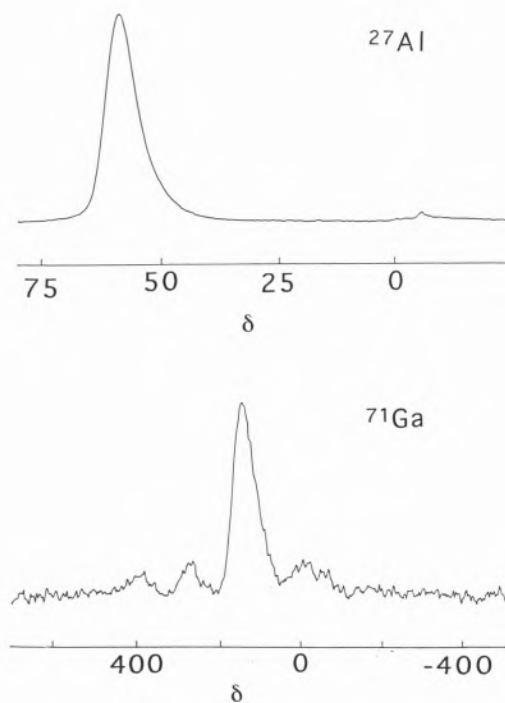
Figure 10. ^{27}Al and ^{71}Ga magic-angle spinning NMR spectra of ETAS-10 (Al/Ti = 0.24) and ETGS-10 (Ga/Ti = 0.37), respectively.

can be deconvoluted into two component signals, each one *ca.* 1.5 ppm downfield from the Si(2Si, 1Al, 1Ti) resonances, and which we assign to Si(2Si, 1Ga, 1Ti) as similar downfield shifts of the [29]Si resonances have been reported for gallium-substituted zeolites. No signals are observed in the range -99 to -103 ppm of ETGS-10. Detailed analysis of spectral intensities (I_{Si}) allow framework Si/Al (or Si/Ga) and Si/Ti ratios to be calculated from equations (1) and (2).

$$Si/Al = \frac{\sum_{n=0}^{4-m} \sum_{m=0}^{4-n} I_{Si(nAl,mTi)}}{0.25 \sum_{n=0}^{4-m} \sum_{m=0}^{4-n} n I_{Si(nAl,mTi)}} \qquad (1)$$

$$Si/Ti = \frac{\sum_{n=0}^{4-m} \sum_{m=0}^{4-n} I_{Si(nAl,mTi)}}{0.25 \sum_{n=0}^{4-m} \sum_{m=0}^{4-n} m I_{Si(nAl,mTi)}} \qquad (2)$$

On the other hand, the [71]Ga MAS NMR spectrum of fully-hydrated ETGS-10 (see Figure 10) displays a broad peak at *ca.* 160 ppm which is characteristic of four-coordinated gallium. It is too early to say whether Al (Ga), Ti avoidance is a general phenomenon is titanoalumino (gallo)silicates. However, it seems logical that, when possible, Al (Ga) and Ti will not be neighbours. We have found that at relatively high Al and Ga framework concentrations slight deviations from the Al (Ga), Ti avoidance rule are observed.

So far we have only discussed the isomorphous framework substitution of Si. Recently, in Aveiro, we have been able to replace Ti by Nb(V), V(IV) and (perhaps) Cr(III).

4.4. Titanium-Niobium-Silicates With the Structure of Nenadkevichite [23,24]

Nenadkevichite is a very rare microporous titanium-niobium-silicate mineral. Nenadkevichite from Lovozero (Russia), first described by Kouzmenko and Kazakova, has the composition (Na, Ca)(Nb, Ti)Si$_2$O$_7 \cdot 2H_2O$ [25]. Nenadkevichite from Saint-Hilaire, Quebec (Canada) crystallizes in space group *Pbam*: *a* = 7.41 Å, *b* = 14.20 Å and *c* = 7.15 Å. Its structure consists of square rings of silica tetrahedra Si$_4$O$_{12}$ in the (100) plane joined together by chains of NbO$_6$ octahedra in the [100] direction (Figure 11) [26]. The pores accommodate Na in two partially (0.53 and 0.54) occupied sites and H$_2$O in two fully occupied sites. Other minerals with a similar structure contain progressively more Ti^{4+} proxying for Nb^{5+} to the mineral labuntsovite which is essentially (Na, K, Ba)$_2$Ti$_2$(O, OH)$_2$Si$_4$O$_{12} \cdot 3H_2O$ [26,27].

We have prepared synthetic analogues of
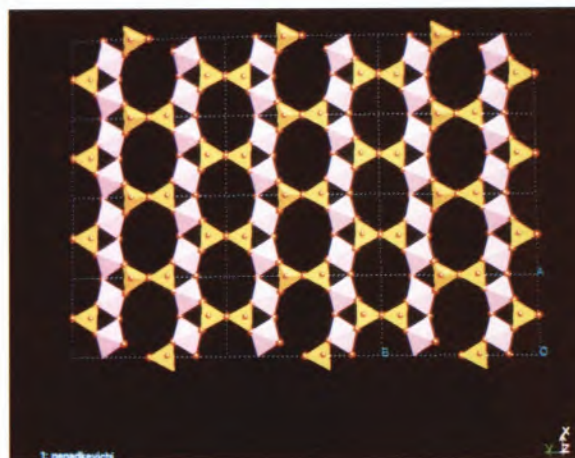
Figure 11. Nenadkevichite [001] projection. Purple octahedra and brown tetrahedra contain Ti (or Nb) and Si, respectively.

nenadkevichite with Ti/Nb molar ratios of 0.8, 2.0, 4.1, 12.3 and 17.1. We have also synthesized a purely titanous sample. These materials display powder XRD patterns (Figure 12) which are characteristic of nenadkevichite (see JCPDS cards 8-105, 37-484 and 25-1189) [26,27]. For Ti/Nb > 4.0 a splitting of the lines at 12.7° 2θ and 27 - 29° 2θ is observed. Interestingly, the XRD pattern of the sample containing no niobium is characteristic of nenadkevichite rather than labuntsovite. The ^{29}Si solid-state MAS NMR spectra (not shown) of nenadkevichite materials contain a main peak at *ca.* -90.8 ppm confirming the presence of Si(2Si, 2Ti) environments. With increasing titanium content a second fainter peak grows at about -96 ppm. At present, the assignment of this resonance is not clear, although we have observed that it becomes much stronger upon Na$^+$-ion exchange. The [93]Nb MAS NMR spectra (Figure 13) display a single
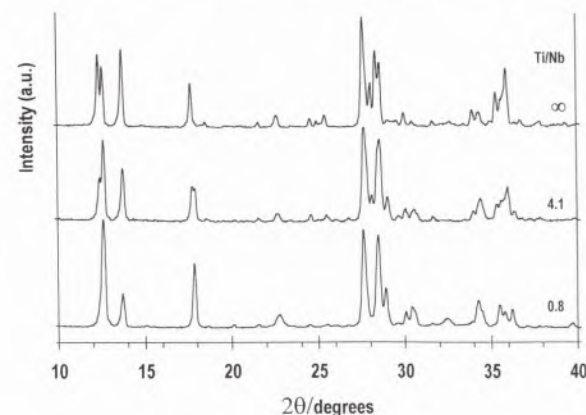
Figure 12. Powder X-ray diffraction patterns of synthetic nenadkevichite materials. The Ti/Nb molar ratios are indicated.
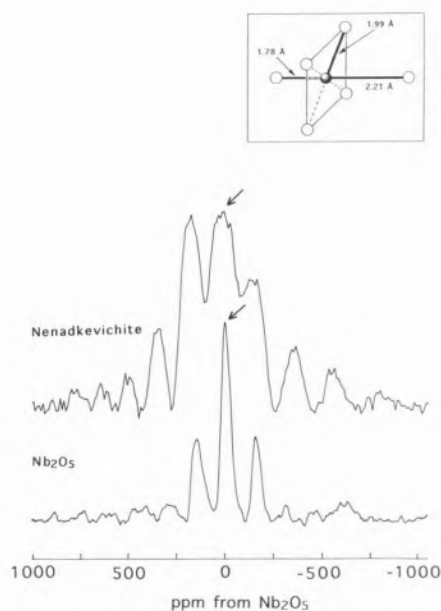
Figure 13. Typical ⁹³Nb magic-angle spinning NMR spectrum of synthetic nenadkevichite (Ti/Nb = 2.0). For comparison, the spectrum of Nb_2O_5 is also depicted. The arrows indicate the central line (the other peaks are spinning sidebands). The inset shows the local environment of Ti and Nb in the mineral nenadkevichite.

resonance at *ca.* 0 ppm from Nb_2O_5 consistent with the presence of hexacoordinated niobium. The sideband MAS pattern associated with this resonance indicates that the local niobium environment in nenadkevichite is more distorted than in Nb_2O_5. The diffuse-reflectance ultraviolet spectra of nenadkevichite materials and ETS-10 (not shown) are similar, hence confirming that titanium is in an octahedral environment. Raman spectra provide perhaps the best evidence for the isomorphous substitution of Ti^{4+} for Nb^{5+} in the framework of synthetic nenadkevichite. The Raman spectra of Ti/Nb = 0.8 nenadkevichite (Figure 14) displays two main bands at 668 and 226 cm⁻¹ which we attribute to NbO_6 octahedra. With increasing Ti content the Raman intensity of these bands decreases (particularly of the former) while simultaneously two other strong bands grow at *ca.* 764 and 290 cm⁻¹. We assign these bands to TiO_6 octahedra. The bands at 940, 878 and 520 cm⁻¹ also increase its intensity. Niobium-silicate glasses and several crystalline solids give bands at 600 - 800 cm⁻¹, which have been assigned to NbO_6 octahedra with *no* non-bridging oxygens (see ref. 28 and ref. therein). Bands seen at 230 - 280 cm⁻¹ are also probably associated with NbO_6 octahedra [28]. On the other hand, titanosilicate glass bands at 770 - 780 cm⁻¹ have been assigned to the Si-O-Ti vibration of Ti in octahedral coordination, while bands at 710 cm⁻¹ may be due to the Ti-O-Ti vibration in octahedral coordination [29]. Bands in this spectral range may, in addition, contain a contribution from SiO_4 deformati-

ons. Bands at 274 - 310 cm⁻¹ have been assigned to O-Ti-O rocking [29]. ETS-10 and ETS-4 contain octahedral Ti^{4+} and give strong bands at 730 and 775 cm⁻¹ and several bands centred at *ca.* 310 and 240 cm⁻¹, respectively. In conclusion, Raman spectroscopy clearly shows that octahedral Nb^{5+} is substituted by octahedral Ti^{4+} in the framework of synthetic nenadkevichite.
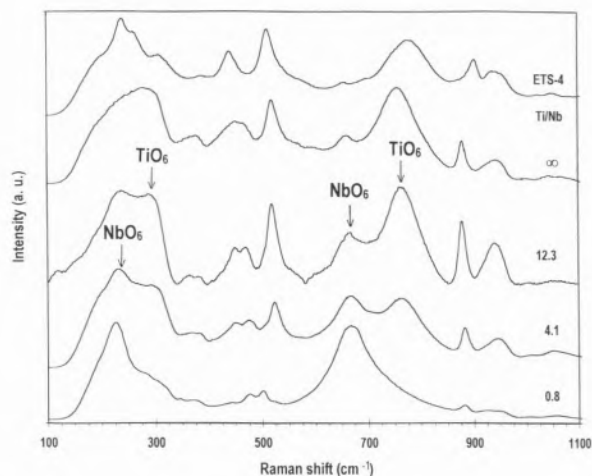
Figure 14. Selected Raman spectra of synthetic nenadkevichite materials. The Ti/Nb molar ratios are indicated. For comparison, the spectrum of ETS-4 is also depicted.

4.5. Synthetic Analogue of Penkvilksite and Other Titanosilicates [30]

As a result of a systematic study aimed at finding new microporous titanosilicates we have prepared four new materials, one of which (AM-3) possesses the structure of penkvilksite. We have named these solids AM-n (*Aveiro-Manchester*), n = 1 - 4. AM materials are often seen as low-level impurities contaminating ETS-10, ETS-4 and synthetic nenadkevichite. The crystal structures of the AM solids are still unknown but they behave much like microporous materials, particularly AM-3. Figures 15 and 16 show SEM images and XRD patterns, respectively, while Table 1 summarizes chemical analysis and adsorption data.

Table 1. Bulk chemical analysis and adsorption data on AM materials.

	AM-1	AM-2	AM-3	AM-4
Si/Ti	4.99	3.05	3.89	1.81
(Na, K)/Ti[(a)]	2.06	1.97	1.96	1.79
Maximum water uptake ($g_{water}/g_{adsorbant}$)%	11.5	8.2	11.7	7.0

(a) AM-1, -3, -4 contain only Na⁺, while AM-2 contains only K⁺.

AM-1 AM-2 AM-3 AM-4
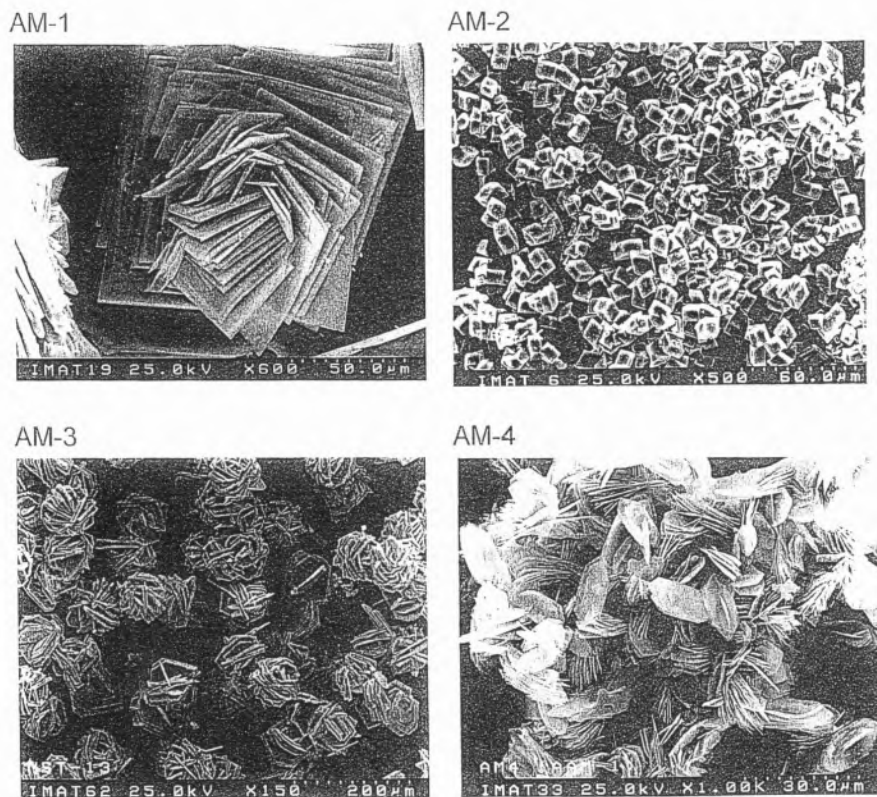
Figure 15. Scanning electron micrographs of AM-n materials.

Penkvilksite is a very rare sodium titanosilicate discovered in 1974 in the Yubileynaya pegmatoid vein of the Lovozero (Russia) alkalic pluton, with an ideal formula $Na_4Ti_2Si_8O_{22} \cdot 5H_2O$ [31]. Since no suitable single crystals are available for X-ray analysis the structure of penkvilksite is not known in detail. Bunssen *et al.* considered the mineral a "titanium zeolite" and suggested that it consists of a framework of pyroxene chains and columns of TiO_6 octahedra [31]. The water is known to be zeolitic.

4.6. The First Microporous Framework Vanadosilicate With Six-Fold Vanadium [32]

When trying to replace selectively some titanium by vanadium atoms in the framework of ETS-10, we have prepared a faint green vanadosilicate (containing *no* titanium) with the structure of ETS-10 which we have named AM-6. Vanadium has already been introduced in the framework of certain zeolites in small amounts. However, cavansite and pentagonite, dimorphs of the mineral $Ca(VO)(Si_4O_{10}) \cdot 4H_2O$ (Malheur County, Oregon), are the only microporous framework solids known to contain stoichiometric amounts of vanadium
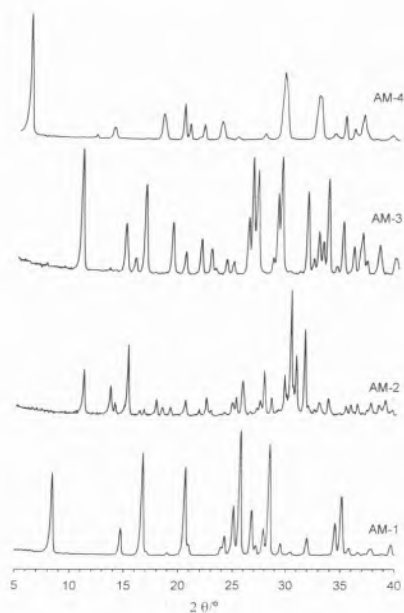
Figure 16. Powder X-ray diffraction patterns of AM-n materials.
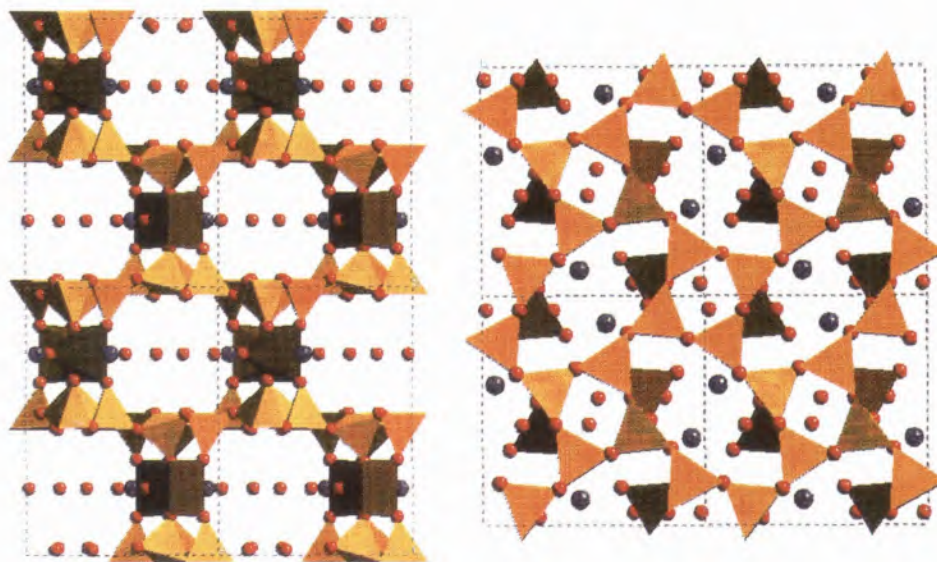
Figure 17. Canvasite structure: [001] (left) and [010] (right) projections. Light-brown tetrahedra and dark-brown square pyramids contain Si and V, respectively. Ca cations and water molecules are depicted in dark blue and red, respectively.

[33,34]. The framework of cavansite (Figure 17) is formed by silicate layers of four- and eight-membered rings of tetrahedra connected vertically by V^{4+} cations in a square pyramidal coordination. Replacement of the VO_5 group by two bridging oxygens would produce a tetrahedral framework topologically identical to that of zeolite gismondine. The Ca cations and the water molecules reside in the channels formed by the eight-membered rings and between the SiO_2 layers. Cavansite has channels running parallel to the c direction with a free diameter of only 3.3 Å in the hydrated state [33,34]. Hence, both canvasite and pentagonite are likely to behave (at best) as small-pore materials.

Nitrogen adsorption isotherms on ETS-10 and AM-6 (not shown) are both rectilinear, characteristic of microporous materials, with maximum uptakes of $ca.$ 0.12 and 0.15 $g_{nitrogen}/g_{adsorbant}$, respectively. Thermogravimetric analysis gives for AM6 a weight loss (water) from 50 to 400 °C of $ca.$ 11%, similar to that measured for ETS-10. Our best AM-6 sample seems to be a pure phase. Scanning electron microscopy (Figure 4) shows that this material contains only a very small amount of quartz as impurity. The cuboid AM-6 crystals are similar to ETS-10 crystals, with a particle size of around 1 to 3 μm. Because AM-6 is much less stable than ETS-10 in the electron beam the HREM images (not shown) are of a somewhat lower quality than those obtained for ETS-10 (Figure 6). Despite this, HREM evidence clearly shows that AM-6 is indeed a wide-pore material with a structure closely related to that of ETS-10. Detailed analysis of the micrographs suggests that the stacking disorder is similar in both materials.

The powder XRD patterns of ETS-10 and AM-6 shown in Figure 5 further confirm that the two solids have very similar structures. The strongest AM-6 reflection appears at a d-spacing (3.599 Å) slightly lower than that of ETS-10 (3.614 Å) but this is not altogether unexpected since V^{4+} and V^{5+} are slightly smaller than Ti^{4+}.

The Raman spectra of ETS-10 and AM-6 are shown in Figure 18. The former displays a strong band at 730 cm^{-1} associated with the TiO_6 octahedra while AM-6 gives a strong and sharp signal at 870 cm^{-1}. Octahedrally coordinated vanadate species are usually not symmetric and in general their Raman bands can not be used to fingerprint their structures. For an ideal VO_6 octahedron the highest frequency stretching bands are estimated to occur as low as 607 cm^{-1} [35]. However, in practice the bands appear at much higher frequency. For example, one of the most regular VO_6 octahedral structures known is contained within the decavanadate ion in $Na_6V_{10}O_{28}.18H_2O$; the highest stretching frequency from this structure appears at 830 cm^{-1} [35]. We assign the AM-6 band at 870 cm^{-1} to relatively undistorted VO_6 octahedra. Since the Raman spectra do not display the characteristic bands at 994, 701, 526 and 481 cm^{-1} our AM-6 samples do not seem to contain any V_2O_5. The structure of AM-6 may only contain (short) terminal V = O bonds in defect sites or on the surphace of crystallites. In accord, the main AM-6 band is seen at 870 cm^{-1} whereas the Raman bands associated with V = O bonds usually appear at 900 - 1000 cm^{-1} [35]. Close inspection of the spectrum of AM-6 reveals the presence of a faint band (not seen for ETS-10) at 946 cm^{-1} which is perhaps due to a relatively small number of V = O bonds in the environ-

ments mentioned above. In the spectral range 100 to 700 cm^{-1} most AM-6 bands are also exhibited by ETS-10. However, the bands of the former are much weaker and seem to appear at slightly different frequencies. The band at 461 cm^{-1} is not seen in the spectrum of ETS-10.

The room-temperature electron paramagnetic resonance spectrum of AM-6 (not shown) displays a single and relatively broad resonance (peak-to-peak width *ca.* 53 G) centred at g = 1.9545, lacking hyperfine structure, indicating the presence of (non-isolated) V^{4+} in dipolar interaction with other V^{4+} ions. Although we were unable to observe any ^{51}V MAS solid-state NMR signals from the samples prepared so far, the framework of AM-6 probably also contains V^{5+}. Indeed, the presence of paramagnetic V^{4+} may render the V^{5+} signal too broad to be detected. On the other hand, preliminary experiments show that upon calcination in oxygen (or air) at 400 °C AM-6 turns from faint green to white and gives a broad ^{51}V MAS NMR signal at -566 ppm (relative to VOCl$_3$). However, powder XRD (not shown) suggests that the AM-6 structure has partially collapsed. At 450 °C the sample is completely amorphous. Hence, we can not draw any conclusions about the coordination of vanadium in AM-6 based on the NMR results.

5. Conclusions and Overview of Future Research and Applications

Unlike traditional zeolites, microporous framework titanosilicates contain atoms in four- and 6-fold coordination. These materials possess completely (and sometimes entirely unexpected) novel structures which, combined with the presence of redox centres in the framework, afford them great potential to be used in a range of important areas such as heterogenous catalysis,
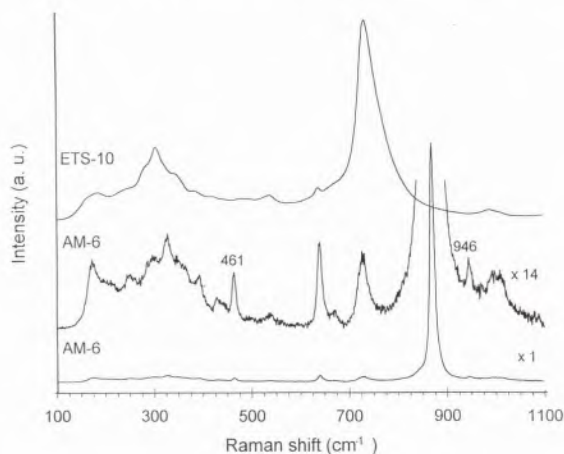
Figure 18. Raman spectra of microporous titanosilicate ETS-10 and vanadosilicate AM-6.
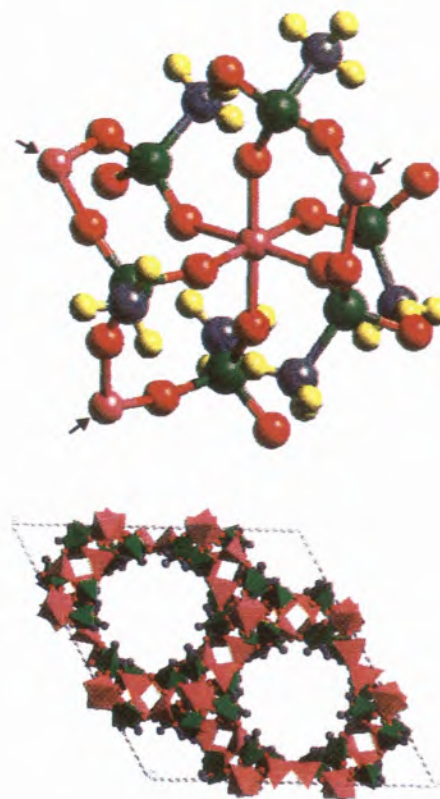
Figure 19. The skeleton of aluminium methylphosphonate AlMepO-β (bottom) is built up of fused four-ring chains and forms unidimensional 18-ring channels of *ca.* 5.8Å cross-section fringed with methyl groups (small dark blue spheres). The asymmetric unit of AlMepO-β (top) contains six crystallographically independent CH$_3$PO$_3$ tetrahedra which share oxygen atoms at their corners with three adjacent Al atoms. Among the four independent Al atoms, three (depicted by arrows) are tetra-coordinated and the fourth is hexa-coordinated, all of which are bound by phosphonates. Pink spheres denote Al, green P, red O, grey C and yellow spheres denote H atoms. P-containing tetrahedra and Al-containing polyhedra are depicted in green and pink, respectively.

ion-exchange and adsorption processes. ETS-10 has already found application in the manufacture of chlorofluorocarbon (CFC)-free air conditioners based on evaporative and desiccant cooling (see ref. 36 and references therein). In addition, since it has a high affinity for Pb^{2+} (via ion-exchange), it may find applications in water treatments. ETS-10 and ETAS-10 have low acidity and we have found that they are very good heterogenous catalyst for certain processes [37]. ETS-10 is a very active and selective catalyst for the double-bond isomerization of 1- to 2-butene [38]. ETS-10 has also been shown to be a good ruthenium catalyst support for Fischer-Tropsch synthesis [39]. ETS-10 and nenadkevichite possess local asymmetric Ti(IV) and Nb(IV) environments (see inset in Figure 13) [17,24] which have been found in materials which display non-linear optical activity such as KTiO(PO$_4$) [40,41]. Therefore, it is

possible that they may also be optically active and, if so, they would combine this property with microporosity. Since, via framework substitution, one can prepare materials with a wide range of (for example) Nb/Ti ratios it may be possible to "tune" the optical properties. We have found that the vanadosilicate AM-6 is antiferromagnetic at low temperatures, due the strong coupling between V(IV) spins. However, it may be possible, via dilution of V(IV) (d^1) centres with V(V) or Ti(IV) (d^0), to obtain a ferromagnetic or ferrimagnetic material.

In our laboratories we are currently trying to prepare new microporous titanosilicates and related materials. We believe (and already have good preliminary evidence) that it is possible to prepare vanadosilicates, zirconosilicates and perhaps niobosilicates. On the other hand, other groups are making considerable progress in the field of microporous transition-metal phosphates. Recently, an exciting and unexpected material (Figure 19) has been reported by Maeda et al: the first microporous inorganic-organic composite, aluminium methylphosphonate (AlMepO-β) [42,43]. The asymmetric unit of AlMepO-β contains six crystallographically independent CH_3PO_3 tetrahedra which share oxygen atoms at their corners with three adjacent Al atoms (which are in four- and six-fold coordination). It is clear that presently the science of microporous framework materials is alive and is not restricted to fourfold aluminium and silicon. The challenge for the future is to prepare microporous solids using most of the elements in the periodic table.

Acknowledgments

References

1. D. W. Breck, *Zeolite Molecular Sieves*, John Wiley, New York, 1974.
2. R. M. Barrer, *Hydrothermal Chemistry of Zeolites*, Academic Press, New York, 1982.
3. R. Rosemary, *Molecular Sieves*, Van Nostrand Reinhold, New York, 1989.
4. S. T. Wilson, S. Oak, B. M. Lok, E. M. Flanigen, W. Plains, U.S. Pat. **4,310,440** (1982).
5. B. M. Lok, C. A. Messina, R. T. Gajek, T. R. Cannan, E. M. Flanigen, U.S. Pat. **4,440,871** (1984).
6. S. T. Wilson, S. Oak, E. M. Flanigen, U. S. Pat. **4,567,029** (1986).
7. M. Estermann, L. B. McCusker, C. Baerlocher, A. Merrouche, H. Kessler, *Nature* **352** (1991) 320.
8. S. M. Kuznicki, U.S. Pat. **4,853,202** (1989).
9. S. M. Kuznicki, K. A. Thrush, Eur. Pat. **0405978A1** (1990).
10. D. M. Chapman, A. L. Roe, *Zeolites* **10** (1990) 730.
11. R. C. Haushalter, L. A. Mundi, *Chem. Mater.* **4** (1992) 31.
12. Y. F. Shen, R. P. Zerger, R. N. DeGuzman, S. L. Suib, L. McCurdy, D. I. Potter, C. L. O'Young, *Science* **260** (1993) 511.
13. P. B. Moore, J. Shen, *Nature* **306** (1983) 356.
14. P. A. Sandomirskii, N. V. Belov, *Sov. Phys. Crystallogr.* **24** (1979) 686.
15. M. W. Anderson, O. Terasaki, T. Ohsuna, A. Philippou, S. P. MacKay, A. Ferreira, J. Rocha, S. Lidin, *Nature* **367** (1994) 347.
16. M. W. Anderson, O. Terasaki, O. Ohsuna, P. J. O'Malley, A. Philippou, S. P. MacKay, A. Ferreira, J. Rocha, S. Lidin, *Philos. Mag. B* **71**, (1995) 813.
17. G. Sankar, R. G. Bell, J. M. Thomas, M. W. Anderson, P. A. Wright, J. Rocha, *J. Phys. Chem.* **100** (1996) 449.
18. R. L. Wadlinger, G. T. Kerr, E. J. Rosinski, U.S. Pat. **3,308,069** (1967).
19. J. M. Newsam, M. J. Treacy, W. T. Koetsier, C. B. Gruyter, *Proc. R. Soc. Lond. A*, **420** (1988) 375.
20. M. W. Anderson, A. Philippou, Z. Lin, A. Ferreira, J. Rocha, *Angew. Chem., Int. Ed. Engl.* **34** (1995) 1003.
21. J. Rocha, Z. Lin, A. Ferreira, M. W. Anderson, *J. Chem. Soc., Chem. Commun.*, (1995) 867.
22. M. W. Anderson, J. Rocha, Z. Lin, A. Philippou, I. Orion, A. Ferreira, *Microporous Mater.* **6** (1996) 195.
23. J. Rocha, P. Brandão, Z. Lin, A. Kharlamov, M. W. Anderson, *Chem. Commun.* (1966) 669.
24. J. Rocha, P. Brandão, Z. Lin, A. Ferreira, M. W. Anderson, *J. Phys. Chem.* **100** (1996) 14978.
25. M. V. Kouzmenko, M. E. Kazakova, *Dokla. Akad. Nauk SSSR* **100** (1955) 1159.
26. P. G. Perrault, C. Boucher, J. Vicat, E. Cannillo, G. Rossi, *Acta Cryst.* **B29** (1973) 1432.
27. E. I. Semenov, *Trudy IMGRE Akad. Nauk SSSR* **2** (1959) 102.
28. K. Fukumi, S. Sakka, *J. Mater. Sci.* **23** (1988) 2819.
29. L. A. Farrow, E. M. Vogel, *J. Non-Cryst. Solids* **143** (1992) 59.
30. J. Rocha, A. Ferreira, Z. Lin, A. Philippou, M. W. Anderson, submitted.
31. I. V. Bunssen, Y. P. Men'shikov, A. N. Mer'kov, A. P. Nedorezova, Y. I. Uspenskaya, A. P. Khomyakov, *Dokl. Akad. Nauk. SSSR* **217** (1974) 126.
32. J. Rocha, P. Brandão, Z. Lin, M. W. Anderson, V. Alfredsson, O. Terasaki, *Angew. Chem.* in press.
33. H. T. Evans, JR., *Amer. Min.* **58** (1973) 412.
34. R. Rinaldi, J. J. Pluth, J. V. Smith, *Acta Cryst.* **B31** (1975) 1598.
35. F. D. Hardcastle, I. E. Wachs, *J. Phys. Chem.* **95** (1991) 5031.
36. X. Yang, R. E. Truitt, *J. Phys. Chem.* **100** (1996) 3713.
37. J. Rocha, Z. Lin, A. Ferreira, A. Philippou, M. W. Anderson, U.K. patent Application **9, 619, 336.**
38. R. R. Rajamohanan, P. R. Hedge, S. V. Chandwadkar, A. J. Ratnasamy, *J. Catal.* **155** (1995) 345.
39. C. R. Bianchi, C. L. Ragaini, *Catal. Lett.* **33** (1995) 49.
40. N. K. Hansen, J. Protas, G. Marnier, *Acta Crystallogr. B* **47** (1991) 660.
41. M. M. Eddy, T. E. Gier, N. L.Keder, G. D. Stucky, D. E. Cox, J. D. Bierlein, J. Jones, *Inorg. Chem.* **27** (1988) 1856.
42. K. Maeda, J. Akimoto, Y. Kiyozumi, *J. Chem. Soc., Chem. Commun.*, (1995) 1033.
43. J. Rocha, Z. Lin, C. Fernandez, J. P. Amoureux, *Chem. Commun.*, in press.

Porphyrins and the Photodynamic Therapy of Cancer

As Porfirinas e a Terapia Fotodinâmica do Cancro

MARIA DA GRAÇA HENRIQUES VICENTE

DEPARTAMENTO DE QUIMICA, UNIVERSIDADE DE AVEIRO, 3810 AVEIRO, PORTUGAL

The radiotherapy and the chemotherapy, normally used for the treatment of cancer, can induce dangerous side effects due to their indiscriminately destruction of both normal and tumor tissues. Photodynamic therapy (PDT) is a new technique for the treatment of various types of malignant tumors. PDT is based on the ability of some porthyrins and porphyrin-like chromorphores to be accumulated selectivity in tumor tissues; tumor necrosis can be obtained by irradiation of the neoplastic area with light of the appropriate wavelength. Until now a few thousand patients have been successfully teateo by PDT worldwide. This article reviews the synthesis, main characteristics and mechanism of action of the main porphyrin-like chromophores used in PDT.

A radioterapia e a quimioterapia, normalmente usadas para o tratamento do cancro, podem original efeitos secundários perigosos, devido à destruição indiscriminada que provocam nos tecidos normais e cancerígenos. A terapia potodinâmica (PDT) é uma técnica nova para o tratamento de vários tipos de tumores malignos. A PDT baseia-se na capacidade que algumas porfirinas e compostos afins têm para se acumularem selectivamente nos tecidos cancerígenos; a destruição dos tumores é obtida àtravés da irradiação da área neoplástica com luz de comprimento de onda apropriado. Até hoje, alguns milhares de doentes têm sido tratados com sucesso pela PDT, por todo o mundo. Neste artigo é feita uma revisão sobre a síntese, principais características e modo de acção dos principais compostos do tipo porfirínico usados em PDT.

Introduction

Photodynamic therapy is a form of photochemotherapy (PCT) that combines visible light, molecular oxygen and a porphyrin-based photosensitizing drug to achieve an efficient therapeutic effect. In this method of cancer treatment neither the light nor the drug has any independent biological effect. In PDT, dangerous side effects in normal tissues which are common in chemotherapy and radiotherapy, can be avoided since the photosensitizer selectively accumulates in the tumor tissues. New developments in lasers and fiber optics have made possible the treatment of different kinds of tumors, both internal and external.

It has been known for over seventy years that some porphyrins have a natural tendency to selectively localize in malignant tumors compared with normal tissue. Upon activation with red light, these porphyrins become very toxic to the surrounding environment; it is believed that they sensitize the production of singlet oxygen and other types of radicals that are very toxic to the tumor cells. Therefore, porphyrins have been successfully used as photosensitizers for PDT. The phototoxicity of the porphyrins and derivatives is mainly determined by their photophysical and photochemical properties and by their degree of tumor selectivity. The basic PDT treatment consists of injecting a patient with the porphyrin sensitizer and then waiting a certain time for the photosensitizer to localize in the tumor tissues. The porphyrin containing tumor cells fluoresce in ultraviolet light and this can be used for detection of neoplastic tissues. The activation of the photosensitizer, by irradiation of the tumor with light of the appropriate wavelength, leads to the generation of cytotoxic species and destruction of the tissues. Photofrin® is currently the photosensitizer used worldwide in PDT and it has been successfully used in over ten thousand patients since its first preparation in 1981. However, due to its complicated composition and weak absorption in the red light region, new improved substances have been investigated as potential photosensiti

zers for PDT. Second generation drugs have been proposed and some are already in Phase I/II clinical trials. In this article an historical view of PDT is first given, followed by discussion of the mechanism of action and structural features of the second generation of photosensitizers with potential use in PDT (for recent reviews see [1-6]).

Historical

In 1900, Raab [7] for the first time reported the use of acridine (**1**) on paramecium for the detection and treatment of tumor cells. Three years later, Jesionek and Tappeiner [8] demonstrated the use of eosin (**2**) in the treatment of human tumors. In 1908, Hausman [9] first noted the photodynamic properties of hematoporphyrin-IX (HP) (**3**) and described the treatment of cancer cells in rats. In the following twenty years, a large number of compounds were used to induce cancer in laboratory animals. In 1942, Auler and Banzer [10] and Figge [11] showed that HP (**3**) had a great affinity for malignant tissue. Some other porphyrins, e.g. protoporphyrin-IX (PP) (**4**), mesoporphyrin-IX (MP) (**5**), deuteroporphyrin-IX (DP) (**6**) and coproporphyrin (**10**), were classified as naturally occurring cocarcinogenic compounds. Other fluorescent compounds such as eosin, fluorescein, rhodamine, dihydrocollidine, methylene blue, thioflavin, toluidine blue and riboflavin were also used, but none exhibited such a strong affinity for the neoplastic tissues as did the porphyrins. In the 1950s, many other authors [12] demonstrated that porphyrins have a tendency to accumulate in both animal and human tumor tissues and that they could be used for the detection and delineation of neoplastic tissue. However, the early studies in humans required large dosage of HP (**3**), [12c] which increased the danger of photosensitivity of the patients, sometimes causing severe skin necrosis upon exposure to strong light.

In the early 1960s, Lipson et al. [13] introduced an improved technique using a hematoporphyrin deñvative (HPD) for the detection and treatment of malignant tumors in humans. They demonstrated that HPD had a greater tendency to accumulate in malignant tissue than did HP (**3**) and also that it had superior fluorescent properties. To prepare the HPD product, Lipson et al. [13c] dissolved HP (**3**) in a solution of 19:1 glacial acetic acid/concentrated sulfuric acid, filtered the resulting mixture and treated the porphyrin solution with 3% sodium acetate. The presumably acetylated products were collected by filtration and dissolved in saline solution containing sodium hydroxide. The final pH was adjusted to 7.4 with hydrochloric acid and the HPD product was stored at -30°C, in the dark. Since 1961 many investigators have used HPD in combination with light for selective *in vivo* tumor destruction.

Various investigators, using high performance liquid chromatography (HPLC) techniques, demonstrated that HPD is a complex mixture of compounds. The major components have been identified as HP (**3**), PP (**4**), hydroxyethylvinylporphyrin (HVD) (**7** and **8**), diacetoxyethyldeuteroporphyrin-IX (DAD) (**9**), and aggregates (dimers and higher oligomers) of porphyrins [14]. In 1981, Dougherty et al. [15] used gel exclusion chromatography to purify the HPD material. In this way they were able to remove most of the monomeric porphyrins and therefore obtain a purified high-molecular weight aggregate that accounted for essentially all of the photo-activated tumoricidal activity of HPD. In addition, the skin photosensitivity of animals receiving an equivalent tumoricidal dose (when activated by light) of this purified active component was greatly reduced compared to HPD. Thus, an improvement in therapeutic ratio was achieved using this purified material, known today as Photofrin®. This purified HPD material has been the subject of numerous studies in an attempt to unambiguously identify its active compounds. Dougherty et al. [16] first described the active compound of HPD as dihematoporphyrin ether (**11** and isomers). A few years later, Kessel [17] proposed dihematoporphyrin ester (**12** and isomers) as the active component of HPD. Some authors [18] have proposed a mixture of the two dimers (**11**) and (**12**) for the active component of HPD. Other studies have suggested that the active species in HPD is a mixture of dimers and higher oligomers linked by ether, ester and even carbon-carbon bonds [19]. More recently it was reported [20] that the ratio monomer:dimer:oligomer for HPD is 22:23:55 and for Photofrin® is 14:19:67.

The rights to Photofrin® belonged to Oncology Research and Development, Buffalo, from 1981 until 1985 whereupon an agreement for transfer of the patent was negotiated with Johnson & Johnson. In 1987 the rights to Photofrin® were sold to Quadra Logic Technologies (QLT), Vancouver. The QLT company together with American Cyanamid/Lederle Laboratories are currently obtaining world-wide marketing approval for Photofrin®. The first Phase III clinical trials using Photofrin® began only in 1988. In 1993 the Canadian Health Protection Branch announced the first approval for the use of Photofrin® in the treatment of superficial bladder cancer [2]. In 1994 approvals occurred in Holland and Japan, in 1995 in the US, and in 1996 in France.

The photodynamic effect

Porphyrin-induced photodynamic damage to cells results in modification of many cellular components and functions. For example, inhibition of transport across the cell membrane, inactivation of enzymes, impaired protein synthesis, vascular damage, effects on DNA, membrane swelling and complete membrane

lysis, and vessel constriction and degeneration have all been reported [21]. It has also been observed [22] that, while the cell plasma membrane may be altered due to HPD photodynamic damage, it may not be a primary event. Effects at the nuclear and mitochondrial membranes may be of primary importance to the ultimate demise of the cell. Interestingly, not all effective photosensitizers cause the same primary effects [23]. Ackerman et. al. [24] showed that singlet oxygen, a short-lived electronically excited state of molecular oxygen, is the effective cytotoxic agent in many photodynamic reactions. *In vivo* experiments have shown [25] that oxygen is required in order to have an effective photodynamic reaction. More evidence includes inhibition of cell killing when quenchers capable of trapping oxygen radicals are added [26], and enhanced killing in D_2O-containing systems [27].

Upon activation with red light, an electron of the porphyrin nucleus is excited from the ground-state to an excited singlet state (Figure 1). The electron then can either return to the singlet ground-state with the emission of light (heat, fluorescence), or it can change its spin via intersystem crossing (ISC) to give the triplet state, which has a slightly lower energy [28]. The decay of the triplet to the singlet ground-state is slow because according to the spectroscopic selection rules, the transition is forbidden. The metastable triplet porphyrin sensitizer therefore has time to react with its chemical environment, transferring energy to produce forms of oxygen known to be lethal to cells. There are two possible mechanisms for the transfer of the energy of the sensitizer [29]. In the designated Type II photooxygenation mechanism, the excitation energy is transferred to molecular oxygen in its ground-state (triplet) to produce highly reactive (toxic) singlet oxygen. In this process the photosensitizer acts catalytically since its function is to absorb light energy and to transfer it to molecular oxygen, regenerating ground state photosensitizer. Singlet oxygen is a powerful oxidant that reacts with a variety of biological molecules and assemblies [30].

In the so-called Type I mechanism the excited triplet state of the sensitizer may react, for example by abstracting a hydrogen atom from a substrate molecule, or undergo electron transfer. The latter may be followed by the formation of, for example, the superoxide ion and radical anion, and the hydroxyl and hydroperoxyl radicals. Some of the radicals produced by these reactions can subsequently react with oxygen to produce a wide variety of oxidized products such as peroxides. The first excited singlet state of the porphyrin can also participate in an electron transfer process with a biological substrate, resulting in the photobleaching of the photosensitizer and the destruction of the substrate [31]. Although some work has been done to identify the photoproducts of HPD photosensitizing reactions in model systems [32], *in vivo* products are not yet identified. Recently, the *in vivo* formation of a chlorin-type photoproduct from protoporphyrin-IX (**4**) was reported [33].
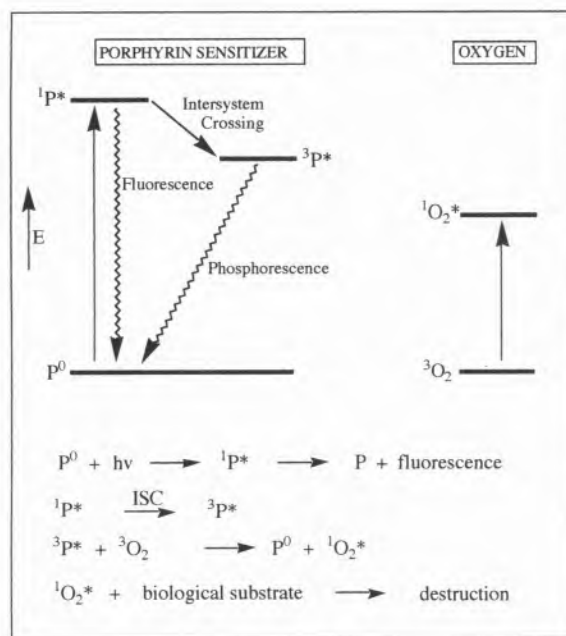
Figure 1 – Energy diagram (excluding vibrational levels) showing porphyrin and oxygen singlet and triplet states. P = porphyrin sensitizer, * = electronically excited state; 1 = singlet excited state, 3 = triplet excited state.

Most of the new photosensitizers for PDT have quantum yields for singlet oxygen production >0.5 which means that singlet oxygen can be produced in considerable amounts when the photosensitizer is activated by red light. The importance of the singlet oxygen mechanism gives rise to another problem for the photodynamic effects, which has to do with the concentration and consumption of molecular oxygen in the tumor cells; PDT induces vascular damage resulting in reduced microcirculation within a few minutes, which further reduces the oxygen supply to the tumor. Low vascular density tumors are more sensitive to oxygen consumption than highly vascularized tumors [34]. It has been reported that tumor oxygenation may be improved by breathing a perfluorochemical emulsion and carbogen (95% O_2, 5% CO_2) [30].

Most clinical studies use lasers as the source of red light, in order to take advantage of the high coupling efficiency to optical fibers which allows a beam of intense light to be delivered conveniently to many areas of the body. One of the more practical recent advances in PDT is the availability of diode lasers as light sources. The more compact diode lasers are much cheaper and have minimum power requirements. The reason for using red light rather than shorter wavelengths, which actually are absorbed more strongly by Photofrin®, is that the red light is considerably more penetrating through tissue [35] due in part to the presence in tissue

of strongly absorbing melanin and hemoglobin. Light scattering is also much greater at shorter wavelengths. The choice of 630 nm light, normally used in PDT, is therefore a compromise between optimal tissue transmission and Photofrin® absorption.

First generation photosensitizers

The original HPD material (also designated as Photofrin I) [13] and the purified HPD material known as Photofrin® (initially known as Photofrin II) [15] represent the first generation of photosensitizers. A number of problems in PDT are the consequence of the complex nature and instability of the first generation photosensitizers. They vary in composition from preparation to preparation and have been observed to degrade with time to yield inactive side products [36]. The commercial Protofrin® was originally shipped and stored at -78°C and only warmed to room temperature immediately prior to use, a freeze dried preparation is now available. Other disadvantages of the first generation photosensitizers are the weak absorption at 630 nm (presumably requiring larger doses of drug to obtain a satisfactory therapeutic effect), the poor selectivity for tumor tissues, and the long retention period (2-3 months) in cutaneous tissues, which causes skin photosensitivity. Research in the last 15 years has turned to the preparation of the so-called second generation photosensitizers for PDT. These are mostly pure compounds, with long wavelength absorptions and enhanced photoactivity compared with Photofrin®. Table 1 lists the long wavelength absorptions and extinction coefficients of Photofrin and some second generation photosensitizers. A new approach to increase selective localization of the photosensitizers in tumor tissues and reduce skin photosensitivity, consists of second generation photosensitizers bound to special carriers.

Table 1. **Long wavelength absorption maxima and extinction coefficients of some typical PDT photosensitizers**

Photosensitizer	λ_{max} (nm)	ε (L.mol⁻¹.cm⁻¹)
Photofrin	630	3000
Chlorin p6	664	43000
Natural bacteriochlorin	785	150000
Benzoporphyrin	690	30000
Benzochlorin	660	35000
Azachlorin	670	50000
Zn-etioporphyrin	690	70000
Tetrabenzoporphyrin	685	120000
Zn-phthalocyanine	675	150000
Porphycene	630	52000

The basic requirements of a PDT photosensitizer are that it should be minimally toxic in the dark, have long wavelength absorptions ($\lambda > 630$ nm) with high extinction coefficients ($\varepsilon > 30000$ L.mol⁻¹.cm⁻¹), be preferentially localized in tumor tissue, have limited *in vivo* stability for rapid clearance after treatment, and have favorable photophysical properties. The most important photophysical properties of the photosensitizer are the energy ($E_T \geq 94$ kJ.mol⁻¹), lifetime ($\tau_T > 100$ ms), and quantum yield ($\phi_T > 0.4$) of the triplet state. For the singlet oxygen mechanism of tumor destruction, the quantum yield of singlet oxygen ($\phi_\Delta > 0.2$) is also an important parameter. It is also very important that the photosensitizer should have a short, high-yielding and inexpensive synthetic route leading to a single pure substance.

The light penetration through tissues increases (typically doubles from around 550 nm to 630 nm and then again from 630 nm to 750 nm) and the scattering of light decreases with the wavelength. It might be expected that photosensitizers with the longest wavelength absorptions would be more adequate for the treatment of bulky tumors. However, there is a limit for the value of the maximum wavelength of absorption of the photosensitizer due to the requirement for singlet oxygen generation. The "phototherapeutic window" has been reported to include light in the 600-1000 nm spectral region. The photosensitizer energy of the triplet state should be greater than the energy of the singlet oxygen, which is 94 kJ.mol⁻¹ (1270 nm), for efficient singlet oxygen production. For some potential photosensitizers with absorptions near 1000 nm, the quantum yield of singlet oxygen is zero probably because of their low energy of the triplet state ($E_T < 94$ kJ.mol⁻¹). It has also been observed that some long-wavelength absorbing drugs containing extended π-systems are less kinetically stable and more subject to photobleaching [5]. Therefore, the photochemical limitation to the long wavelength of a photosensitizer is about 800 nm. Light of this wavelength penetrates, in lightly pigmented tissues, up to 2-3 cm.

Second generation photosensitizers

Since the the early 1980s new improved photosensitizers related to Photofrin® have been synthesized and reported [1-6, 37]. These are the so-called second generation photosensitizers and some of them are already in Phase I and II clinical trials. These photosensitizers are based on cyclic tetrapyrrole molecules with intensified long-wavelength absorptions. Only the metal-free or the diamagnetic metal complexes (e.g. Al, Zn, Sn, Si, Ge, Ga, Cd) of these macrocycles can be used in PDT, since a paramagnetic ion would quench the photochemistry necessary for sensitization.

The first second generation photosensitizers consisted of pure porphyrin dimers and trimers linked by ether, ester, and carbon-carbon double bonds, in a

mimic of the presumably active components of Photofrin® [38]. However, these compounds showed low photoactivity compared to Photofrin®. By judicious substitution of the porphyrin ring it is possible to move the long wavelength absorption band of the porphyrin spectrum further to the red region. However the effect is small and the extinction coefficient of the longest wavelength absorption is only modestly increased. Therefore research has turned to the synthesis of chlorin and bacteriochlorin type macrocycles. Reduction of the porphyrin macrocycle (for instance with diimide) leads to the formation of chlorins (λmax = 650-690 nm) (Figure 2) and bacteriochlorins (λmax = 720-760 nm) which have red-shifted, high extinction coefficient absorptions, and which allow in principle the use of lower doses of photosensitizer. It has also been reported that chlorins do not cause severe cutaneous photosensitization as porphyrins usually do [39]. Natural chlorins, such as chlorophyll-a (13) and bacteriochlorophyll-a (14) have been used as photosensitizers for PDT [40]. Some chlorophyll-a derivatives were prepared mainly by demetallation, cleavage of the phytyl group, and reactions on the isocyclic cyclopentanone ring of (13) [41]. For example chlorin e_6 (15) [42], N-aspartylchlorin e_6 (16) [43], chlorin p_6 (17) [44] and its lysyl derivative (18) [45] are all active in PDT. Chlorin e_6 (15) is obtained from chlorophyll-a (13) by demetallation, transesterification using methanol/5% sulfuric acid, cleavage of the cyclopentanone ring with sodium methoxide/methanol, and basic hydrolysis of the resulting methyl esters. Chlorin p_6 (17) is obtained from purpurin-18 methyl ester (19), a chlorophyll-a degradation product, by simple hydrolysis of the anhydride ring and the methyl esters. Lysyl chlorin p_6 (18) is prepared by treatment of purpurin-18 (19) with lysine in a mixture of dichloromethane, pyridine, and water. The bacteriochlorin (20) has a long-wavelength absorption at 815 nm, and has shown promising anti-tumor activity [46]. The bacteriochlorin (20) is also prepared from purpurin-18 methyl ester (19). The anhydride ring in (19) is first replaced with the imide ring in (20) by reacting (19) with lysine ethyl ester followed by cyclization of the open chain product with Montmorillonite K10 clay suspended in dichloromethane. The β-vinyl group is then converted into the β-formyl group by reaction with osmium tetroxide/sodium periodate. This conversion produces a 30 nm red shift in the optical spectrum whereas the imide ring produces a 40 nm red shift relative to the open chain amide product. The *vic*-dihydroxy-bacteriochlorin (20) is produced by the reaction of the β-formyl-chlorin analogue with osmium tetroxide/pyridine, and then with hydrogen sulfide gas, which cleaves the intermediate osmate complex. Many other potential photosensitizers have been prepared from compound (19) since it is possible to open the anhydride ring of (19) with a number of different kinds of nucleophiles, such as amino acids.

Some synthetic chlorins and bacteriochlorins have been found to be good photosensitizers for PDT. For

example, *meso*-tetrakis(*m*-hydroxyphenyl)chlorin (21) has been used in clinical trials since 1991 [5, 47]. Chlorin (21) was prepared by reduction, with diimide, of the *meso*-tetrakis(*m*-hydroxyphenyl)porphyrin, which was synthesized from the corresponding *meso*-tetrakis(*m*-methoxyphenyl)porphyrin by cleavage of the methyl ethers with BBr_3 at low temperatures. The *meso*-tetrakis(*m*-methoxyphenyl)porphyrin is prepared in moderate yields, in a one step reaction, by condensation in acidic media of pyrrole and *m*-methoxybenzaldehyde. Although simple to prepare, chlorin (21) causes skin photosensitivity of the patients, presumably in part due to its different structure (it has a *meso* rather than a β substituted macrocycle) from the natural occurring chlorins. A disadvantage of using chlorins and bacteriochlorins as photosensitizers for PDT is their re-oxidation back to porphyrins, with loss of the intense long-wavelength absorption necessary for deeper tissue penetration and greater photosensitizing activity. Furthermore, *in vivo* oxidation of the photosensitizers may result in the formation of a new chromophore absorbing at a different wavelength, thus reducing the photodynamic efficiency. In order to prevent dehydrogenation, chemically stable chlorin macrocycles having an isocyclic ring or containing a keto or geminal alkyl groups [48] were synthesized. Examples are the oxochlorin (22) [49], the benzoporphyrin derivative monocarboxylic acid (BPDMA) (23) [50] and the etiopurpu-
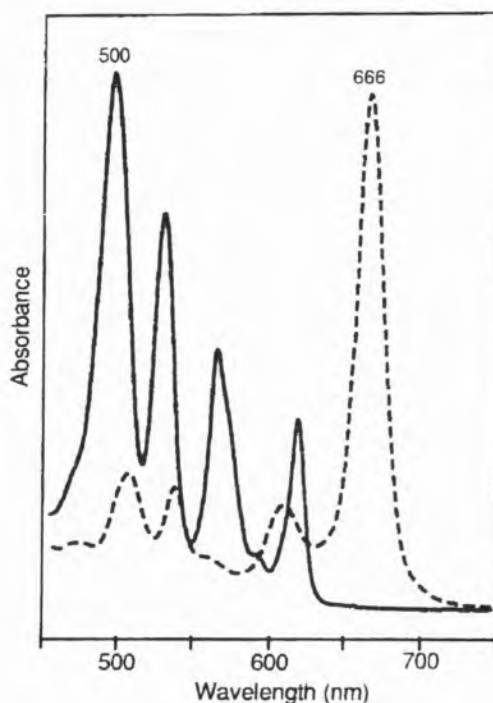
Figure 2 – Typical optical spectra (450-750 nm), of a porphyrin (—) and a chlorin (– – –).

rin (**24**) [51], which have already been used in successful clinical trials. The main step in the preparation of oxochlorin (**22**) is the oxidation of the starting porphyrin with osmium tetroxide followed by an acid-catalyzed pinacolic rearrangement (Scheme 1). The treatment of porphyrins with osmium tetroxide and the migratory aptitudes in the pinacolic rearrangement have been reported [52]. It has been shown that the osmium tetroxide reaction can be directed to give bacteriochlorins if the substrates in the reaction are chlorins (e.g. in the synthesis of bacteriochlorin (**20**)). The BPDMA (**23**) was prepared from protoporphyrin-IX (**4**) by the Diels-Alder [4+2] cyclization reaction using dimethyl acetylenedicarboxylate as the dienophile, followed by reaction with base. Triethylamine and 1,8-diazabicyclo [5.4.0]undec-7-ene (DBU) are used to promote rearrangement of the Diels-Alder adduct intermediate to give the cis-cyclohexadiene product. Recently, some derivatives of BPDMA with good photodynamic activity have been reported [53]. The etiopurpurin (**24**) was prepared by the intramolecular cyclization of a *meso*-acrylic acid chain onto the adjacent β-position, under mild conditions. The *meso*-acrylic acid chain is introduced by Vilsmeier reaction (N,N-dimethylformamide/POCl$_3$) followed by the Wittig reagent (carbethoxymethylene)triphenyl phosphorane. More recently, other promising chlorin and bacteriochlorin macrocycles have been synthesized. Examples are the bacterichlorin (**25**) [54], the benzochlorin (**26**) [55], and the naphthochlorin (**27**) [56]. The bacteriochlorin (**25**) was prepared by the double cyclization of an acrolein and an acrylic acid chains on two adjacent *meso* positions of octaethylporphyrin (OEP), using trifluoroacetic acid. Compound (**25**) shows an intense absorption at 890 nm. Benzochlorins are in pre-clinical trials and have demonstrated good tumoricidal activity [57]. Benzochlorin (**26**) was prepared from OEP as seen in Scheme 2. The acrolein side chain was introduced by the Vilsmeier reaction, using 3-(dimethylamino)acrolein and phosphorus oxychloride. The cyclization of the *meso*-acrolein chain, in concentrated sulfuric acid, onto the adjacent β-position of the macrocycle afforded (**26**) in 40% overall yield. The naphthochlorin (**27**) was prepared from the readily available *meso*-tetrakis(*p*-methoxyphenyl)porphyrin (TMPP), as can be seen in Scheme 3. The intramolecular cyclization of the β-vinyl group into the *ortho* position of the adjacent phenyl ring afforded (**27**) in an overall yield of 50%. Research is now in progress to demetallate naphthochlorin (**27**) and to cleave the methoxyl groups in the presence of BBr$_3$, to generate the free-base naphthochlorin (**28**). The starting porphyrins OEP and TMPP are easily prepared in one step due to their high symmetry [58].

Second generation photosensitizers derived from phthalocyanines (**29**) [59] and naphthalocyanines (**31**) [60], such as (**30**) and (**32**), are currently in clinical trials and show good photobiological activity. Phthalocyanines (λmax = 680-720 nm) and naphthaloc-

Scheme 1 – Vicinal hydroxylation to give a dihydroxy-chlorin and acid catalyzed pinacolic rearrangement to give the oxochlorin.

yanines (λmax = 760-800 nm) absorb light of longer wavelength with higher extinction coefficients compared to porphyrins, due to the extended conjugated π-system. Furthermore, phthalocyanines and naphthalocyanines absorb minimally in the wavelength region 400-

600 nm, so that induced skin sensitity to sunlight is smaller with these compounds than with porphyrins. Both macrocycles (**29**) and (**31**) are readily prepared by reductive tetramerization of, respectively, phthalonitriles and naphthalene-2,3-dinitriles, or equivalent monomers. The tetramerization reaction occurs in the presence of a metal or metal salt which acts both as a template and an electron source. The disadvantage of phthalocyanines is their high *in vivo* photostability, which causes extended skin sensitity in the patients.

Other reported photosensitizers for PDT that show strong absorption bands at long wavelengths include tetrabenzoporphyrin (**33**) [61], the azachlorin (**34**) [62], the texaphyrin (**35**) [63], and the porphycene (**36**) [64]. The tetrabenzoporphyrin (**33**) and other benzoporphyrin derivatives have been successfully used in *in vivo* PDT studies. However the literature methods for the synthesis of these type of compounds give low yields of impure products and new synthetic routes are currently being developed [65]. Azachlorins have a nitrogen atom in the place of one methine bridge of the chlorin macrocycle, which confers a higher extinction coefficient of the long wavelength absorption [66]. Although azachlorin (**34**) has not yet been tested in *in vivo* PDT studies, it has good photophysical properties

for sensitization. Azachlorins, like azaporphyrins, are prepared from the naturally occurring bile pigment bilirubin. The bilirubin is first converted into biliverdin which reacts with zinc acetate and then with acetic anhydride to produce the corresponding zinc oxoniaprotoporphyrin. This compound is transformed into the azaprotoporphyrin by cleavage of the oxonia bridge with ammonia, followed by activation of the lactam oxygen with trimethylsilyl polyphosphate (PPSE) and recyclization in pyridine (Scheme 4). The resulting azaprotoporphyrin is converted into azachlorin (**34**) by reaction with singlet oxygen, reduction of the aldehyde functions, cleavage of the porphyrin glycol formed, reduction with sodium borohydride, and amide acetal Claisen rearrangement of the intermediate allylic alcohol. Texaphyrins are expanded porphyrins that absorb strongly in the 720-780 nm spectral region. The lanthanum complex of texaphyrin (**35**) has been shown to be an efficient singlet oxygen producer and photoactive in *in vivo* experiments. These type of compounds are prepared by the Schiff base condensation of diformyltripyrranes with *ortho*-diaminobenzene derivatives, followed by aromatization using a metal salt, a base and air. Porphycene (**36**) has a strong absorption in the red region of the absorption spectrum and was reported to be a good *in vivo* tumor localizer. However these types of compounds are produced only in fairly low yields from the coupling reaction of the corresponding diformyl-bipyrroles, in the presence of low-valent titanium complexes.

The porphyrin, phthalocyanine and porphycene macrocycles are all hydrophobic, so many of the reported new effective photosensitizers (e.g. (**24**), (**25**), (**26**), (**30**), (**33**), and (**36**)) are insoluble in water. In order to obtain water solubility for injection into the bloodstream, polar hydrophilic substituents were introduced, such as sulfonic acid, carboxylic acid, hydroxyl, and quaternary ammonium salt functionalities. Derivatives of chlorophyll-a (**13**) such as (**15**), (**16**), (**17**), and (**18**) contain hydrophilic carboxylic acid groups and exhibit good tumor localization. Amongst the *meso*-tetraarylporphyrins the 3-hydroxy- and the 3,4-dihydroxyphenyl derivatives have been reported to be 25-30 times as potent as Photofrin® in sensitizing tumors [67]. Positively charged porphyrins and phthalocyanines were shown to exhibit significant tumor photonecrosis [68]. The photodynamic properties of sulfonated aluminium (III) phthalocyanines (**29**, R = SO_3H) have been studied and reported to be significantly influenced by the degree of sulfonation (the mixture of the disulfonic acid derivatives is the most active photosensitizer) [69]. The photosensitizer properties for effective *in vivo* tumor localization are not yet completely understood but seem to be connected with the lipophilicity and aggregation behavior of the sensitizers. Highly lipophilic photosensitizers are poorly soluble and strongly aggregated in aqueous solutions, whereas hydrophilic ones generally show lower cell membrane penetrating properties. It has
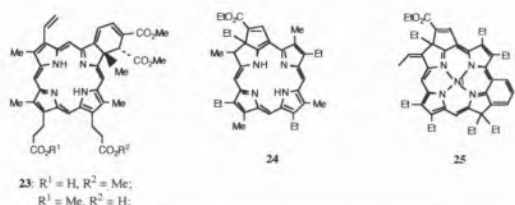
Scheme 2 – Synthesis of a benzochlorin. a) Cu(OAc)₂/CHCl₃; b) 3-DMA/POCl₃, CH₂Cl₂; c) NaHCO₃, sat. aq.; d) conc. H₂SO₄,2h, RT.
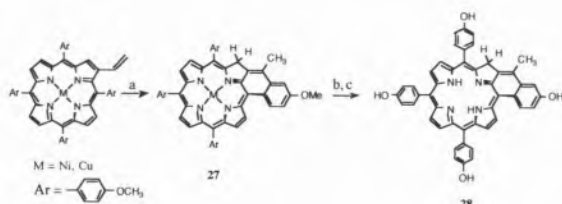
Scheme 3 – Synthesis of a naphthochlorin. a) dil. H₂SO₄; b) conc. H₂SO₄; c) BBr₃

been reported that macrocycles containing a suitable combination of hydrophilic (for solubilization in the aqueous media) and hydrophobic (for interactions with the lipidic part of cell membranes) substituents orient preferably in the cell membrane allowing a better tumor accumulation [6, 67b, 70]. The effect of varying the hydrophobicity of the macrocycle by changing the length of the alkyl side chains has been shown to have a significant response on *in vivo* tumor damage [71]. The attachment of hydrophilic carbohydrate structural units to the chlorin macrocycle [50] and the synthesis of neutral glycosylated porphyrins derived from *meso*-tetraphenylporphyrin [72] have been reported.

The hydrophobic second generation photosensitizers, e.g. (**24**), (**25**), (**26**), (**29**), (**31**), (**33**), and (**36**), have been administered *in vivo* in an emulsifying agent, such as a polymer or a liposomal preparation [73]. Some of the transport agents used include Cremophor EL (CRM, polyoxyethyleneglycol triricinoleate), Tween 80 (TW80, polyoxyethylene sorbitan monoleate), and DPPC (dipalmitoyl phosphatidylcholine). It has been reported that the delivery system can greatly affect the uptake of the hydrophobic photosensitizers by the tumors [74], and there are problems concerning regulatory approval of these drug/delivery vehicle combinations. Carrier polymers, such as methoxy(polyethylene) glycol and polyvinylalcohol, have the disadvantage of exhibiting longer retention times in the serum [6]. Photosensitizers containing both hydrophilic and hydrophobic groups have also been coupled to delivery systems.

29: R = H
30: R = OC₄H₉

31: R = H
32: R = NHCOCH₃

33
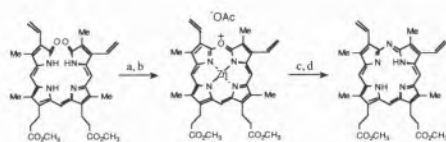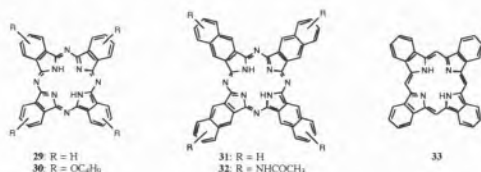
Scheme 4 – Synthesis of a azaporphyrin from a zinc oxoniaporphyrin, which is prepared from biliverdin. a) Zn(OAc)₂/THF; b) Ac₂O/THF; c) NH₃/CH₃CN; d) PPSE, Py

34

35

36
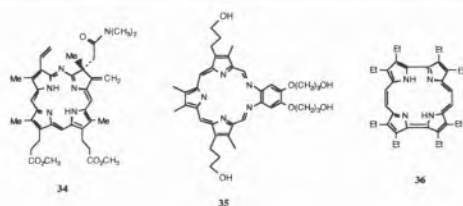
It is generally accepted that the patterns of biodistribution of the photosensitizers are correlated with the association to low-density lipoprotein (LDL) and high-density lipoprotein (HDL) receptors in *in vivo* normal and tumor tissues [75]. The plasma protein LDL is a natural carrier of porphyrins in blood and can incorporate more than 50 porphyrin molecules. The role of LDL in the accumulation of porphyrins in tumor tissues has been demonstrated in cellular models [76]. Cancer cells exhibit high levels of LDL receptors, which can account for the accumulation of porphyrins in tumor tissues. It has been reported that LDL can also be used as an efficient delivery system for the photosensitizers [77]. Certain drugs, such as compactin and lovastatin, known to increase the expression of the LDL receptor in cells, have been reported to significantly increase PDT efficiency [78]. *In vivo* studies have indicated the importance of both the photodynamic properties of the sensitizer and the choice of the delivery vehicle as determinants for PDT efficacy.

An interesting alternative to the injection of the photosensitizer is its generation within the tissue. It has been shown that 5-aminolevulinic acid (ALA), a biosynthetic precursor of heme, can be efficiently used in PDT [79]. The external administration of ALA leads to the formation of protoporphyrin-IX (**4**), the immediate precursor of heme, in photosensitizing concentrations. However, only certain type of cells, including cancer cells, can synthesize protoporphyrin-IX (**4**) after ALA administration, which accounts for the selectivity of ALA-induced phototoxicity in PDT. Most of the clinical studies performed using this technique have involved the topical application of ALA as a cream to skin lesions [80]. In a few cases ALA has been given orally or injected, which generalizes this type of treatment to internal tumors [81]. Since the protoporphyrin-IX (**4**) is synthesized within the mitochondria of living cells, it accumulates inside those cells and little or no protoporphyrin-IX is present in the general circulation. Therefore no skin photosensitivity is usually detected in this treatment. The rapid photobleaching of ALA-induced protoporphyrin-IX in normal skin, with the production of photoproducts, has been reported [82].

The New Approach

A major goal of PDT is to preferential destroy tumor cells while sparing normal tissues. The mechanism for tumor localization of the photosensitizers is poorly understood, and it seems to depend on many variables such as the photosensitizer, the delivery system and the type of tumor. A new approach for the selective delivery of the photosensitizers to tumor tissues has been developed, and it is designated as antibody-targeted photolysis (ATPL). This new approach uses photosensitizers coupled to monoclonal antibodies which bind specifically to the malignant cell surface

antigens [6]. The malignant tumor cells have different cell surface antigens from those of normal cells. Therefore such conjugates can eliminate skin photosensitivity and diminish toxic effects on the nontarget normal tissues. Since the monoclonal antibodies are responsible for the selective localization of the antibody-photosensitizer conjugate in the tumor tissues, the photosensitizers used are selected for their binding capacities and photophysical properties. The antibody-bound porphyrins and chlorins totally retain their photophysical properties [83]. A suitable functional group on the photosensitizer is required for the direct binding to the monoclonal antibodies. Carboxylic acid groups have been used to form amide bonds with the amino groups on lysine residues of the antibody. Several sulfonated macrocycles were coupled using N-hydroxysuccinimidyl-3-(2-pyridyldithio)propionate as the linking agent [84]. However, when the photosensitizers bind near the antigen binding sites, inactivation of the antibodies can occur. To retain the antigen-binding activities the photosensitizers have been coupled to carriers, such as polyvinylalcohol and low molecular weight dextrans [85]. The resulting conjugates have been reported to be efficient generators of singlet oxygen and very selective for tumor tissues. In the last ten years many different photosensitizers conjugated to antibodies have been used in the diagnosis and treatment of cancer [6, 86].

Conclusions

Although many new promising photosensitizers for PDT have been synthesized and reported in the last 15 years, biological activity tests are only known for a small part. Many major pharmaceutical companies have not demonstrated much interest in this area, probably because PDT effectiveness depends on a lot of factors. The effect of a particular photosensitizer on a specific type of tumor is difficult to predict and the same PDT conditions can have different effects on different types of tumors and patients. In the future new improved sensitizers will undoubtedly be reported. Work will be done to elucidate the photochemical mechanisms to generate the cytotoxic species and the photobleaching of the photosensitizers. A better control of the *in vivo* behavior of the sensitizers will allow a more widespread application of the PDT treatment. Finally, the application of PDT to inactivate viruses in blood, such as the herpes simplex virus (HSV) and the human immunodeficiency virus (HIV), is currently the subject of intense interest and research.

Acknowledgments

References

1. S. B. Brown, T. G. Truscott, *Chemistry in Britain* (1993) 955.

2. T. J. Dougherty, *Photochem. Photobiol.* **58** (1993) 895.

3. G. Jori, *J. Photochem. Photobiol. A: Chem.* **62** (1992) 371.

4. F.-P. Montforts, B. Gerlach, F. Höper, *Chem. Rev.* **94** (1994) 327.

5. R. Bonnett, *Chem. Soc. Rev.* (1995) 19.

6. D. Wohrle, A. Weitemeyer, A. Hirth, U. Michelsen, in *Photochemical Energy Conversion, Fundamentals and Applications*, M. Kaneko Ed.; Industrial Publishing & Consulting Inc.: Tokyo, 1996, in press.

7. O. Raab, *Z. Biol.* **39** (1900) 524.

8. A. Jesionek and V. H. Tappeiner, *Muench. Med. Wochschr.* **47** (1903) 2042.

9. a) W. H. Hausman, *Biochem. Z.* **14** (1908) 275; b) W. H. Hausman, *Wien. Klin. Wchneschr.* **22** (1909) 1820.

10. H. Auler and G. Banzer, *Ztschr. f. Krebsforsch.* **53** (1942) 65.

11. F. H. J. Figge, *Univ. Md. Med. Bull.* **26** (1942) 165.

12. e.g. a) L. O. J. Manganiello and F. H. J. Figge, *Bull. School Med. Univ. Maryland* **36** (1951) 3; b) F. H. J. Figge and G. C. Peck, *Anat. Rec.* **115** (1953) 306; c) D. S. Rassmussen-Taxdal, G. E. Ward and F. H. J. Figge, *Cancer* **8** (1955) 78; d) F. H. J. Figge, W. K. Diehl, G. C. Peck and H. P. Mack, *Cancer Res.* **2** (1956) 105.

13. a) R. L. Lipson and E. J. Baldes, *Arch. Dermat.* **82** (1960) 508; b) R. L. Lipson, E. J. Baldes and A. M. Olsen, *J. Natl. Cancer Inst.* **26** (1961) 1; c) R. L. Lipson, E. J. Baldes and A. M. Olsen, *J. Thorac. Cardiov. Surg.* **42** (1961) 623.

14. a) P. S. Clezy, T. T. Hai, R. W. Henderson and L. van Thuc, *Aust. J. Chem.* **33** (1980) 585; b) R. Bonnett, R. J. Ridge and P. A. Scourides, *J. Chem. Soc. Perkin Trans. 1* (1981) 3135; c) M. C. Berenbaum, C. R. Bonnett and P. A. Scourides, *Brit. J. Cancer* **45** (1982) 571; d) D. Kessel and T. Chow, *Cancer Res.* **43** (1983) 1994; e) J. F. Evensen, S. Sommer, J. Moan and T. Christensen, *Cancer Res.* **44** (1984) 482; f) D. Kessel and M.-L. Cheng, *Cancer Res.* **45** (1985) 3053; g) J. Moan, *Photochem. Photobiol.* **43** (1986) 681.

15. a) T. J. Dougherty, *Photochem. Photobiol.* **38** (1983) 377; b) T. J. Dougherty, D. G. Boyle, K. R. Weishaupt, B. A. Henderson, W. R. Potter, D. A. Bellnier and K. E. Wityk, in *Porphyrin Photosensitization*, D. Kessel and T. J. Dougherty Eds.; Plenum Press: New York, 1983, p. 3; c) T. J. Dougherty, D. G. Boyle, K. R. Weishaupt, B. A. Henderson, W. R. Potter, D. A. Bellnier and K. E. Wityk, *Adv. Exp. Med. Biol.* **160** (1983) 3.

16. a) T. J. Dougherty, W. R. Potter and K. R. Weishaupt, in *Porphyrins in Tumor Phototherapy*, A. Andreoni and R. Cubeddu Eds.; Plenum Press: New York, 1984, p. 23; b) T. J. Dougherty, W. R. Potter and K. R. Weishaupt, in *Porphyrin Localization and Treatment of Tumors*, D. Doiron and C. J. Gomer Eds.; Alan R. Liss: New York, 1984, p. 301.

17. a) D. Kessel, in *Photodynamic Therapy of Tumors and Other Diseases*, G. Jori and C. Perria Eds.; Plenum Press: New York, 1985, p. 1; b) D. Kessel, C. K. Chang and B. Musselman, in *Methods in Porphyrin Photosensitization*, D. Kessel Ed.; Plenum Press: New York, 1985, p. 213; c) D. Kessel, P. Thompson, B. Musselman and C. K. Chang, *Cancer Res.* **47** (1987) 4642.

18. a) E. J. Land, R. W. Redmond and T. G. Truscott, *Cancer Lett.* **32** (1986) 181; b) R. W. Boyle, W. F. Keir, A. H. McLennan, G. Maguire and T. G. Truscott, *Cancer Lett.* **38** (1987) 9.

19. a) R. Bonnett and M. C. Berenbaum, *Adv. Exp. Med. Biol.* **160** (1983) 241; b) C. J. Byrne, L. V. Marshallsay and A. D. Ward, *Photochem. Photobiol.* **46** (1987) 575; c) D. Kessel, P. Thompson, B. Musselman and C. K. Chang, *Photochem. Photobiol.* **46** (1987) 563.

20. A. F. Mironov, A. N. Nizhnik, A. Y. Nockel, *J. Photochem. Photobiol., B: Biol.* **4** (1990) 297.

21. a) D. Kessel, *Biochem.* **16** (1977) 3443; b) J. Moan, H. Waksvik and T. Christensen, *Cancer Res.* **40** (1980) 2915; c) D. A. Bellnier and T. J. Dougherty, *Photochem. Photobiol.* **36** (1982) 43; d) B. W. Henderson and G. Farrell, *Proc. SPIE* **1065** (1989) 2; e) M. Geze, P. Morliere, J. C. Maziere, K. M. Smith, R. Santus, *J. Photochem. Photobiol., B: Biol.* **20** (1993) 23.

22. C. J. Gomer and T. J. Dougherty, *Cancer Res.* **39** (1979) 146.

23. a) B. W. Henderson, *Photochem. Photobiol. Suppl.* **57** (1993) 17S; b) V. H. Fingar, *Photochem. Photobiol. Suppl.* **57** (1993) 18S.

24. R. A. Ackerman, J. N. Pitts, Jr. and I. Rosenthal, Preprints of papers, Div. of Petroleum Chemistry, Inc., *Amer. Chem. Soc.* **16** (1971) A25.

25. C. J. Gomer, *Photochem. Photobiol.* **37S** (1983) 91.

26. a) K. R. Weishaupt, C. J. Gomer and T. J. Dougherty, *Cancer Res.* **36** (1976) 2326; b) L. Ma, J. Moan, K. Berg, *Int. J. Cancer* **57** (1994) 883.

27. J. Moan, E. O. Pettersen and T. Christensen, *Brit. J. Cancer* **39** (1979) 398.

28. R. S. Becker, A. L. Maçanita, *Rev. Port. Quím.* **2** (1995) 30.

29. H. V. D. Bergh, *Chemistry in Britain* (1986) 430.

30. J. Moan and K. Berg, *Photochem. Photobiol.* **55** (1992) 931.

31. a) T. S. Mang, T. J. Dougherty, W. R. Potter, D. G. Boyle, S. Somer, J. Moan, *Photochem. Photobiol.* **45** (1987) 501; b) J. Moan, K. Berg, *Photochem. Photobiol.* **53** (1991) 549.

32. G. Jori and J. D. Spikes, in *Topics in Photomedicine*, K. C. Smith Ed.; Plenum Press: New York, 1984, p. 183.

33. E. F. G. Dickson, R. H. Pottier, *J. Photochem. Photobiol., B: Biol.* **29** (1995) 91.

34. T. H. Foster, S. L. Gibson, L. Gao, R. Hilf, *Proc. SPIE* **1645** (1992) 104.

35. T. J. Dougherty, *Adv. Exp. Med. Biol.* **193** (1985) 313.

36. T. J. Dougherty, *Photochem. Photobiol.* **45** (1987) 879.

37. K. M. Smith, *in* Photodynamic Therapy of Neoplastic Disease, Volume II, D. Kessel Ed.; CRC Press, Boca Raton, 1990; pp 145-168.

38. a) I. K. Morris, A. D. Ward, *Tetrahedron Lett.* **29** (1988) 2501; b) R. K. Pandey, M. G. H. Vicente, F.-Y. Shiau, T. J. Dougherty, K. M. Smith, *Proc. SPIE* **1426** (1991) 356; c) R. K. Pandey, F.-Y. Shiau, T. J. Dougherty, K. M. Smith, *Tetrahedron* **47** (1991) 9671; d) D. Kessel, C. K. Chang, B. W. Henderson, *J. Photochem. Photobiol., B: Biol.* **18** (1993) 177.

39. C. J. Gomer, A. Ferrario, *Cancer Res.* **50** (1990) 3985.

40. a) R. K. Pandey, F.-Y. Shiau, I. Meunier, S. Ramaprasad, A. B. Sumlin, T. J. Dougherty, K. M. Smith, *Proc. SPIE* **1645** (1992) 264; b) K. M. Smith, R. K. Pandey, F.-Y. Shiau, N. W. Smith, P. Iakovides, T. J. Dougherty, *Proc. SPIE* **1645** (1992) 274.

41. a) R. K. Pandey, F.-Y. Shiau, K. Ramachandran, T. J. Dougherty, K. M. Smith, *J. Chem. Soc., Perkin Trans. 1* (1992) 1377; b) S-J. H. Lee, N. Jagerovic, K. M. Smith, *J. Chem. Soc., Perkin Trans. 1* (1993) 2369; c) R. K. Pandey, S. Constantine, D. A. Goff, A. N. Kozyrev, T. J. Dougherty, K. M. Smith, *Bioorg. Med. Chem. Lett.* **6** (1996) 105.

42. G. A. Kostenich, I. N. Zhuravkin, A. V. Furmanchuk, E. A. Zhavrid, *J. Photochem. Photobiol., B: Biol.* **17** (1993) 187.

43. a) W. G. Roberts, F.-Y. Shiau, J. S. Nelson, K. M. Smith, M. W. Berns, *J. Natl. Cancer, Inst.* **80** (1988) 330; b) J. D. Spikes, J. C. Bommer, *J. Photochem. Photobiol., B: Biol.* **17** (1993) 135.

44. a) G. W. Kenner, S. W. McCombie and K. M. Smith, *J. Chem. Soc., Perkin Trans. 1* (1973) 2517; b) J. K. Hoober, T. W. Sery, N. Yamamoto, *Photochem. Photobiol.* **48** (1988) 579; c) R. Bachor, C. R. Shea, R. Gillies, T. Hasan, *Proc. Natl. Acad. Sci. USA* **88** (1991) 1580.

45. a) M. W. Leach, R. J. Higgins, S. A. Autry, J. E. Boggan, S-J. H. Lee, K. M. Smith, *Photochem. Photobiol.* **58** (1993) 653; c) D. Kessel, K. Woodburn, C. J. Gomer, N. Jagerovic, K. M. Smith, *J. Photochem. Photobiol., B: Biol.* **28** (1995) 13.

46. a) D. Kessel, K. M. Smith, R. K. Pandey, F.-Y. Shiau, B. W. Henderson, *Photochem. Photobiol.* **58** (1993) 200; b) K. Pandey, F.-Y. Shiau, A. B. Sumlin, T. J. Dougherty, K. M. Smith, *Bioorg. Med. Chem. Lett.* **4** (1994) 1263; c) R. K. Pandey, N. Jagerovic, T. J. Dougherty, K. M. Smith, *Proc. SPIE* **2325** (1994) 2.

47. J.-F. Savary, P. Monnier, G. Wagnières, D. Braichotte, C. Fontolliet, H. van den Bergh, *Proc. SPIE* **2078** (1994) 330.

48. a) J. W. Bats, G. Haake, A. Meier, F.-P. Montforts, G. Scheurich, *Liebigs Ann.* (1995) 1617; b) D. Kusch, E. Töllner, A. Lincke, F.-P. Montforts, *Angew. Chem. Int. Edn. Engl.* **34** (1995) 784.

49. K. Woodburn, C. K. Chang, S. Lee, B. Henderson, D. Kessel, *Photochem. Photobiol.* **60** (1994) 154.

50. a) A. M. Richter, B. Kelly, J. Chow, D. J. Liu, G. M. N. Towers, D. Dolphin, J. G. Levy, *J. Natl. Cancer Inst.* **79** (1987) 1327; b) D. Dolphin, *Can. J. Chem.* **72** (1994) 1005; c) B. M. Aveline, T. Hasan, R. W. Redmond, *J. Photochem. Photobiol., B: Biol.* **30** (1995) 161.

51. A. R. Morgan, G. M. Garbo, R. W. Keck, L. D. Eriksen, S. H. Selman, *Photochem. Photobiol.* **51** (1990) 589.

52. a) C. K. Chang, C. Sotiriou, W. Wu, *J. Chem. Soc., Chem. Commun.* (1986) 1213; b) C. K. Chang, C. Sotiriou, *J. Heterocycl. Chem.* **22** (1985) 1739.

53. a) R. K. Pandey, N. Jagerovic, J. M. Ryan, T. J. Dougherty, K. M. Smith, *Tetrahedron* **52** (1996) 5349; b) I. Meunier, R. K. Pandey, M. O. Senge, T. J. Dougherty, K. M. Smith, *J. Chem. Soc., Perkin Trans. 1* (1994) 961.

54. A. L. Morgan, S. Gupta, *Tetrahedron Lett.* **35** (1994) 4291.

55. a) M. G. H. Vicente, K. M. Smith, *Tetrahedron Lett.* **31** (1990) 1365; b) M. G. H. Vicente, K. M. Smith, *J. Org. Chem.* **56** (1991) 4407.

56. M. A. Faustino, M. G. P. M. S. Neves, M. G. H. Vicente, A. M. Silva, J. A. S. Cavaleiro, *Tetrahedron Lett.* **36** (1995) 5977.

57. D. Kessel, A. R. Morgan, *Photochem. Photobiol.* **58** (1993) 521.

58. K. M. Smith, in *Porphyrins and Metalloporphyrins*; K. M. Smith Ed.; Elsevier Science Ltd: Amsterdam, 1975; pp 32-33.

59. a) I. Rosenthal, *Photochem. Photobiol.* **53** (1991) 859; b) M. Shopova, V. Mantareva, K. Krastev, D. Hadjiolov, A. Milev, K. Spirov, G. Jori, F. Ricchelli, *J. Photochem. Photobiol., B: Biol.* **16** (1992) 83; c) D. Phillips, *Pure & Appl. Chem.* **67** (1995) 117.

60. a) N. C. Yates, J. Moan, A. Western, *J. Photochem. Photobiol., B: Biol.* **4** (1990) 379; b) D. Wöhrle, M. Shopova, S. Müller, A. D. Milev, V. N. Mantareva, K. K. Krastev, *J. Photochem. Photobiol., B: Biol.* **21** (1993) 155.

61. a) Wolford, S. T.; Novicki, D. L.; Kelly, B. *Fundam. Appl. Toxicol.* **24** (1995) 52; b) S. A. Vinogradov, D. F. Wilson, *J. Chem. Soc. Perkin Trans. 2* (1995) 103.

62. B. Gerlach, F.-P. Montforts, *Liebigs Ann.* (1995) 1509.

63. J. L. Sessler, G. Hemmi, T. D. Mody, T. Murai, A. Burrell, S. W. Young, *Acc. Chem. Res.* **27** (1994) 43.

64. a) E. Vogel, M. Köcher, H. Schmickler, J. Lex, *Angew. Chem., Intl. Edn. Engl.* **25** (1986) 197; b) M. Leunig, C. Richert, F. Gamarra, W. Lumper, E. Vogel, D. Jochani, A. E. Goetz, *Br. J. Cancer* **68** (1993) 225.

65. M. G. H. Vicente, A. C. Tomé, A. Walter, J. A. S. Cavaleiro, *J. Chem. Soc., Chem. Commun.* in preparation.

66. K. Schiwon, H.-D. Brauer, B. Gerlach, C. M. Müller, F.-P. Montforts, *J. Photochem. Photobiol., B: Biol.* **23** (1994) 239.

67. a) M. C. Berenbaum, S. L. Akande, R. Bonnett, H. Kaur, S. Ioannou,

R. D. White, U.-J. Winfield, *Br. J. Cancer* **54** (1986) 717; b) K. R. Adams, M. C. Berenbaum, R. Bonnett, A. N. Nizhnik, A. Salgado, M. A. Valles, *J. Chem. Soc., Perkin Trans. 1* (1992) 1465.

68. a) A. Villanueva, G. Jori, *Cancer Letters* **73** (1993) 59; b) D. Wöhrle, N. Iskander, G. Graschew, H. Sinn, E. A. Friedrich, W. Maier-Borst, J. Stern, P. Schlag, *Photochem. Photobiol.* **51** (1990) 351; c) A. Villanueva, L. Caggiari, G. Jori, C. Milanesi, *J. Photochem. Photobiol., B: Biol.* **23** (1994) 49.

69. a) R. W. Boyle, B. Paquette, J. E. van Lier, *Br. J. Cancer* **65** (1992) 813; b) J. Griffith, J. Gruse-Sawyer, S. R. Wood, J. Schonfield, S. B. Brown, B. Dixon, *J. Photochem. Photobiol., B: Biol.* **24** (1994) 195.

70. a) K. R. Adams, M. C. Berenbaum, R. Bonnett, A. N. Nizhnik, A. Salgado, M. A. Valles, *J. Chem. Soc. Perkin Trans. 1* (1992) 1465; b) D. Kusch, A. Meier, F.-P. Montforts, *Liebigs Ann.* (1995) 1027.

71. D. A. Bellnier, B. W. Henderson, R. K. Pandey, W. R. Potter, T. J. Dougherty, *J. Photochem. Photobiol., B. Biol.* **20** (1993) 55.

72. M. Momenteau, D. Oulmi, P. Maillard, A. Croisy, *Proc. SPIE* **2325** (1994) 13.

73. a) D. Kessel, A. Morgan, G. M. Garbo, *Photochem. Photobiol.* **54** (1991) 193; b) K. Woodburn, D. Kessel *J. Photochem. Photobiol., B: Biol.* **22** (1994) 197; c) S. Georgiou, T. Papazoglou, D. Dafnomili, A. G. Coutsolelos, V. Kouklaki, A. Tosca, *J. Photochem. Photobiol., B: Biol.* **22** (1994) 45; d) C. Richert, *J. Photochem. Photobiol., B: Biol.* **19** (1993) 67.

74. a) M. Soncin, L. Polo, E. Reddi, G. Jori, M. E. Kenney, G. Cheng, M. A. J. Rodgers, *Cancer Lett.* **89** (1995) 101; b) R. Biolo, G. Jori, M. Soncin, B. Rihter, M. E. Kenney, M. A. J. Rodgers, *Photochem. Photobiol.* **63** (1996) 224.

75. a) J. C. Maziere, P. Moliere, R. Santus, *J. Photochem. Photobiol.* **8** (1991) 351; b) G. Jori, *Lasers Med. Sci.* **5** (1990) 115; c) M. R. Hamblin, E. L. Newman, *J. Photochem. Photobiol., B: Biol.* **23** (1994) 3; d) D. Kessel, *Cancer Lett.* **33** (1996) 183.

76. P. Morliere, E. Kohen, J. P. Reyftmann, R. Santus, C. Kohen, J. C. Maziere, S. Goldstein, W. F. Mangel, L. Dubertret, *Photochem. Photobiol.* **46** (1987) 183.

77. a) G. Jori, E. Reddi, *Int. J. Biochem.* **25** (1993) 1369; b) M. R. Hamblin, E. L. Newman, *J. Photochem. Photobiol., B: Biol.* **26** (1994) 147; c) W. G. Love, S. Duk, R. Biolo, G. Jori, P. W. Taylor, *Photochem. Photobiol.* **63** (1996) 656.

78. S. Biade, J. C. Maziere, L. Mora, R. Santus, C. Maziere, M. Auclair, P. Morliere, L. Dubertret, *Photochem. Photobiol.* **57** (1993) 371.

79. V. Vonarx-Coinsman, M.-T. Foultier, L. X. Brito, L. Morlet, A. Gouyette, T. Patrice, *J. Photochem. Photobiol., B: Biol.* **30** (1995) 201.

80. J. C. Kennedy, R. H. Pottier, *J. Photochem. Photobiol., B: Biol.* **14** (1992) 275.

81. C. S. Lok, A. J. MacRobert, J. Bedwell, J. Regula, N. Krasner, S. G. Bown, *Br. J. Cancer* **68** (1993) 41.

82. a) K. König, H. Schneckenburger, A, Rück, R. Steiner, *J. Photochem. Photobiol., B: Biol.* **18** (1993) 287; b) M. Ahram, W.-F. Cheong, K. Ward, D. Kessel, *J. Photochem. Photobiol., B: Biol.* **26** (1994) 203.

83. A. Bamias, P. Keane, T. Krausz, G. Williams, A. A. Epenetos, *Cancer Res.* **51** (1991) 724.

84. J. Morgan, H. Lotman, C. C. Abbou, D. K. Chopin, *Photochem. Photobiol.* **60** (1994) 486.

85. a) A. R. Oseroff, G. Ara, D. Ohuoha, J. Aprille, J. C. Bommer, M. L. Yarmush, J. Foley, L. Cincotta, *Photochem. Photobiol.* **46** (1987) 83; b) F. N. Jiang, D. J. Liu, H. Neyndorff, M. Chester, S. Jiang, J. G. Levy, *J. Natl. Cancer Inst.* **83** (1991) 1218.

86. T. A. Dahl, *The Spectrum* (1992) 11.

PF1/PF2: A Molecular Mechanics Force Field for Conformational Studies on Oxygen and Sulphur Compounds

PF1/PF2: Um Campo de Forças Mecânico-Molecular para o Estudo Conformacional de Compostos de Oxigénio e Enxofre

RUI FAUSTO

DEPARTAMENTO DE QUÍMICA, UNIVERSIDADE DE COIMBRA, P – 3049 COIMBRA (PORTUGAL)

Potential energy functions and important details of computacional procedures currently used in Molecular Mechanics are reviewed. The general orientation followed during the development of the PF1/PF2 force fields and a series of selected results are also presented and analysed to illustrate the efficiency and reliability of these force fields, as applied to conformational and vibrational studies on oxygen and sulphur compounds.

Neste artigo, são discutidas as funções de energia potencial e os aspectos mais relevantes dos procedimentos computacionais correntemente utilizados em Mecânica-Molecular. Apresenta-se a orientação geral seguida durante o desenvolvimento do campo de forças PF1/PF2, e discute-se uma série seleccionada de resultados com ele obtidos, tendo em vista ilustrar a eficácia e poder predictivo quando aplicado ao estudo conformacional e vibracional de compostos de oxigénio ou enxofre.

Introduction

In contrast to the more sophisticated quantum mechanical treatments, the conventional and intuitive description of a molecule with specific bonds between atoms has attracted the growing preference of many scientists for methods, like Molecular Mechanics (MM), that implement a classical representation of molecules and compete with Quantum Mechanics in the quality of the results.

The general principles of MM were laid down fifty years ago [1]. In some small and simple molecules, it was assumed that the molecular geometry would adjust itself to the "natural" values of bond lengths and bond angles. In more complex systems, van der Waals interactions between non-bonded atoms and correlations between bond angles could cause deviations from those values. Comparison between the geometries of the real and model systems was used to measure the strain within the molecule and evaluate specific molecular properties, like geometries, vibrational frequencies and thermodynamic properties.

A complete molecular mechanical calculation involves four fundamental steps:

i) the choice of potential energy functions that correspond to different types of interactions;

ii) the force field parameterization;

iii) the calculation of molecular equilibrium geometries through energy minimization;

iv) the calculation of other molecular properties considering the previously determined equilibrium geometries.

The possibility of calculating a large number of properties is one of the most relevant features of MM. However, its most fundamental characteristic is related with the empirical consistency of the method, imparting a high degree of confidence to the results [2]. In fact, properties of a given molecule are calculated using a set of potential energy parameters previously developed to reproduce experimental values in simpler molecules of the same family.

While the properties considered in a MM study display a large variety and a diverse nature, a general agreement between calculated and experimental values is reached, provided a judicious choice of both potential energy functions and model compounds is performed.
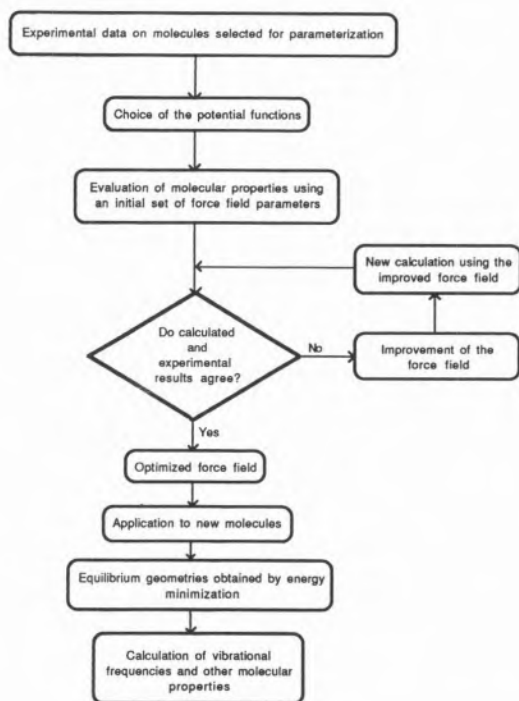
Since MM offers an attractive means of undertaking conformational and vibrational analysis, we have begun to develop this technique in our laboratory with a view to applying it to the most important families of oxygen and sulphur containing molecules. As a starting point, we have developed a MM force field for simple acyl chlorides, carboxylic acids and esters which can also be used to deal with alkanes, alcohols and ethers (**PF1**) [3,4]. This force field was later applied to α-chloro substituted carbonyl compounds, mainly to assess conformational freedom involving rotation around the C_α—$C(=O)$ bond [5-7] and, more recently, extended to deal with both the aldehyde and ketone functional groups [8]. The general quality of the results obtained with the **PF1** force field for these families of oxygen containing molecules has been discussed in detail [9,10] and improves on previously reported MM calculations despite its simplicity.

The extension of **PF1** force field to sulphur containing molecules, named **PF2**, has been successfully carried out more recently and proved to be of great value in studying this kind of molecules [10-12]. Being the first MM force field that can be applied to thiocarbonyl compounds, **PF2** can be used to deal with thiols, thioethers, thioaldehydes, thiones, dithioacids and dithioesters, thus covering a large series of different functional groups.

In this paper, we discuss the general orientation that has been followed during the development of the **PF1/PF2** force fields, with particular emphasis on the selection of potential energy functions. A series of results are also presented and analysed to illustrate the

efficiency and reliability of these force fields, as applied to oxygen and sulphur compounds.

Potential functions

Molecular Mechanics assumes the potential energy as a sum of terms depending on the molecular geometry:

$$\mathbf{E} = E_v + E_\delta + E_\tau + E_{nb} + \dots \tag{1}$$

E, sometimes named "steric energy" [1,2], represents the difference between the energies of the real molecule and the hypothetical molecule where all the structural parameters assume their "natural values". E_v and E_δ the bond stretching and angle bending energies, respectively, result from stretching bonds and bending angles from their "natural values". E_τ, the torsional energy, is associated with internal rotations, and E_{nb} is the energy of interaction between non-bonded atoms. Additional terms can be added to consider the occurrence of specific interactions like intramolecular hydrogen bonding or electrostatic interactions [13,15].

Experience has shown that the choice of functions in the force field is critical. In addition, while a variety of efficient and fast computational algorithms is widely available, the final force field should be both reliable and simple.

Bond stretching and angle deformation

The most extensively used potential energy function associated with bond stretching is

$$V_v(b) = K_{1v}(b-b_o) + 1/2\, K_{2v}(b-b_o)^2 + 1/6\, K_{3v}(b-b_o)^3 \tag{2}$$

where b is the instantaneous bond length, b_o is the corresponding "natural" value and K_{1v}, K_{2v} and K_{3v} are related with the "resistance" of the bond to stretching.

In general, the same kind of function is chosen to represent the potential energy change on angle deformation, *i.e.*,

$$V_\delta(\theta) = K_{1\delta}(\theta-\theta_o) + 1/2\, K_{2\delta}(\theta-\theta_o)^2 + 1/6\, K_{3\delta}(\theta-\theta_o)^3 \tag{3}$$

When both $K_{1\alpha}$ and $K_{3\alpha}$ ($\alpha = v$ (stretching) or δ (bending)) are chosen to be zero, <2> and <3> reduce to harmonic functions. This simplification is very useful from a pratical point of view, as it considerably reduces the number of parameters and the computational time required. It has been followed thoroughly during the development of the **PF1/PF2** force fields.

Experience has demonstrated that the use of harmonic functions generally leads to significantly accurate results, though some studies have been presented that include other terms. In particular, linear terms have been considered [2,16], though their inclusion seems to

be redundant as it amounts to a redefinition of b_o or θ_o. On the other hand, cubic terms deal with anharmonicity, at least in an approximate way. However, they lead to badly behaved functions for large displacements from the equilibrium position (Fig. 1). While this difficulty has been dealt with successfully [17,18], the practical advantages of including cubic terms are not much relevant.
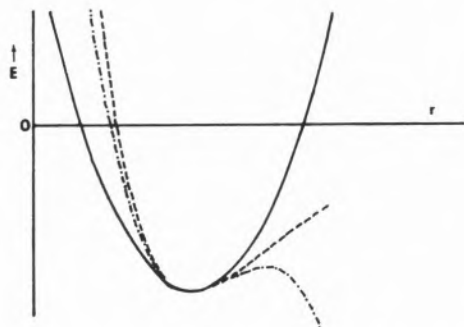
Figure 1 – Harmonic and anharmonic potential: —, harmonic potential; —; Morse type potential –,–., harmonic with cubic term added

Another way to account for anharmonicity is to use Morse functions [19]. In particular, for bond stretching [20]

$$V_v(b) = D \exp[-2k (b-b_o)] - 2D \exp[-k (b-b_o)], \qquad (4)$$

where D and k are related with the dissociation energy and the stretching force constant, respectively. While these functions present some theoretical advantages, the additional computational effort they give rise to discourages their use.

Angle bending terms are of fundamental importance to geminal interactions. The preference for a function like (3) results mainly from its simplicity. However, the inclusion of additional terms related with interactions between adjacent stretching and bending coordinates, have been proposed by several authors [21,22], the

$$V_{vv'}(b,b´) = 1/2 K_{vv'}(b-b_o)(b´-b_o´) \qquad (5)$$

$$V_{v\delta}(b,q) = 1/2 K_{v\delta}(b-b_o)(\theta-\theta_o) \qquad (6)$$

main objective being a better agreement between calculated and experimental vibrational frequencies. Our experience shows that the inclusion of such terms is neither essential to a good force field nor worth the effort.

Non-bonded interactions

The quantitative treatment of intramolecular non-bonded interactions in MM relies very much on simple van der Waals interatomic potentials obtained from rare gases studies [23]. The general form of these potentials exhibits a short distance repulsive interaction and a long distance attraction. The resulting potential profile can be characterised by the minimum energy distance, r* (related with the van der Waals atomic radii), the height of the potential well e (connected with atomic polarizabilities), and the slope of the repulsive section of the curve.
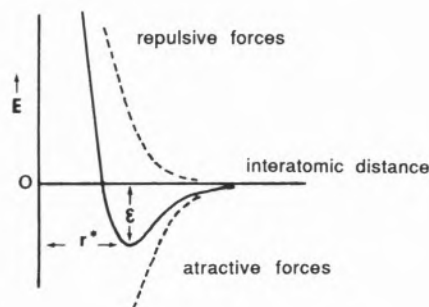
The attractive part of the potential is due to the London dispersion interaction [24]. Perturbation theory yields the following general function

$$V_{disp}(r) = -C_1 r^{-6} - C_2 r^{-8} - C_3 r^{-10} - ... \qquad (7)$$

where r is the interatomic distance and C_1, C_2, C_3, ... depend on atomic polarizabilities and ionization potentials [25]. At short distances, repulsive interactions of the orbital overlap and nuclear-nuclear types dominate, and are generally represented by a negative exponential function or by a positive inverse power function of the interatomic distance,

$$V_{rep}(r) = A \exp(-Br), \qquad (8)$$

$$V_{rep}(r) = Ar^{-n}, \qquad (9)$$

where A and B are adjustable parameters. The results obtained with these functions are qualitatively similar.

The potential functions most extensively used in MM for non-bonded interactions (1-4 and larger) are the modified Buckingham [26] and the Lennard-Jones [27] functions, which result from combining the first term of (7) with expressions (8) or (9), respectively:

$$V_{nb}(r) = A \exp(-Br) - Cr^{-6} \qquad <(10)$$

$$V_{nb}(r) = Ar^n - Br^{-6} \qquad (11)$$

In the case of Lennard-Jones functions, it is common practice to keep n as a constant (usually 12 or 9) [13-15], though its use as an adjustable parameter improves the quality of the results. While a slightly modified Buckingham potential with two parameters has also been used [28,29], experience shows that this reduction in the number of parameters leads to poor results [13], as

in the case of Lennard-Jones functions. Thus, a potential function with three adjustable parameters seems to be necessary for a good description of the van der Waals interactions. In both **PF1** and **PF2**, modified Buckingham potentials with three adjustable parameters are used.

The above mentioned non-bonded potentials assume spherically symmetric electronic densities on atoms and are insensitive to distinct atomic environments.

The first approximation does not work well for atoms with small atomic numbers as these display considerably asymmetric electronic distributions in a molecule. This is especially critical for the hydrogen atom whose single electron gets involved in a bond. In particular, when molecular geometries are correlated with X-ray geometries in crystals, van der Waals potentials centred off the hydrogen atom nuclei have been considered [29-32]. For isolated molecule studies, the choice of less repulsive potentials like those used in both **PF1** and **PF2** strongly improves the results [9,10] without any additional complication.

Atoms with electron lone pairs, like oxygen and sulphur, also display asymmetric electronic densities. Sometimes, the lone pairs have been successfully simulated by specific van der Waals potential functions [33] that picture them as pseudo-atoms. However, this approximation should be discouraged as the explicit consideration of electron lone pairs strongly increases the complexity of the potential energy function. In addition, recent studies clearly indicate that van der Waals lone pair potentials are not necessary, provided the force field optimization is carefully carried out [3,9-12].

The second approximation — insensitivity of non-bonded potentials to distinct atomic environments — is a crude representation of reality, especially when the interacting atoms have large polarizabilities like sulphur or chlorine atoms. In particular, this approximation does not distinguish between atoms on the same side of the molecular skeleton or on opposite sides when the interaction is significantly reduced by the shielding effect of the skeletal atoms. While theoretically unrealistic, this approximation has been assumed so far in all MM studies, and yields excelent agreement with experimental results.

Additional terms related with non-bonded interactions have also been frequently used, in particular, for the consideration of electrostatic interactions [13-15,34-37]. Though the inclusion of these terms was considered relevant by several authors, our experience shows that they can be ignored in a majority of cases, provided van der Waals potentials are correctly evaluated [9,10].

Torsions

Torsional terms are essential for the development of a reliable MM force field, as they take into account interactions not explicitly considered in van der Waals terms, in particular, electronic exchange between adjacent bonds [13] (an alternative interpretation of their importance considers that torsional energy is related with van der Waals repulsion anisotropy, as this is clearly more important for small than for large dihedral angles [38]). In fact, while some effort has been dispensed by several authors to obtain a suitable force field without torsional terms [13-15], no success has yet been reached.

Torsional potentials are usually expressed as functions of the torsional angle (dihedral angle) φ, using a cosine type Fourier series,

$$V_\tau(j) = \frac{1}{2} \sum_n K_{n\tau}[1-\cos(v\varphi)] \qquad (12)$$

where $K_{n\tau}$ are related with rotational barriers and the expansion is truncated in consonance with the rotor symmetry. A frequent simplification, implemented in **PF1/PF2**, uses a single cosine function, *i.e.*, the first term of Eq. (12) for non-symmetrical rotors, and the n=3 term for C_{3v} rotors. This simplification reduces considerably the number of potential parameters and does not originate qualitative changes in the results, thus being very useful from a practical point of view.

Essentially, there are two different ways for consideration of torsions in a mm calculation: *i)* one torsional angle per bond between chain atoms (group torsional model [39]) or, *ii)* one torsional angle for each combination of outer pairs of atoms around a bond (bond torsional model [40]). The second approximation is more appropriate for a nonsymmetrical arrangement of groups and is adopted in **PF1/PF2**.

Torsions around double or partially double bonds are associated with large energy barriers mainly due to electronic effects originated by the reduction of π overlap for non-planar conformations. As these torsional potentials present a maximum value for a dihedral angle near 90°, **PF1/PF2** force fields include a two-fold cosine function (n=2 in expression (12)), with a negative value of $K_{2\tau}$ to account for these specific electronic effects. While an additional n=4 term has been already previously proposed to soften the resulting potential [41], its inclusion is not necessary and is not implemented in our force fields.

The harmonic function,

$$V_\tau(\varphi) = \frac{1}{2} K_\tau (\varphi-\varphi_o)^2, \qquad (13)$$

where φ_o is the dihedral angle corresponding to the minimum energy conformation, was also proposed to represent the torsional potential around double bonds [14]. However, this potential may only be used near the energy minima, when good estimates of equilibrium geometries are available.

The out-of-plane wagging deformations (Ω) are considered as particular cases of torsion and in both **PF1** and **PF2**, this kind of interaction is represented by a cosine function of Ω with n=1.
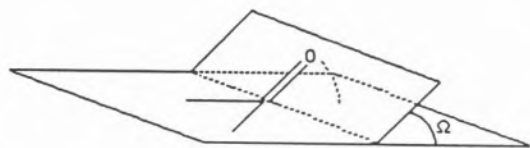
The inclusion of mixed terms involving torsional coordinates has also been suggested by several authors [21,42], to reach an improved agreement between calculated and experimental vibrational frequencies. However, these terms are not essential for the development of a good force field in the large majority of cases [9-15] and have not been considered in **PF1** or **PF2**.

Force field parameterization

The choice of the potential terms is not the single degree of freedom from which the final quality of the force field depends. All potential functions contain interdependent parameters (Fig. 2) which have to be determined as a set, as individual values are not physically meaningful. The optimization process improves on an initial parameter set, until calculated and experimental values agree within predetermined precision.

Stretching:
$$V_\nu = \frac{1}{2} K_\nu (b - b_o)^2$$

Bending:
$$V_\delta = \frac{1}{2} K_\delta (\theta - \theta_o)^2$$

Torsion:
$$V_\omega = \frac{1}{2} K_\omega (1 + \cos(n\varphi))$$

Out-of-plane wagging:
$$V_\tau = \frac{1}{2} K_\tau (1 + \cos(\Omega))$$

Non-bonded:
$$V_{nb} = A\, e^{-Br} - \frac{C}{r^6}$$
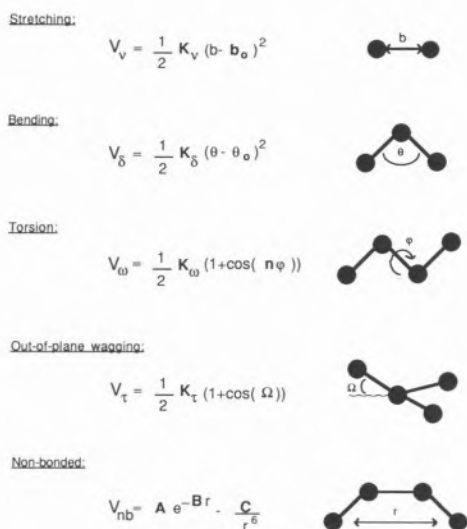
Figure 2 – Potential functions selected to build **PF1/PF2** molecular mechanics force fields. Force field parameters are printed in bold-type

The optimization process can be carried out automatically or by direct inspection of the results. Automatic optimization methods are essentially based on a least squares algorithm that solves the system of n_{opt} simultaneous equations where n_{opt} is the total

$$\partial \mathbf{y}^2 / \partial k_n = 0 \qquad n = 1, ..., n_{opt} \qquad (14)$$

number of potential parameters, k_n refers to the nth parameter to optimize and **y** is the difference vector between experimental and calculated values.

The basic difficulty of this optimization procedure lays on establishing a reliable method of weighting the various molecular properties [15], as parameterization requires a large number of distinct molecular properties. Geometries, conformational energies and thermodynamic properties are generally used; less frequently, vibrational frequencies, dipole moments, magnetic properties or rotational constants are also considered.

The classical least squares minimization method assumes a linear Taylor expansion:

$$\mathbf{y}_{(i+1)} = \mathbf{y}_{(i)} + \sum_{n=1,nopt} (\partial \mathbf{y} / \partial k_n) dk_n \qquad (15)$$

This is a reasonable approximation providing the initial estimates of the parameters are good. The derivatives in expression (17) are calculated in part analytically, since the computing time for a pure numerical evaluation becomes prohibitive [15].

It is important to recall that the convergence of the optimization process is strongly dependent on the initial parameter estimates, thus calling for an active human participation. Therefore, the combined use of the automatic and by-direct-inspection optimization procedures is likely to yield a better parameterized force field [10], thus being used thouroughly in the **PF1** and **PF2** parameterizations.

Whatever the optimization method is, a force field parameterization is always an extremely complex process as it requires a judicious choice of model compounds and observables and involves a large amount of varied experimental data.

It should be pointed out that different experimental techniques yield geometries with different physical meanings, even when the samples are in the same phase. As the development of a force field for isolated molecules requires experimental data from the gaseous phase, the most widely used experimental techniques are microwave spectroscopy and electron diffraction. Since these two techniques are based in different physical phenomena, it is not suprising that they yield non-equivalent structures [43,44]. In particular, as the interaction times for these experiments are different, vibrational motions affect the final structure in different ways. Therefore, the selection of a particular type of molecular structure for force field parameterization should be judiciously performed. As the high resolution power of microwave spectroscopy leads to molecular geometries most suitable for mm calculations they have been used systematicaly in **PF1** and **PF2**.

Energy minimization

Once the force field is parameterized, it can be applied to a particular molecule to get the geometries of its conformations that correspond to minima in the potential energy surface.

The first MM studies could not calculate accurate equilibrium geometries. The geometries of the various conformations to be studied had to be supplied as data, and approximated equilibrium conformations were determined by varying systematicaly the relevant internal coordinates, one by one. These limitations were overcomed after the development of a mathematical algorithm based on an iterative procedure, to perform automatic minimization of the "steric" energy [40].

The analytical solution of the minimization problem is too complex as it requires the solution of a system of n_{cord} non-linear equations

$$\partial E/\partial x_n = 0 \qquad n = 1, ..., n_{cord} \qquad (16)$$

where x represents the coordinates in the configurational space of the molecule. Therefore, the minimization is carried out using numerical methods. Among these, the gradient search methods are the most widely used.

The first minimization method used in MM [40] was based in the steepest descent algorithm [45]. This algorithm is quite efficient during the initial minimization steps, far from the minimum, but it leads to a rather slow convergence near the bottom of the potential well. Therefore, the method is now generally used in the initial stages of the minimization process, and is followed, closer to the equilibrium positions, by methods based in more efficient algorithms, like the Newton-Raphson [46] or the Davidon-Powell-Fletcher [47,48] algorithms.

All methods minimize a given input geometry to a local minimum in the potential energy surface. For molecules with more than a single minimum, the final structure depends on the input geometry. Thus, the conformational analysis of a molecule often requires multiple optimizations, starting with input geometries in different regions of the potential energy surface. In addition, the final geometry depends also on the termination criterium used to stop the iterative process. The most widely used criteria are based on the proximity, to a small predetermined value, of an energy or a geometry variation in subsequent steps. However, when the potential energy well near the minimum is very broad, both of these criteria may stop the minimization process before an acceptable energy minimum has been reached. To avoid this problem, the precision of the termination criterium could be increased, though to the expenses of computational time. A more efficient termination criterium, used in our calculations, is based on the fact that the energy gradient should vanish for equilibrium conformations, and the minimization procedure

is stopped when the quadratic norm of the energy gradient reaches a value sufficiently close to zero.

Sometimes, in a MM calculation, the energy minimization process can lead to a false minimum or to a saddle point. False minima result either from an inadequate minimization technique or from a less realistic parameterization of the force field. Saddle points satisfy the criteria imposed by minimization algorithms, namely the annulement of the energy gradient. However, both of these problems can be avoided if a systematic study of the conformational behaviour of the molecule near each point resulting from minimization is carried out, and adequate algorithms and termination criteria are used [9-14].

Molecular properties calculation

The fundamental ideas of MM are centred on two expressions, namely, [1], which builds the potential energy of the molecule from various contributions, and the following Taylor expansion which allows to

$$E(\underline{x}) = E(\underline{x}_o) + \sum (\partial E/\partial x_i)_o \, dx_i + \sum (\partial^2 E/\partial x_i \partial x_j)_o \, dx_i dx_j, \qquad (17)$$

extrapolate to a neighbouring point the mathematical information on a particular point of the energy surface.

The first term represents the equilibrium "steric" energy of the molecule. Its physical meaning depends on the potential functions used to build the force field. The second term corresponds to the energy gradient and is zero for equilibrium conformations. The third term represents the harmonic vibrational energy, the partial derivatives being the harmonic force constants that define the vibrational force field for a particular equilibrium molecular conformation.

It is important to note the essential difference between potential parameters like K_{2v} or $K_{2\delta}$ (see equations (2) or (3)) and the vibrational force constants. In MM, the vibrational force field for each stable molecular conformation is defined and numerically evaluated from equation (17). On the other hand, all conformations of a given molecule are calculated using the same potential energy function, where several potential parameters are included.

Once the force field is determined, it is easy to evaluate normal modes and their frequencies using one of the current methods of normal coordinate analysis. Wilson's method [49] solves the vibrational problem in internal coordinates; Gwinn's formulation [50] performs the calculations in cartesian coordinates. While Wilson's method is generally preferred by vibrational spectroscopists, mm vibrational calculations are usually performed following Gwinn's method as this requires only one matrix diagonalization and allows a checking of the energy minimization to be made. In fact, if the molecular geometry corresponds to a true minimum in the potential energy surface, six frequencies (five for

linear molecules) are equal to zero as they refer to rotational and translational motions. Once an equilibrium geometry is determined, other molecular properties like inertia moments and rotational constants can be calculated, and thermodynamic properties evaluated from vibrational frequencies and statistical considerations [51]. Infrared intensities can also be estimated provided electrostatic terms are included in the potential energy function.

Alcohols and ethers

The force field for these families of molecules was parameterized using 19 model compounds (9 alkane and 10 alcohol and ether molecules) [3]. The inclusion of alkanes in the parameterization was necessary to deal with hydrocarbon fragments more accurately, and the results on this class of molecules can be found in refs. 3 and 10. In this case, as well as for alcohols and ethers, the results obtained with the **PF1** force field are in excellent agreement with the available experimental values and generally improve on existing calculated literature values.

The structure of the methanol molecule shows a small methyl tilt (angle α of the C-O bond axis with the axis of rotation of the methyl group) towards the lone electron pairs of the oxygen atom [52,53].
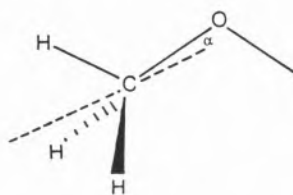
Similar tilt angles have also been experimentally observed in other molecules, like dimethyl ether [54] or ethylmethyl ether [55] which also have a methyl group directly bonded to an oxygen atom. This general trend is correctly predicted by our calculations as all the calculated structures for the above considered molecules present small methyl tilt angles towards the oxygen lone electron pairs in good quantitative agreement with those observed experimentally [3,10].

The results of **PF1** MM calculations are also very useful for understanding and systematizing the general conformational preferences exhibited by both the C-C-C-O and C-C-O-X (X= H or C) axes in alcohols and ethers. In these molecules, the calculations indicate that both the C-C-C-O and C-C-O-X axes adopt preferentially the *anti* conformation (corresponding to a dihedral angle of 180°) [3,10]. A *gauche* C-C-O-C axis (dihedral angle equals ±60°) is destabilized by ≈6 kJ mol⁻¹ relatively to the most stable conformation, while a *gauche* C-C-C-O axis is destabilized only by ≈2 kJ mol⁻¹ relatively to the *anti* C-C-C-O axis in both alcohol and ether molecules

(Fig.3). This increase in the energy difference between *gauche* and *anti* conformations going from the C-C-C-O axis to the C-C-O-C axis relates with the stronger hydrogen-hydrogen interactions involving the hydrogen atoms directly bonded to the terminal carbon atoms in this latter case. The energy difference between the two stable conformations of the C-C-O-H axis (*anti* and *gauche*) is very small (≈0.5 kJ mol⁻¹; see Fig.3).

The similarity observed in the calculated E_{g-a} values for ethers and alcohols indicates that internal rotation around the C-C central bond of this axis is not significantly affected by the group which is bonded to the oxygen atom.
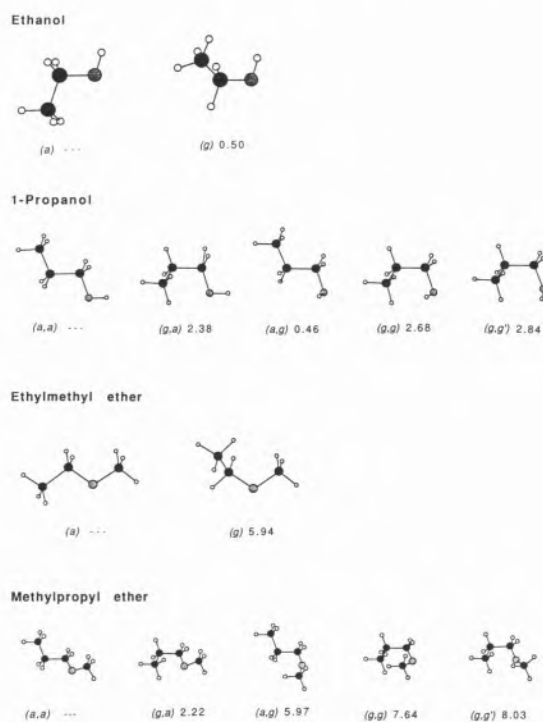
Figure 3 – Conformers and **PF1** relative energies (kJ mol⁻¹) of 1-propanol, ethylmethyl ether and methypropyl ether. *g. gauche; a, anti.*

During the **PF1** force field parameterization, we emphasized the importance of a general agreement between calculated and observed vibrational frequencies. In fact, MM cannot compete with traditional vibrational analysis without requiring an extraordinary increase in both the complexity of the force field and the number of potential parameters [10,14]. Nevertheless, the results obtained for this property with the **PF1** force field show a very good general agreement with the experimental values (Fig.4), the largest errors appearing, as expected, for methyl vibrations, considering the higher symmetry of this group (see ref.10 for detailed discussion).
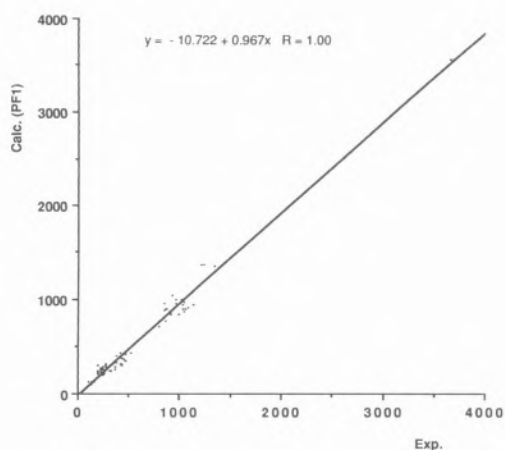
Figure 4 – Calculated **(PF1)** *versus* experimental vibrational frequencies (cm⁻¹) for alcohol and ether molecules. Data was taken from refs. 3, 10 and references therein.

Carbonyl compounds

The quality of the **PF1** results (structures and energies) for carbonyl compounds [4-6,10] is quite similar to that of the results obtained for alkanes, alcohols and ethers. In addition, experimental vibrational frequencies are generally better reproduced by the calculations in the case of carbonyl compounds, as discussed elsewhere [10].

We have used 17 molecules for the carbonyl force field parameterization, 3 of which are α-chloro substituted compounds. While the results for these compounds are particularly interesting, they have been reviewed elsewhere [9], and thus will not be considered in this article.

In general, the calculated structures for aldehydes and ketones [10] agree very well with experiment, and improve existing calculated literature values [56]. In consonance with quantum-mechanical *ab initio* molecular orbital calculations [57], the **PF1** MM calculations indicate that aldehyde fragment behaves like a relatively rigid structural unit with respect to conformational changes. In fact, it was shown that both the aldehyde C-H and C=O bond lengths and the O=C-H bond angle do not change appreciably with the conformation [10]. On the other hand, the C_β-C_α-C(=O) bond angle in these compounds, as well as in ketones, are significantly dependent on the conformation adopted by the molecule. For instance, in propanal and 2-butanone, this angle decreases by ≈1 and ≈2 degrees, respectively, when the conformation changes from the most stable *syn* forms (with a C-C-C=O dihedral angle of 0°) to the *skew* forms (with C-C-C=O dihedral angles in the ±120° region). The larger C-C-C angle observed for *syn* forms can be ascribed, at least partially, to steric repulsions

operating between carbonyl oxygen lone electron pairs and the β-methyl groups.

The MM results obtained for 2-pentanone and 3-pentanone molecules are particularly useful to determine relative stabilities of conformations differing by internal rotation around C_α-C(=O) and C_β-C_α single bonds in saturated ketones. 2-pentanone can exist in five distinct conformers (see Fig. 5, also for naming), the most stable one being the planar *(anti,anti)* form, with both C-C-C_{sp2}-C and C-C-C-C_{sp2} dihedral angles equal to 180°. A similar form — planar *(anti, anti)* — was also found to be the most stable conformers of 3-pentanone (see Fig.6). In fact, from our results for aliphatic ketones, it is possible to conclude that the molecular conformations having a *gauche* C-C-C_{sp2}-C axis are destabilized by approximately 4 kJ mol⁻¹ relatively to those conformations having an *anti* C-C-C_{sp2}-C axis (Fig.5,6). In addition, the energy difference between a *gauche* and an *anti* C-C-
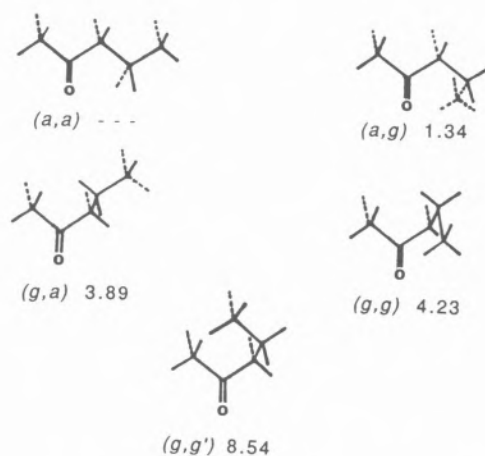
Figure 5 – Conformers and **PF1** relative energies (kj mol⁻¹) of 2-pentanone. g. *gauche*; a, *anti*
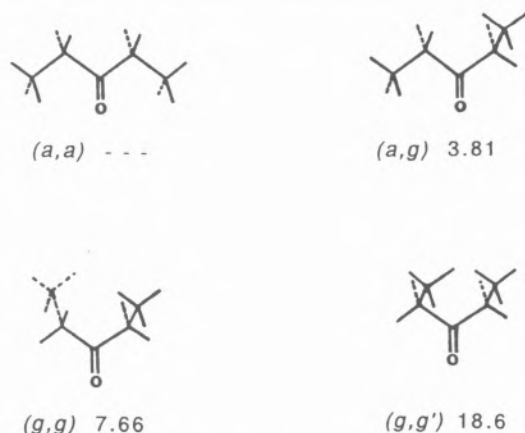
Figure 6 – Conformers and **PF1** relative energies (kJ mol⁻¹) of 3-pentanone. g. *gauche*; a, *anti*

C-C$_{sp2}$ axis is ≈1 kJ mol^{-1}, the *anti* form being the most stable one (see Fig.5). We should point out that the E$_{g\text{-}a}$ in saturated ketones is significantly smaller than the *g-a* energy difference observed in the case of butane (≈4 kJ mol^{-1} [58]). This is certainly due to the fact that the H...H repulsive interactions that occur in the *gauche* forms of ketones are reduced by substitution of one of the methyl terminal groups of butane by the carbonyl linkage.

The internal rotation around the central C$_{sp2}$-O bond in carboxylic acids and esters originates two different planar conformations the *s-cis* form, with a O=C-O-R dihedral angle equals to 0°, being more stable than the *s-trans* form (O=C-O-R dihedral angle equals to 180°).
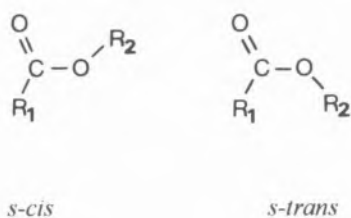
s-cis   *s-trans*

Considering only intramolecular electronic effects, the energy maximum of the *s-cis→s-trans* interconversion reaction should occur for a O=C-O-R dihedral angle near 90°, when mesomeric delocalization reaches a minimum. While electronic effects are usually very difficult to account for by MM calculations, **PF1** force field proved to be very reliable to describe such kind of effects in carboxylic molecules [6,10,51]. Two illustrative examples of capital importance in conformational analysis of these compounds can be pointed out:

i) It is known that the mesomeric delocalization O=CR-OR′ ↔ O-CR=OR′ is less important in the *s-trans* forms of carboxylic acids and esters than in their most stable *s-cis* forms [9-11,59]. This different stability reflects itself in the values of structural parameters, like C-O bond lengths. In particular, **PF1** calculations predict that the central C-O bond length increases by a few picometers and the C=O bond length reduces slightly when going from *s-cis* to *s-trans* conformers [3-6,10], in agreement with experiment,.

ii) The **PF1** calculated energy differences between *s-trans* and *s-cis* conformers in acetic acid and its methyl ester increase by approximately 8 kJ mol^{-1} in the latter molecule [4]. In addition, in methyl acetate, this barrier is predicted to be greater than in acetic acid by ≈20 kJ mol^{-1} [4]. Also, the maximum of the barrier does not seem to occur at 90° in methyl acetate, as it should be predicted if only mesomeric effects were operating in the O=C-O group, but at *ca.* 100°. These increments in the energy differences and in the angle of maximum potential energy may be ascribed both to steric repulsion between the acetyl and methoxyl groups and to the larger indutive or hyperconjugative effect of the methyl ester group. It is remarkable that **PF1** can account for such kind of conformational features, even when both

steric and electronic effects are operating simultaneously.

From the MM results it can be concluded that the *(s-trans)-(s-cis)* energy differences in simple saturated aliphatic carboxylic acids and esters are ≈25 and ≈35 kJ mol^{-1}, respectively (exceptions to this general rule are HCOOH and HCOOCH$_3$). In addition, the energy barriers for *s-cis→s-trans* isomerization are ≈45 kJ mol^{-1} in carboxylic acids and ≈65 kJ mol^{-1} in esters.

The relative stabilities of conformations differing by internal rotation around C$_\alpha$-C and C$_\beta$-C$_\alpha$ bonds in carboxylic acids and esters were also examined and proved to be qualitatively similar to those observed for aldehydes and ketones. Thus, in these molecules, the C-C-C=O and the C-C$_\beta$-C$_\alpha$-C axes adopt preferentially *syn* and *anti* forms, respectively. The less stable *skew* C-C-C=O conformations are higher in energy by ≈6 kJ mol^{-1} than the *syn* forms; the *gauche* C-C$_\beta$-C$_\alpha$-C conformers are ≈4 kJ mol^{-1} less stable than the *anti* form. It is interesting to note that, in both cases, the energy differences between the less stable (*skew* or *gauche*) forms and the most stable form are higher than those found in ketones.

The results obtained for acyl chloride molecules show that a *syn* C-C-C=O axis in these compounds corresponds also to the most stable form, *skew* forms yet being ≈6 kJ mol^{-1} higher in energy than the *syn* conformer [10].

Conformational preferences of the ester group can be summarized as follows:

i) In methyl esters, the lowest energy conformation is the *anti* form, with a H-C-O-C dihedral angle of 180°. In the *syn* conformation (energy maximum) there is a strong steric interaction between the carbonyl atom and the methoxy hydrogen atom (in the plane) that reflects on the large calculated O-C-H$_{in\text{-}plane}$ angles found for this conformation [4].
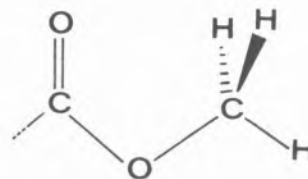
ii) The internal O-C barrier of rotation of the methyl ester group is ≈5 kJ mol^{-1} for all compounds studied in the O=C-O-C *s-cis* conformation. This energy barrier strongly increases for *s-trans* O=C-O-C forms due to the proximity of the methyl ester and the acyl groups.

iii) The C-O-C-C internal rotation in ethyl ester molecules originates two different stable conformers, the *anti* form (dihedral angle of 180°) being most stable than the *gauche* form (C-O-C-C dihedral angle ≈80°) by ≈1 kJ mol^{-1}.

PF1 vibrational results on carbonyl compounds are summarized graphically in Fig.7. As it was pointed

out before, the MM vibrational results for these molecules are in better agreement with the experimental values than in the case of alkanes, alcohols and ethers. This is because the reduced symmetry of the carbonyl moiety makes each calculated frequency essencially dependent on the value of a single potential parameter. In more symmetrical groups, one single parameter may be important to determine the calculated values for several vibrations.

Figure 7 makes clear that the worse agreement obtained between calculated and experimental frequencies occurs for C-C stretching modes. This can be easily understood considering the high degree of vibrational coupling usually found for these vibrations, as well as their sensitivity to structural changes.
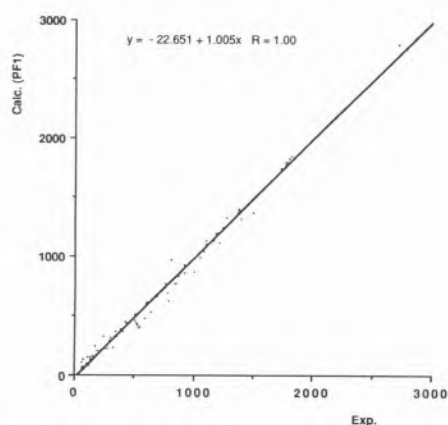
Figure 7 – Calculated **(PF1)** *versus* experimental vibrational frequencies (cm⁻¹) for carbonyl molecules. Data was taken from refs. 3, 10 and references therein.

Thiols and thioethers

The force field for thiols and thioethers (**PF2**) was developed using 9 representative molecules (5 thiols and 4 thioethers) [11]. **PF1** force field parameters were used to deal with hydrocarbon molecular fragments.

The calculated values and the available experimental data for these classes of compounds are in good general agreement. In opposition to what was observed in the case of alcohols and ethers, the MM calculations show that a methyl group directly bonded to the sulphur (thiol or thioether) atom does not show any important tilt towards the sulphur lone electron pairs. The absence of such structural feature in these molecules can be partially ascribed to the longer C-S bond length.

The results obtained for 1-propanethiol are particularly relevant to the understanding of conformational preferences of both the C-C-C-S and C-C-S-H axes in thiols. We have calculated the structures and relative energies of the five expected conformers, *ag, aa, gg, gg* ˜ and *ga* of this molecule (Fig.8). In this notation, the first letter refers to the conformations around the C-C bond,

and the second to the conformations around the C-S bond. The C-C *anti* forms have been determined to be more stable by ≈1.7 kJ mol⁻¹ than the forms which have a C-C *gauche* conformation. The calculated bond lengths and angles in the various conformers are similar. However, the C-S and C-C central bonds as well as the C-C-S angle are slightly increased in the *gauche* C-C forms [11], thus indicating some intramolecular strain in these conformers.
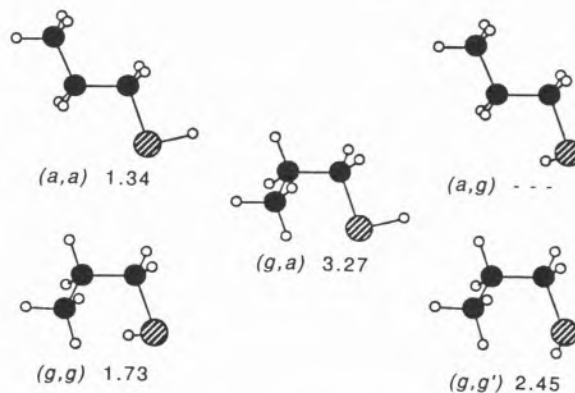
Figure 8 – Conformers and **PF2** relative energies (kJ mol⁻¹) of 1-propanethiol. *g. gauche; a, anti.*

In all studied molecules the sulphydryl group adopts preferentially a *gauche* position (see Fig.8); the *anti* form is higher in energy than the *gauche* form by ≈1.3 kJ mol⁻¹. It should be pointed out that this conformational trend contrasts with that observed in the case of the oxygen analogue molecules which have *anti* C-C-O-H axes more stable than *gauche* C-C-O-H axes, as it was already mentioned in this article. This distinct conformational behaviour seems to suggest that longer C-S bond lengths — leading to longer non-bonded H...H distances and to reduced steric hindrance in *gauche* conformations — might be the origin of this conformational preference around the C-C-S-H axis.

The *gauche* arrangement preference in the immediate neighbourhood of a sulphur atom seems to be a general trend, as the MM calculations also predict that the most stable C-C-S-C axis conformation in thioether compounds is also *gauche* [11]. The results of the calculations on ethylmethyl, methylpropyl and diethyl sulphide molecules are particularly interesting on this instance. The relative stability of the *gauche* and *anti* conformers of ethylmethyl sulphide have been the subject of a variety of experimental and theorethical studies. Experimental work on this molecule has included vibrational spectroscopy [60-65], electron diffraction [66] and microwave spectroscopy [67,68]. It was believed at one time that the *anti* form was more stable than the *gauche* form, and an older MM force field [69] predicted the *anti* form to be 1.21 kJ mol⁻¹ lower in energy than the *gauche* conformer. However, an *ab initio*

SCF MO calculation with a 3-21G+*d* (C,S) basis set and a second order Moller-Plesset pertubation correction to include electron correlation led recently to the conclusion that the *gauche* form is the most stable [70]. This conformational preference is well reproduced by our MM force field, with the *gauche* conformer calculated to be 0.7 kJ mol^{-1} more stable than the *anti* form (Fig.9). In addition, **PF2** indicates that the most stable conformers of diethyl sulphide and methylpropyl sulphide molecules are the *gg* and *ag* forms, respectively (in the case of methylpropyl sulphide, the notation assigns the first letter to the conformation of the C-C-C-S axis and the second to the conformation of the C-C-S-C axis).
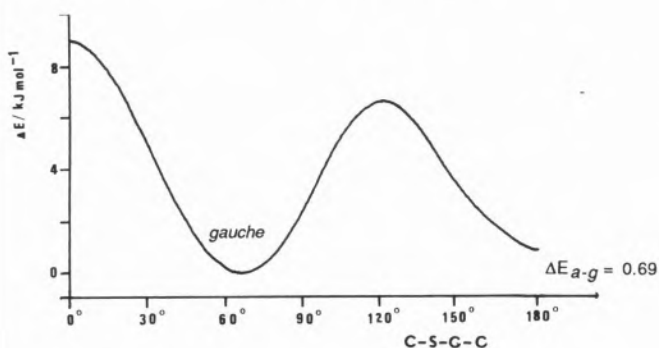
Figure 9 – **PF2** potential energy profile for internal rotation about the C-S bond in ethylmethyl sulphide, showing the greater stability of the *gauche* conformer as compared with the *anti* form.

It is interesting to note that the relative stability of an *anti* and *gauche* C-C-X-C axis (X= C, O, S) favours more the *anti* form for X=O than for X=C, and is reversed for X=S, the *gauche* form being the most stable in this case. A plot of E_{g-a} *vs.* C-X bond length gives a straight line (Fig.10) thus showing that the *g-a* relative stability
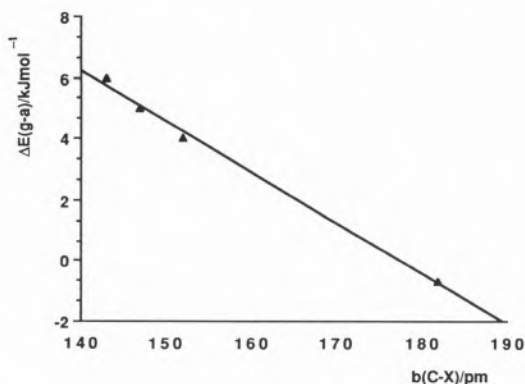
Figure 10 – $\Delta E_{g-a}^{c-c-x-c}$ (X = O, CH$_2$, NH, S) *versus* the lenght (b$_{c-x}$) of the C-X central bond. The straight line obeys to the equation $\Delta E_{g-a}^{c-c-x-c}$ = 29.61.b$_{c-x}$ - 0.17, the correlation coefficient being 1.00.

around a C-C-X-C axis depends on the length of the central C-X bond. We should recall that the data presented in Fig.10 also include recent results on relative energies of *gauche* and *anti* forms of the C-C-N-C axis in ethyl-methyl amine [71], and that the linear dependence observed for the above considered molecules is also obeyed by this molecule.

PF2 vibrational results on thiols and thioethers are summarized in Fig.11. This Figure presents only the results for skeletal vibrations and for those modes involving the functional groups. The calculated values for other modes show the same general trends found for alkane, alcohol and ether molecules. Generally speaking, the agreement between calculated and experimental values is satisfactory, while the calculated C-C stretching frequencies are too small, a trend which had already been noticed for alkanes [3].
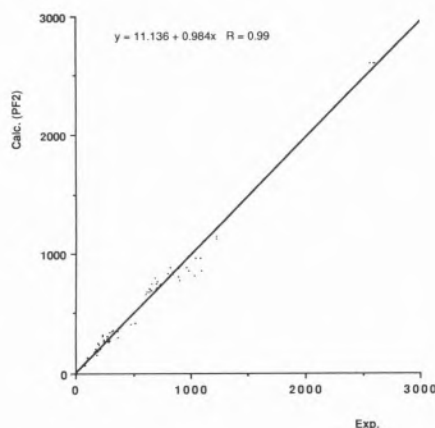
Figure 11 – Calculated **(PF2)** versus experimental vibrational frequencies (cm^{-1}) for thiol and thioether molecules. Data was taken from refs. 10, 11 and references therein.

Thiocarbonyl compounds

The most recent extension of **PF2** to thiocarbonyl compounds was intended to deal with thioaldehyde, thione, dithioacid and dithioester groups. Ten model compounds were used to determine specific thiocarbonyl potential parameters. The resulting force field is the first MM force field parameterized for these families of molecules. In fact, the necessary information for such force field development only recently became available, as a result of our investigations on the structures and properties of thiocarbonyl compounds by means of a series of sistematic *ab initio* quantum mechanical SCF-MO calculations [10,59,72-74].

The MM results obtained for the molecules used in the parameterization agree very well with the reference *ab initio* values [10-12]. In addition, changes in molecular geometries associated with internal rotations are also

correctly predicted. For instance, the **PF2** calculated C-C=S and C-C$_{sp2}$-H angles for ethanethial in the *anti* conformation (H-C-C=S dihedral angle equals to 180°) are 125.3° and 116.2°, respectively; the *ab initio* values for these angles are 125.0° and 116.2°. In addition, in the lowest energy conformation (*syn*), these angles (*ab initio* ; **PF2**) are (*125.6°* ; **126.7°**) and (*115.5°* ; **115.4°**), respectively, while the H-C=S angles were predicted to be very similar in both conformations, by mm as well as by *ab initio* methods. Molecular mechanical calculations predict also correctly the relative values of C-H bond lengths and C$_{sp2}$-C-H angles involving the hydrogen atoms located in and out of the molecular plane. Molecular orbital calculations [74] have shown that the α-carbon *2s* orbital has a larger contribution to the C-H in-plane bond than to the out-of-plane bonds. The larger *s* character of the in-plane bond leads to a relatively small bond length for this bond and to a larger C$_{sp2}$-C-H angle.

The conformational study of 2-pentanethione and 3-pentanethione is particularly relevant to the understanding of conformational preferences exibited by C-C-C$_{sp2}$-C and C-C-C-C$_{sp2}$ axes in the vicinity of a thiocarbonyl group. In consonance with the relative stability of the

various conformers of these molecules (Fig.12), a *gauche* C-C-C$_{sp2}$-C axis (±60°) is more stable than an *anti* C-C-C$_{sp2}$-C axis (180°) by approximately 1kJ mol^{-1}. This contrasts with the trends exibited by carbonyl compounds where the *anti* conformation is the most stable one. On the other hand, the C-C-C-C$_{sp2}$ axis adopts preferentially the *anti* conformation, either in thiocarbonyl or in carbonyl compounds. However, the C-C-C-C$_{sp2}$ *gauche-anti* energy difference is appreciably larger in thiocarbonyl than in carbonyl molecules (E$_{gauche-anti}$ ≈3 and 1 kJ mol^{-1}, respectively). This destabilization of *gauche* forms upon O→S substitution results mainly from strong interactions between the sulphur atom and the *gauche* 3-methyl substituents due to the larger van der Waals radius of the sulphur atom.

Geometry changes accompanying the *s-cis→s-trans* conversion in dithioacids and dithioesters (see refs. 72 and 73 for a detailed discussion) are correctly predicted

2-Pentanethione

(a,a) 1.43   (g,a) ---

(g,g) 2.82   (g,g') 4.29

3-Pentanethione

(a,a) 1.20   (g,a) 0.70

(g,g) ---   (g,g') 0.49

Figure 12 – Conformers and **PF2** relative energies (kJ mol^{-1}) of 2-pentanethione and 3-pntanethione. g, *gauche*; a, *anti*.
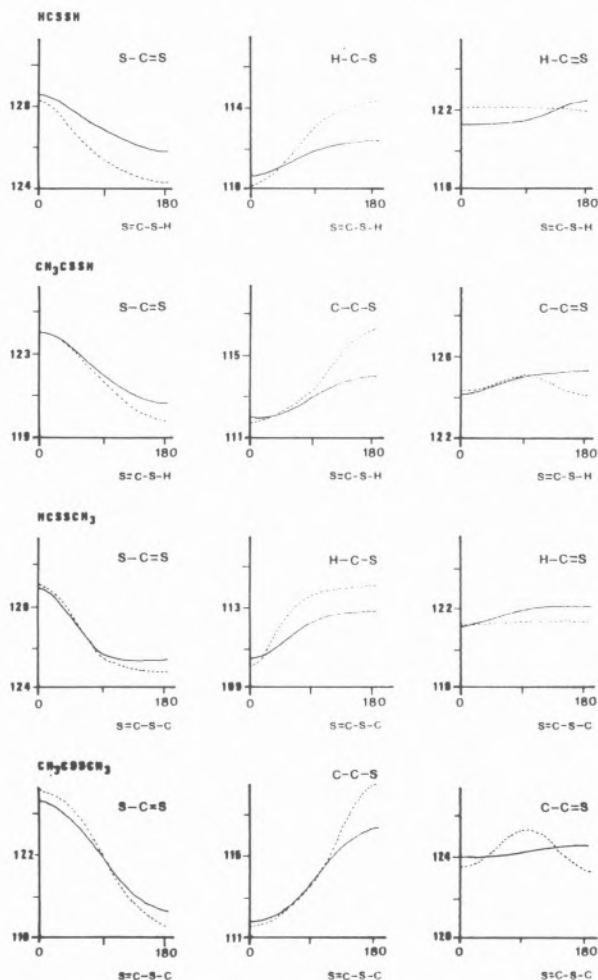
Figure 13 – Geometry changes accompanying the *s-cis→s-trans* conversion in RC(=S)SR (R = H or CH$_3$) molecules, –, **PF2** –,*ab initio* 3-21G.

by the MM calculations. Figure 13 shows an excellent agreement between MM and *ab initio* results for S=C-S, X-C=S and X-C-S angles (X=H or C) of dithioformic and dithioacetic acids and their methyl esters, along the *s-cis*→*s-trans* isomerization.

The results obtained for the set of molecules having one α-methyl group ($CH_3CH_2C(=S)X$, X= H, CH_3, SH or SCH_3) enable us to correlate conformational preferences of this group with the X substituent. In all the molecules studied *gauche* forms are more stable than *syn* forms, the C-C-C=S dihedral angles of the *gauche* forms increasing along the series X= H] SCH_3 *(s-cis)* ≈SH *(s-cis)*] SH *(s-trans)* ≈SCH_3 *(s-trans)*. Considering that larger C-C-C=S angles correlate with smaller $CH_{3(α)}$...X distances and stronger $CH_{3(α)}$...X repulsive interactions, the calculated values of these angles in the above series of molecules show that $CH_{3(α)}$...X interactions are more important when the X substituent is bulky and positively charged. These interactions destabilize *gauche* forms with respect to the *syn* conformer, reflecting on the largest *gauche-syn* energy differences for molecules where X is a methyl group, or for molecules that exhibit a *s-trans* conformation around the C—S central bond.

The results obtained for molecules having two α-methyl groups ($C(CH_3)_2HC(=S)X$, X= H, CH_3, SH and SCH_3) reveal that a similar correlation between conformational preferences and the nature of the X group can also be established for these molecules. In this case, bulkier and more positive X groups correlate with less stable *syn* forms, because in this conformation both α-methyl groups are placed near the X group. Thus, the *syn* form is the most stable form when X = H, SH(*s-cis*) and SCH_3(*s-cis*), while the *gauche* form becomes the most stable one either for the *s-trans* forms of the dithioacid and dithioester molecules or for X = CH_3.

As it was shown for single methyl substituted molecules, the calculated relative values for the H-C-C=S dihedral angle of the *gauche* forms can also be used to analyse the relative strength of the $CH_{3(α)}$...X interactions along the series of molecules now considered, though, in this case, larger H-C-C=S dihedral angles correspond to larger $CH_{3(α)}$...X distances.

The results obtained for ethyl dithioesters allow to understand the conformational preferences of the ethyl fragment in these molecules. In both ethyl dithioformate and ethyl dithioacetate the internal rotation around the C-S bond gives rise to two distinct stable conformations: the *anti* (C-C-S-C dihedral angle equals 180°) and the *gauche* forms (C-C-S-C dihedral angle near 60°). The lowest energy forms, for both *s-cis* and *s-trans* S=C-S-C axes, correspond to the *gauche* form, in contrast to the dioxygen compounds. These conformational preferences can be explained considering:

i) the larger C-S bond lengths that result in weaker CH_3(*gauche*)...S= steric interactions in dithioesters compared to CH_3(*gauche*)...O= interactions in oxygen esters;

ii) the reduced mesomeric aptitude of the sulphur atom, leading to a less effective electronic stabilization of the *anti* conformer in dithioesters than in esters;

iii) the stronger through-space repulsive interactions between thiolic lone electron pairs and the terminal methyl group (more important in the *anti* conformer than in the *gauche* form), as compared with CH_3...$O_{lone\ pairs}$ interactions in oxygen esters.

In consonance with the above reasoning, the C_{sp2}-S-CH_2-CH_3 axis should also preferencially adopt the *gauche* conformation in ethyl thiolesters, while the lowest energy conformation of the C_{sp2}-O-CH_2-CH_3 axis in ethyl thionoesters should be *anti*.

PF2 vibrational results on thiocarbonyl compounds are resumed in Fig.14, where they are compared with experimental data. It can be concluded, from this figure that the general agreement between calculated and experimental values is qualitatively similar to that obtained for carbonyl compounds.
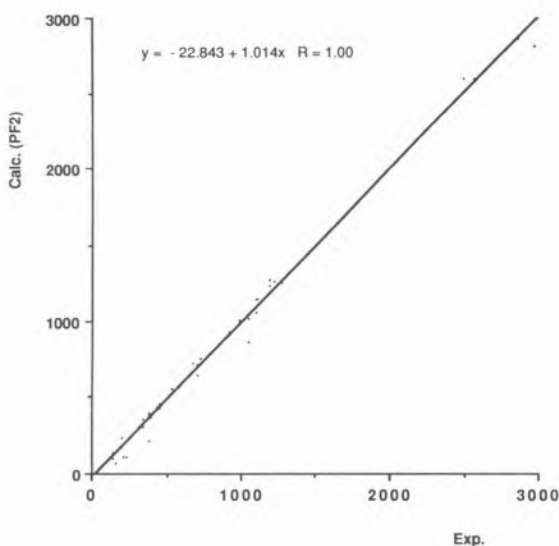
Figure 14 – Calculated **(PF2)** *versus* experimental vibrational frequencies (cm⁻¹) for thiocarbonyl molecules. Data was taken from refs. 10, 12 and references therein.

Acknowledgements

References

1. T.L.Hill, *J.Chem.Phys.* 14 (1946) 465.

2. S.Lifson and A.Warshel, *J.Chem.Phys.* **49** (1968) 5116.

3. J.J.C.Teixeira-Dias and R.Fausto, *J.Mol.Struct.* **144** (1986) 199.

4. R.Fausto and J.J.C.Teixeira-Dias, *J.Mol.Struct.* **144** (1986) 215.

5. R.Fausto and J.J.C.Teixeira-Dias, *J.Mol.Struct.* **144** (1986) 225.

6. R.Fausto and J.J.C.Teixeira-Dias, *J.Mol.Struct.* **144** (1986) 241.

7. J.J.C.Teixeira-Dias and R.Fausto, *Pure and App.Chem.* **61** (1989) 959.

8. R.Fausto and J.J.C.Teixeira-Dias, *Proceedings of the 11th Meeting of the Portuguese Society of Chemistry*, Lisbon, Portugal, 1988, p.QF-CE5.

9. J.J.C.Teixeira-Dias and R.Fausto, *Rev.Port.Quím.* **29** (1987) 47.

10. R.Fausto, Ph.D.Thesis, The University Chemical Department, Coimbra, Portugal, 1987.

11. R.Fausto, J.J.C.Teixeira-Dias and P.R.Carey, *J.Mol.Struct.* **159** (1987) 137.

12. R.Fausto, J.J.C.Teixeira-Dias and P.R.Carey, *J.Mol.Struct.* **212** (1989) 61.

13. U.Burket and N.L.Allinger, *"Molecular Mechanics"*, ACS Monograph 177, Am.Chem.Soc. Washington, USA, 1982.

14. S.R.Niketic` and K.Rasmussen, *"The Consistent Force Field: A Documentation"*, Lecture Notes in Chemistry, Vol.3, Springer-Verlag, Heidelberg, FRG, 1977.

15. K.Rasmussen, *"Potential Energy Functions in Conformational Analysis"*, Lecture Notes in Chemistry, Vol.37, Springer-Verlag, Heidelberg, FRG, 1985.

16. C.Altona and M.Sundaralingam, *J.Am.Chem.Soc.* **92** (1970) 1995.

17. E.M.Engler, J.D .Andose and P.V.R.Schleyer, *J.Am.Chem.Soc.* **95** (1973) 8005.

18. D.H.Wertz and N.L.Allinger, *Tetrahedron*, **30** (1974) 1571.

19. P.M.Morse, *Phys.Rev.* **34** (1929) 57.

20. A.Warsheel, *J.Chem.Phys.* **55** (1971) 3327.

21. N.L.Allinger, M.T.Tribble, M.A.Miller and D.H.Wertz, *J.Am.Chem.Soc.* **93** (1971) 1637.

22. O.Ermer, *Tetrahedron*, **30** (1974) 3130.

23. H.Margenan and N.R.Kestner, *"Theory of Intermolecular Forces"*, Pergamon Press, Oxford, U.K. 1969.

24. F.London, *Trans.Faraday Soc.* **33** (1937) 8.

25. K.S.Pitzer, *Adv.Chem.Phys.* **2** (1959) 59.

26. R.A.Buckingham, *Trans.Faraday Soc.* **54** (1958) 453.

27. J.E.Lennard-Jones, *Proc.Roy.Soc.* **43** (1931) 461.

28. N.L.Allinger, *J.Am.Chem.Soc.* **99** (1977) 8127.

29. N.L.Allinger and D.Y.Chung, *J.Am.Chem.Soc.* **98** (1976) 6798.

30. D.E.Williams, *J.Chem.Phys.* **43** (1965) 4424.

31. D.E.Williams and T.L.Starr, *Comput.Chem.* **1** (1977) 173.

32. U.Burket, *Tetrahedron*, **33** (1977) 2237.

33. T.Laier and E.Larsen, *Acta Chem.Scand.* **A33** (1979) 257.

34. G.Del Re, *J.Chem.Soc.* (1958) 4031.

35. S.Melberg and K.Rasmussen, *J.Mol.Struct.* **57** (1979) 215.

36. G.N.Ramachandram and K.Srinivasan, *Int.J.Protein Res.* **1** (1969) 5.

37. A.J.Hopfinger, *"Conformational Properties of Macromolecules"*, Academic Press, New York, USA, 1973.

38. A.I.Kataigorodski, *Chem.Soc.Rev.* **7** (1978) 133.

39. G.J.Gleicher and P.V.R.Shleyer, *J.Am.Chem.Soc.* **89** (1967) 582.

40. K.B.Wiberg, *J.Am.Chem.Soc.* **87** (1965) 1070.

41. O.Ermer, *"Aspekte von Kraftfeldrechnungen"*, Wolfgang Bauer Verlag, Munich, FRG, 1981.

42. A.Warshel and S.Lifson, *Chem.Phys.Lett.* **4** (1969) 255.

43 . K.Kuchitsu and S.J.Cyvin, *"Molecular Structures and Vibrations"*, Ed.S.J.Cyvin, Elsevier, Amsterdam, Neederlands, 1972, Cap.12.

44. K.Kuchitsu, *"Critical Evaluatioin of Chem. and Phys. Structural Information"*, Ed.D.R.Lide and M.A.Paul, Nat.Acad.Sci. Washington, USA, 1974, p.132-139.

45. A.Cauchy, *Comp.Rend.Sci.(Paris)*, **25** (1847) 536.

46. P.E.Gill, W.Murray and S.M.Picker, *Natl.Phys.Lab.Report*, NAC 24, 1972.

47. W.C.Davidon, *AEC Res. and Develop.Report*, ANL-5990 (rev.), 1959.

48. R.Fletcher and M.J.Powell, *Comput.J.* **7** (1963) 149.

49. E.B.Wilson, *J.Chem.Phys.* **9** (1941) 76.

50. W.D.Gwinn, *J.Chem.Phys.* **55** (1971) 477.

51. R.Fausto, *"Aplicações da Mecânica Molecular e da Espectroscopia Vibracional à Análise Conformacional"*, The University Chemical Department, Coimbra, Portugal, 1984.

52. K.Kimura and M.Kubo, *J.Chem.Phys.* **30** (1959) 151.

53. RT.M.Lees and J.G.Baker, *J.Chem.Phys.* **30** (1968) 5299.

54. K.Tamagawa, M.Takemura,S.Konaka and M.Kimura, *J.Mol.Struct.* **125** (1984) 131.

55. M.Hayashi and K.Kuwada, *J.Mol.Struct.* **28** (1975) 147.

56. N.L.Allinger, M.T.Tribble and M.A.Miller, *Tetrahedron*, **28** (1972) 1173.

57. V.J.Klimkowski, P.V.Nuffel, L.V.D.Enden, C.V.Alsenoy, H.J.Geise, J.N.Scarsdale and L.Schafer, *J.Comp.Chem.* **5** (1984) 122.

58. V.Sackwild and W.G.Richards, *J.Mol.Struct.* **89** (1982) 269.

59. R.Fausto, L.A.E.Batista de Carvalho, J.J.C.Teixeira-Dias and M.N.Ramos, *J.Chem. Soc. (Faraday Trans. II)*, **85** (1989) 1945.

60. M.Ohsaku, Y.Shiro and H.Murata, *Bull.Chem.Soc.Jpn.* **45** (1972) 954.

61. M.Ohsaku, Y.Shiro and H.Murata, *Bull.Chem.Soc.Jpn.* **46** (1973) 1399.

62. M.Hayashi, T.Shimanouchi and S.Mizushima, *J.Chem.Phys.* **26** (1957) 608.

63. N.Nogami, H.Sugeta and T.Miyazawa, *Bull.Chem.Soc.Jpn.* **48** (1975) 3573.

64. M.Sakakibara, H.Matsuura, I.Harada and T.Shimanouchi, *Bull.Chem.Soc.Jpn.* **50** (1977) 111.

65. J.R.Durig, D.A.C.Compton and M.R.Jalilian, *J .Phys.Chem.* **83** (1979) 511.

66. K.Oyanagi and K.Kuchitsu, *Bull.Chem.Soc.Jpn.* **51** (1978) 2243.

67. M.Adachi, J.Nakagawa and M.Hayashi, *J.Mol.Spectrosc.* **91** (1982) 381.

68. M.Hayashi, M.Adachi and J.Nakagawa, *J.Mol.Spectrosc.* **86** (1981) 129.

69. N.L.Allinger and M.J.Hickey, *J.Am.Chem.Soc.* **97** (1975) 5167.

70. M.Ohsaku and A.Imamura, *Mol.Phys.* **55** (1985) 331.

71. L.A.E.Batista de Carvalho, Ph.D.Thesis, The University Chemical Department, Coimbra, Portugal, 1989.

72. R.Fausto and J.J.C.Teixeira-Dias, *J.Mol.Struct.(Theochem.)*, **150** (1987) 381.

73. R.Fausto, J.J.C.Teixeira-Dias and P.R.Carey, *J.Mol.Struct.(Theochem.)*, **152** (1987) 119.

74. R.Fausto, J.J.C.Teixeira-Dias and P.R.carey, *J.Mol.Struct.(Theochem.)*, **168** (1988) 179.